The application of low dimensional nanomaterials in electrocatalysis and electrochemical biosensing

by

Zanzan Zhu

A Dissertation

Submitted to the Faculty

of the

WORCESTER POLYTECHNIC INSTITUTE

in partial fulfillment of the requirements for the

Degree of Doctor of Philosophy

in

Chemical Engineering

May 2015

Approved by

Dr. Hong Susan Zhou, advisor

Department of Chemical Engineering

Worcester Polytechnic Institute

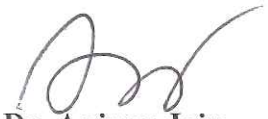

Dr. Anjana Jain

Department of Biomedical Engineering

Worcester Polytechnic Institute

Dr. Nathaniel A. Deskins

Department of Chemical Engineering

Worcester Polytechnic Institute

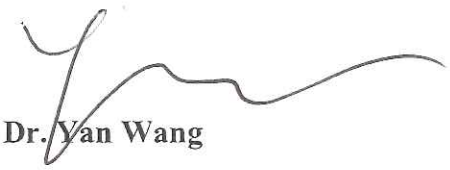

Dr. Yan Wang

Department of Materials Science& Engineering

Worcester Polytechnic Institute

Abstract

Electrochemistry, based on the study of an electrochemical reaction at the interface between an electrode and an electrolyte, is having a profound effect on the development of different fields of science and engineering including battery, fuel cell, electrochemical sensor, electrochromic display, electrodeposition, electroplating, electrophoresis, corrosion, and so on. The performance of the electrochemical reaction depends strongly on the nature of the employed electrode such as structure, chemical composition, and surface morphology. Nanomaterials, notable for their extremely small feature size (normally in the range of 1-100 nm), exhibit new properties which are different from those of bulk materials due to their small size effect. In past decade, nanomaterials have been widely used to develop new strategies for designing electrode and its surface morphology for electrocatalysis and electrochemical sensing applications. My work is aimed at exploring the application of low dimensional nanomaterials (nanotubes and nanoparticles) in electrocatalysis and electrochemical biosensors.

Electrocatalysis plays an important role in energy and industrial applications. As one of the most attractive support materials for electrocatalyst, carbon nanotubes have been extensively reported to enhance the performance of various electrochemical catalytic reactions. In recent years, carbon nanotubes with a bamboo-like structure due to nitrogen doping have become a hot topic of increased interest in the field of electrocatalysis because of the unique bamboo shaped structure associated properties. In this work, bamboo shaped carbon nanotubes, synthesized by chemical vapor deposition method, were investigated for ethanol/methanol electro-oxidation, respectively. Small sized platinum nanoparticles (Pt NPs) were dispersed onto BCNT surface through an impregnation method. The role of nitrogen doping in the formation of bamboo shaped structure and its effect in the electrochemical performance of CNTs were discussed. The electrochemical

studies showed that the as-prepared Pt/BCNTs electrocatalysts indeed exhibited a remarkable enhancement in catalytic activity for methanol/ethanol oxidation compared to that of the Pt/commercial CNT electrocatalysts. In order to further investigate the potential of using BCNTs as bioelectrocatalyst support materials, a hybrid organic-inorganic nanocomposite film of BCNTs/ploymer was constructed to immobilize an enzyme horseradish peroxidase (HRP) to examine the direct electrochemical behavior of the enzyme towards electrocatalysis process of H_2O_2. The results indicated that the immobilized HRP onto the film retains its good bioelectrocatalytic activity to H_2O_2. The defective sites on the BCNTs surface induced by nitrogen doping could help to promote the direct electron transfer between enzyme and the electrode. The BCNT/polymer film structure provides a vast array of new opportunities to use BCNTs as building units for bioelectrochemical and biomedical applications.

Compared to carbon nanotubes, TiO_2 nanotubes have much better biocompatibility and show greater potential as implant materials. The advantages of TiO_2 nanotube array include high biocompatibility, good corrosion resistance in biological environments and highly ordered one dimensional nanotubular geometry. Herein, a well performing non-enzymatic electrochemical glucose biosensor by using CuO nanoparticle decorated TiO_2 nanotube array electrode was developed. Well-aligned TiO_2 nanotube arrays were successfully synthesized by electrochemical anodization. Highly uniform CuO nanoparticles were electrodeposited onto TiO_2 nanotube arrays through a two-step method and used to electrocatalyze the glucose oxidation. The proposed electrode produced a high sensitivity of 239.9 μA mM^{-1} cm^{-2} and a low detection limit of 0.78 μM with good stability, reproducibility, selectivity and fast response time, suggesting its potential to be developed as a low-cost nano-biosensor for glucose measurements in human fluids.

The final work of this thesis presents a simple sandwich-type electrochemical impedance immunosensor with antitoxin heavy-chain-only V_H (V_HH) antibodies labeled gold nanoparticles as the amplifying probe for detecting *Clostridium difficile* toxins. Gold nanoparticles (Au NPs) with diameter of ~13-15 nm were synthesized and characterized by transmission electron microscopy and UV-vis spectra. The electron transfer resistance of the working electrode surface was used as parameter in the measurement of the biosensor. With the increase of the concentration of toxins from 1pg/mL to 100 pg/mL, a linear relationship was observed between the relative electron transfer resistance and toxin concentration. In addition, the detection signal was enhanced due to the amplification effect. This proposed method achieved a limit of detection for TcdA and TcdB as 0.61 pg/mL and 0.60 pg/mL, respectively. The pilot study with spiked clinical stool samples showed promising results, indicating the designed biosensor has a great potential in clinical applications.

Acknowledgements

I would like to thank my advisor, Dr. Hong Susan Zhou, for her guidance and support during my PhD study at WPI. She encouraged me to work hard and helped me a lot with her expertise during these years. She taught me how to thick deeply and broadly about my research topic. I would also like to thank my committee members, Dr. Anjana Jain, Dr. Nathaniel A. Deskins, and Dr. Yan Wang, for insightful questions and professional comments on my thesis.

I also want to extend my thanks to Prof. Hanping Feng in Department of Microbial Pathogenesis in University of Maryland Dental School. He not only provided antibodies and antigens for my research, but also taught me much knowledge on immunology. I want to thank Dr. Kathleen Wang for her help in using high–intensity ultrasonic probe in Professor Terri Camesano's lab in Department of Chemical Engineering in WPI, Mr. Jack Hirsch for his help in analyzing XPS in Umass Amherst, Sia Najafi for his help in using WPI's computer clusters and Yinjie Cen for his help in using electrochemical anodization equipment in Prof. Jianyu Liang's lab in Department of Materials Science & Engineering in WPI.

In addition, I wish to thank all the current and former lab members for their suggestions, support and friendship. Thank you to Mr. Douglas White in Department of Chemical Engineering for his machine shop services on my research. I also would like to acknowledge Ms. Felicia Vidito and Ms. Tiffany Royal of the Chemical Engineering office for all their administrative help.

Finally, my special thanks are given to my father, Yu'an Zhu, my mother, Haixiang Chen and my husband, Dr. Zhichuan Xu for their continuous and unconditional love and support.

Table of contents

List of figures

List of tables

List of schemes

Chapter 1 Introduction

1.1 Electrochemistry background

1.1.1 Electrochemistry: an overview

Electrochemistry is focused on the research of an electrochemical reaction which is a heterogeneous chemical process involving the electron transfer between an electrode (metal, carbon, semiconductor, etc.) and an electrolyte (ionic conductor). In general, oxidation-reduction (redox) reactions happened on the electrode might be an anodic or cathodic process refers the loss or gain of electrons to or from the electrode. The field of electrochemistry includes a huge array of different subjects in science, engineering and technology, such as battery, fuel cell, electrochemical sensor, electrochromic display, electrodeposition, electroplating, electrophoresis, corrosion, and so on [1].

Fig 1.1 shows the pathway of a simple oxidation-reduction process ($O + ne \leftrightarrow R$) on an electrode. The conversion from the oxidized species O to the reduced species R is made up of several steps as below:

(1) Mass transfer of oxidized species O from bulk solution to the electrode surface;

(2) In the electrode surface region, chemical reactions including adsorption, desorption, pronation and decomposition might precede or follow the electron transfer steps;

(3) Electron transfer at the electrode surface;

(4) Mass transfer of the reduced species R from the electrode surface to bulk solution.

As a whole process, the rate of the overall electrochemical reaction on the electrode surface is determined by both the electron transfer on the electrode surface and the mass transport of the species between the bulk solution and electrode surface region [1].

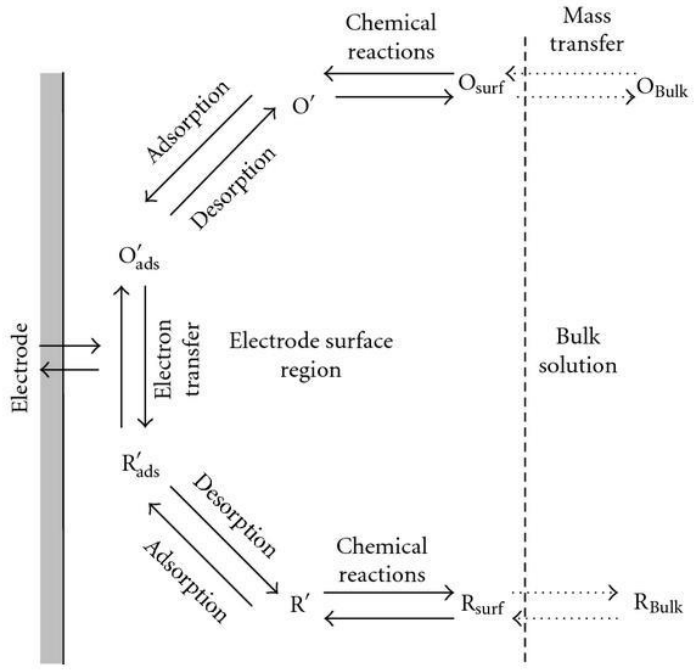

Figure 1.1 Pathway of a general electrode reaction in the electrochemical process. Adopted from Ref. [1].

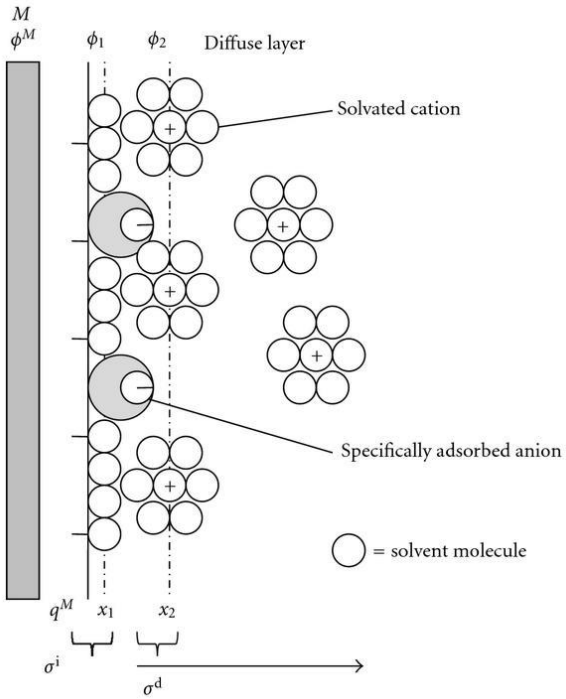

Figure 1.2 Helmholta model of the electrical double layer. Adopted from Ref. [1].

In the discussion of electron transfer, the interface between the electrode and the electrolyte is a key point, where a specific interfacial region called electrical double layer is formed. The electrical properties of this double layer significantly affect the electrochemical measurement in the practical applications. The model of the electrical double layer was first put forward by Helmholta in 1897 [2]. In this model, it has been assumed that there is an excess of electrons at the electrode surface, in order to neutralize the charged surface, ions and solvent molecules approach the electrode surface and form several layers. As presented in Fig. 1.2, usually, there are two layers are associated with the electrical double layer. The inner Helmholtz plane (ϕ_1) is the layer closest to the electrode, which passes through the centers of specifically absorbed ions and molecules. The distance to the electrode is x_1. The outer Helmholtz plane (ϕ_2) is located in the centers of the solvated ions, which are nonspecifically absorbed. The distance to the electrode is x_2. The diffuse layer contains solvent ions which decrease exponentially vs. the distance from the electrode surface [1].

1.1.2 Common techniques in electrochemistry

Common techniques in electrochemistry include voltammetry, amperometry, potentiometry, conductometry, electrochemical impedance spectroscopy (EIS), and so on. In amperometry, the working electrode is held at a constant potential and current changes by electrochemical oxidation/reduction reaction are detected with the time. Similar but different to amperometry, in voltammetry, the signal is obtained by applying a set of varying potential and measuring the resulting current.

Voltammetric methods include linear sweep voltammetry, cyclic voltammetry, hydrodynamic voltammetry, differential pulse voltammetry, square-wave voltammetry, alternating current voltammetry, polarography, and stripping voltammetry [3].

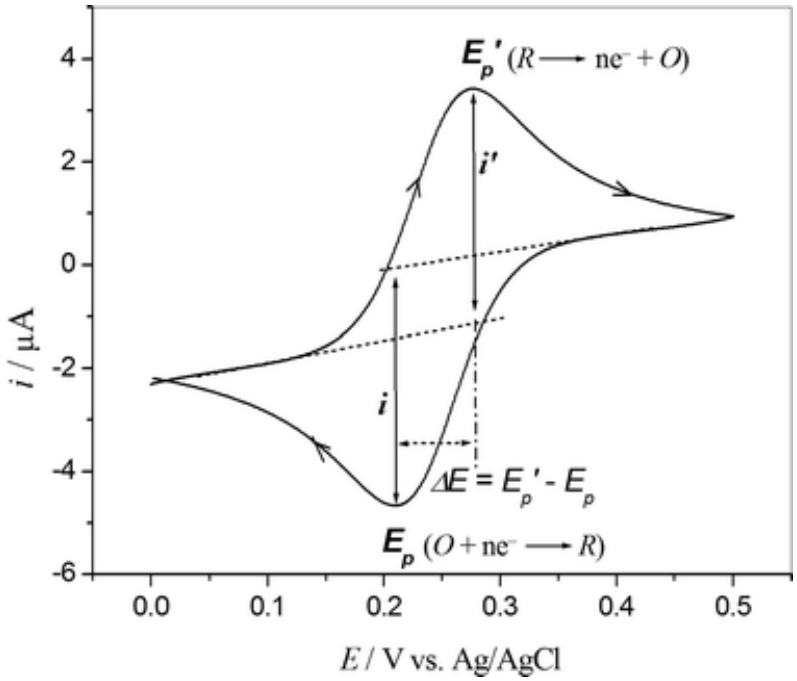

Figure 1.3 Typical cyclic voltammogram recorded for a reversible single electrode transfer reaction. Adopt from Ref. [4].

Among them, cyclic voltammetry (CV) is the most widely used electrochemical technique and is often used to study mechanisms and kinetics of an electrochemical reaction. In cyclic voltammetry, the scan starts from initial potential and reverses when the voltage reaches a certain value. Fig. 1.3 gives the CV curve of a typical reversible single electrode transfer reaction, where i' and i are anodic and cathodic peak current, E_p' and E_p are anodic and cathodic peak potential, and ΔE_p is peak potential separation, which represents the electron transfer rate. When the ΔE_p is small enough, the electron transfer is very fast, it can be considered as a reversible reaction. It's known that the anodic current is due to an oxidation reaction, while the cathodic current is due to a reduction reaction. In a redox system, there is no exchange of ions between electrode and electrolyte. Thus, the electrode is required to be made of an inert metal, such as platinum or gold. Meanwhile, the electrolyte contains a redox probe which has two substances: electron donors and

electron acceptors. Here we take Fe^{3+}/Fe^{2+} system as an example. The forward scan is the oxidation from Fe^{2+} (electron donor) to Fe^{3+} (electron acceptor), and the current flow is from electrolyte to electrode. When the scan is revised, it is the reduction of Fe^{3+} to Fe^{2+}, and the current flow is back to electrolyte from electrode. In an ideal reversible system, the electrochemical oxidation/reduction reactions are governed by the Nernst equation:

$$E = E^{0'} + \frac{RT}{nF} ln \frac{[O]}{[R]} \quad (1.1)$$

where $E^{0\prime}$ is the formal redox potential, which is determined by the equation $E^{0\prime} = (E_p + E_P')/2$, E is the redox potential, n is the number of electron transfer, [O] is the concentration of oxidized form and [R] is the concentration of reduced form at the electrode surface. F is the Faraday's constant (96485.309 C mol^{-1}), R is the standard gas constant (8.314510 J K^{-1} mol^{-1}) and T is the absolute temperature in Kelvin.

The peak current i_p in this reversible system at 278 K is given by Randles-Sevcik equation:

$$i_p = 2.69 \times 10^5 \, n^{2/3} A D_0^{1/2} v^{1/2} c_0^* \quad (1.2)$$

where A is the electrode area (cm^2), D_0 is the diffusion coefficient (cm^2/s), v is the scan rate (V/s) and c_0^* is the bulk concentration (mol/cm^3). This equation indicated a linear relationship between the peak current and square root of the scan rate, which often used to judge the process of diffusion control system.

The electrochemical impedance spectra often consist of a semicircle part at high frequencies and a linear part at lower frequencies as shown in Fig. 1.4. The linear part represents the diffusion limited process. The semicircle part corresponds to the electron transfer limited process, which shows the blocking behavior of electrode for charge transfer. When electrochemical inert

molecules were attached onto the electrode surface, they would form an electron transfer blocking layer and hence increase electron transfer resistance. The diameter of semicircle exhibits the electron/charge transfer resistance of electrode surface which is an important parameter in the measurement of electrochemical impedance. The Nyquist plots of electrochemical impedance spectra outline the real part of impedance (Z_{Re}) versus the negative of the imaginary part ($-Z_{Im}$). Inset of Fig.1.4 is the Randles model equivalent circuit for the electrochemical impedance data [5, 6], which includes the electrolyte resistance between working and reference electrodes (R_s), the double layer capacitance of electrode/electrolyte interface (C), Warburg impedance (Z_w) causing by the diffusion of ions from the electrolyte to the interface and electron transfer resistance (R_{et}). Electrochemical impedance spectroscopy is a rapid and non-destructive method that possesses the ability to study the interfacial behavior of a wide range of materials in electrochemical system [6, 7]. More importantly, this technology is very useful to monitor the bio-recognition event through capacitance, reactance and/or resistance changes at the modified electrode surface [5].

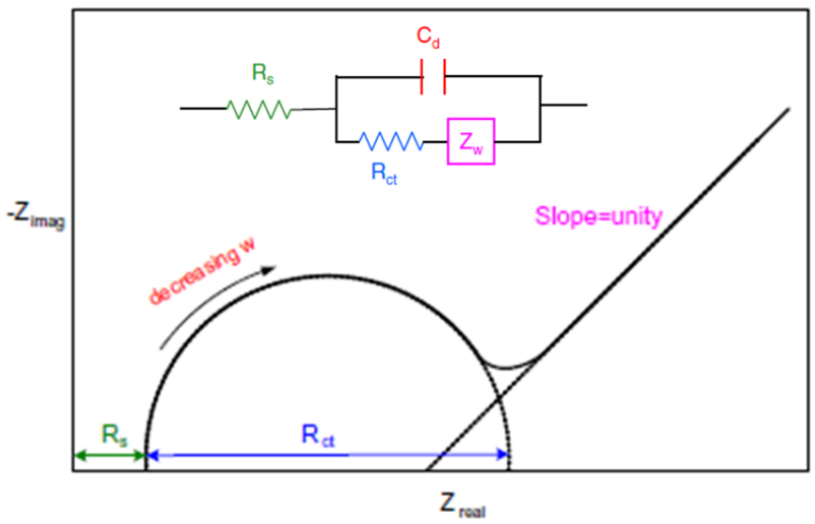

Figure 1.4 The Nyquist plots of electrochemical impedance spectra. Inset: the Randles model equivalent circuit for the electrochemical impedance data. Adopted from Ref. [6].

1.1.3 Electrocatalysis

Electrocatalysis, as a branch of electrochemistry devoted to changing the kinetics of an electrochemical reaction and in some cases also the mechanism via the use of electrocatalyst on an electrode surface, plays an important role in the development of a large amount of research areas, including electroanalytical sensors, water electrolysis, fuel cells, and solar cells [8].

The increases of the rate of an electrochemical reaction can be achieved by reducing the over-potential, which is the extra potential over the theoretical potential that required for the reaction. Compared to usual homogeneous catalysis, electrocatalysis is considered as a more complex process in terms of the description of reaction rate. As shown in Fig. 1.1, an electrified solid-liquid interface is established between the electrolyte and the electrode. A simple oxidation-reduction process involves several steps including mass transfer, adsorption/desorption, and electron transfer. The over-potential is a consequence of electrolyte resistance, electron transfer resistance and mass transfer resistance [1]. In order to minimize the over-potential, much effort has been devoted to the development of efficient electrocatalyst.

In general, electrocatalysts consist of noble metals (Pt, Pd, Ru, and Au) and their conducting support materials (carbonaceous materials). The performance of an electrocatalyst depends strongly on the nature of the noble metals and support materials (chemical composition, size, shape, surface chemistry and electrochemical properties) as well as the interactions between them.

In addition, the electrode material and surface morphology are also considered as important factors which will influence the behavior of electrochemical reactions. Similar to electrocatalyst, the nature of electrode not only controls the active surface sites for the reactions but also the electron transfer pathways. Generally speaking, in order to enhance the efficiency of an electrochemical reaction, there are some common key points that need to be noted both for the electrocatalyst and

electrode, for example high active surface area, good mechanical, chemical, and electrochemical stability. In order to achieve these aims, nanotechnology has its natural superiority [9, 10].

1.1.4 Electrochemical biosensor

A biosensor is a device that transfers a biological event to a measurable signal. It often consists of a biological recognition element which must be selective, a transducer to generate the measurable signal and a signal processing unit [11]. Biosensors are excellent analytical tools for the detection of a wide range of biological elements, such as nucleic acids, antibodies, enzymes, bacteria, viruses and so on [12]. Currently, the biosensors can be performed in cell cultures, human samples, food samples and environmental samples [13]. As an important part in biosensor, the attachment of the target biological elements to the surface of biosensor can be achieved by various methods, such as adsorption, encapsulation, entrapment, covalent binding, cross-linking and so on [14]. Once the interaction between target biological elements and recognition elements is defined, different types of transducers can be utilized to convert the recognition events into a digital signal proportional to the presence of the target analyte in the sample. The election of a suitable transducer is extremely important to a biosensor. The most common methods include electrochemical, optical, piezoelectric, magnetic, et al. Among them, electrochemical technique is the most widely used type due to its numerous possibilities[15]. Researchers from different fields in worldwide are interested in developing novel biosensors with high sensitivity and excellent selectivity [16].

Electrochemical biosensor is two or three electrodes electrochemical cell, which can transfer a biological event to an electrochemical signal. They often contain a biological recognition element on the electrode surface which reacts with the analyte and then produce electrochemical signal [17]. Electrochemical biosensor plays an important role in biosensor field because of their intrinsic

advantages such as high sensitivity, fast response, easy operation, favorable portability and low cost.

Based on the method of the recognition process, electrochemical biosensors can be divided into biocatalytic sensors and bioaffinity sensors. Biocatalytic sensors use the biological recognition element (e.g. enzyme, electrocatalyst) which can produce electroactive species, while bioaffinity sensors monitor a binding event between the biological recognition element and the analyte [3, 18].

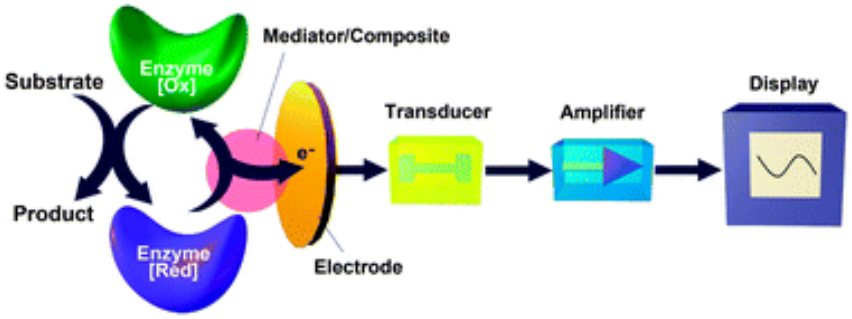

Figure 1.5 Basic elements of an enzymatic biosensor. Adopted from Ref. [19].

As shown in Fig.1.5, enzymatic biosensors using enzymes as the recognition element combine electrochemical technology with specificity of enzyme have provided great opportunities for novel strategies in the early diagnosis [20]. The enzyme oxidizes the active compound and generates detectable electrochemical signal. The direct electron transfer between the redox active center of enzyme and the electrode without mediators is significant to the development of enzymatic biosensor. However, because the active center of the enzyme is surrounded by a thick protein layer and located deeply in hydrophobic cavity of molecules, the direct electrochemistry of enzyme is very difficult [21, 22]. Therefore, the use of an electrical connector or mediator is required to shift electrons and enhance the electron transportation from enzyme onto electrode surface.

Bioaffinity sensors, such as DNA biosensors and immunosensors, are based on the recognition and specific binding which happens between two biomolecules. One of the two biomolecules is initially bonded onto the transducer, and will be used to capture the target analyte during the detection. Bioaffinity electrochemical sensors are the most widely used type of bioaffinity sensors, which collect the measurable electrochemical signal produced by the biomolecular recognition [23]. DNA biosensor, based on DNA–DNA hybridization, is of considerable recent interest due to its simplicity, speed, and economical assay for the diagnosis of genetic and infectious diseases and for the detection of genome mutation [24]. When it comes to electrochemical biosensing, a single-stranded DNA (ssDNA) is attached onto an electrode for sensing its complementary DNA. An electrochemical signal is directly given by electrochemical reactions caused by the DNA hybridization. However, it's difficult to collect sensitive electrochemical signals for the DNA electrochemical sensor based on the electrochemical oxidation of nucleobases (primarily purine) [25]. There are two main reasons: 1) the electrochemical oxidation of purine happens occurs at high potentials and is characterized by a low electron-transfer rate; 2) the peak current is too small to be investigated on classic electrode unless using mercury based electrode. In order to solve these problems, electroactive indicators such as a cationic metal complex or intercalating organic compound have been widely used to improve the electrochemical response in DNA electrochemical biosensor. Some other indicator-free designs involve the attachment of a redox group onto the target DNA [26]. Immunosensors, based on a specific interaction of antibodies with their corresponding antigens, provide a sensitive and selective tool for the detection of many kinds of proteins. Although the antibody-antigen interaction has high specific, most of them do not yield sensitive measurable signals [27].

The performance of electrochemical biosensors can be improved by the applications of nanotechnology in all their three components ranging from the recognition component, the transducer to the signal processing system [10]. Meanwhile, some significant advantages owing to the small size of nanomaterials allow the fabrication of multiplex systems and offer the possibility to design device which can detect single molecule [15].

1.2 Introduction to nanomaterials

Nanotechnology, as a new branch of science that deals with materials with nanosize, is having a profound effect on the development of many fields including energy delivery and storage, device, biomedicine, functional materials, sensing, and so on. Nanomaterials and their composites exhibit many remarkable properties that are different from those of bulk form and are expected to lead to groundbreaking discoveries both in science and engineering in next decade [28].

1.2.1 Surface effect and quantum effect of nanomaterials

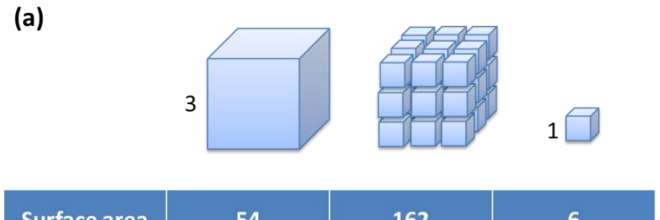

Surface area	54	162	6
Volume	27	27	1
Surface to volume ratio	2	6	6

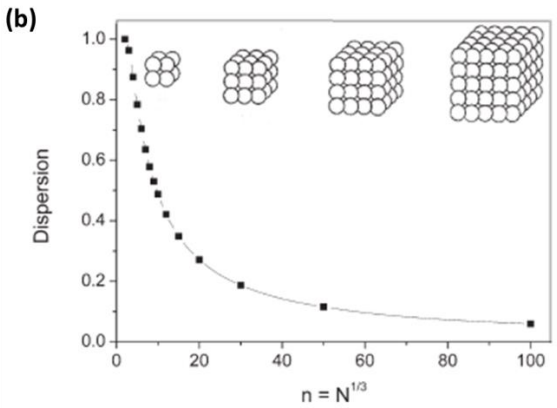

Figure 1.6 (a) An illustration to depict the increase in surface to volume ratio with a decrease in size; (b) Evolution of the dispersion F as a function of n for cubic clusters up to n = 100 ($N=10^6$), F is the fraction of atoms at the surface of cubes, n is the amount of atoms along an edge of cubes, N is the total number of atoms N in cubes. Adopted from Ref. [29].

When the materials size is reduced to nanoscale, the interesting changes in chemical and physical properties are due to two principal factors: surface effect and quantum effect.

As it can be observed in Fig. 1.6a, if a large cube is divided into several individual small cubes, the total volume is same, but the total surface area is greatly increased, therefore, the surface to volume ratio increases. In case of nanomaterials, the surface to volume ratio increase dramatically compared to their bulk form. This significant increase brings several unique properties to nanomaterials. Because of their high surface to volume ratio, reactions are able to take place at greater number of sites at the same volume, and thus results in higher reactivity. On the other hand, the atoms at surfaces of materials have fewer neighbors compared to atoms in the interior of the materials, thus they possess unsatisfied bonds and are less stabilized. Decreasing in size (amount of atoms) results in an increases in the fraction of atoms at the surface (Fig. 1.6b), which means that the smaller nanomaterials has higher free energy and higher reactivity [29].

In nanomaterials, the electrons are confined between two potential barriers rather than free to move within their respective bands in all three directions in the bulk materials. As a result, electronic energy levels are not continuous but are replaced by a series of discrete electronic energy levels. This phenomenon is called quantum confinement, which leads to an increase in the band gap energy and a blue shift in light emission with decreasing size (Fig.1.7). As a result, the electrical and optical properties of nanomaterials become size and shape dependent [29, 30].

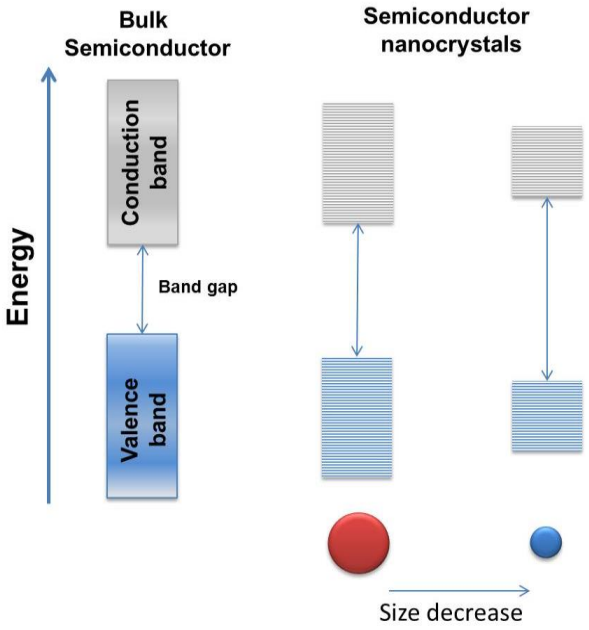

Figure 1.7 Schematic representation of the quantum confinement effect on a semiconductor material.

These essential features of nanomaterials make it possible to turn chemical and physical properties to specific applications by controlling their size, shape and chemical composition.

1.2.2 Classification and fabrication of nanomaterials

Based on the number of dimensions which are not confined to the nanoscale rang, nanomaterials can be classified into four categories: zero-dimensional (0D), one-dimensional (1D), two-dimensional (2D) and three-dimensional (3D) nanomaterials [10].

Table 1.1 Classification of nanomaterials

0D nanomaterial	1D nanomaterial	2D nanomaterial	3D nanomaterial
Metal nanoparticle, quantum dot, hollow nanosphere, core-shell nanoparticle	Nanotube, nanowire, nanorod, nanotube array, nanowire array	Nanofilm, nanosheet, nanoplate	Ordered mesoporous material, ordered macroporous material, multi-nanolayer

Zero-dimensional nanomaterials usually refer to the materials with nano-dimensions in all their three directions, such as metal nanoparticles [31], quantum dots [32], hollow nanospheres [33] and core-shell nanoparticles [34]. One-dimensional nanomaterials have one direction which is out of the nanoscale range. Randomly arranged 1D nanomaterials include nanotubes [35], nanowires [36], nanorods [37], nanofibers [38] and so on, while highly ordered nanomaterials are nanotube array [39] and nanowire array [40]. Typical 1D nanomaterials like carbon nanotubes often have a high aspect ratio due to the long length and small diameter [41]. In 2D nanomaterials, there are two direction are outside the nanoscale range. The family of 2D nanomaterials consists of nanofilms [42], nanosheets [43] and nanoplates [44] with nanometer thickness. Graphene is one of the most popular 2D nanomaterials and has been great extensively studied due to its unique properties so far [22]. In 3D nanomaterials, all three dimensions are out of the nanoscale range. This type of nanomaterials, also known as bulk nanomaterials, can be composed of individual 0D, 1D and 2D

nanostructural elements. Examples of 3D nanomaterials include ordered mesoporous materials [45], ordered macroporous materials [46] and multi-nanolayers [47].

In order to produce nanomaterials with very well controlled properties, there are several points worth noting: size, shape, distribution, chemical composition, crystal structure, surface functionalization, etc. Generally, there are two methods to produce nanomaterials: top-down methods and bottom-up methods. In the top-down approach, nanoscale materials with desired size and shape are created from a bulk material by physical, mechanical or chemical methods. Common top-down techniques involve nanolithography, chemical etching and mechanical milling. Currently, the most used top down approach is nanolithography technique, which includes different forms, like electron-beam lithography, X-ray lithography, atomic force microscopic nanolithography, nano-imprint lithography, and scanning probe microscope lithography. Nanolithography has been widely used to fabricate nanochips and nanoarrays. Although a large amount of one dimensional nanostructures have been prepared with nanolithography, this technique is not cheap and not suitable for the fabrication of complex structures. Additionally, it's very easy to cause the imperfection and damage to the produced nanomaterials for this approach [48, 49].

The bottom-up approach is to build nanomaterials from atomic or molecular species, allowing for the fabrication of complex nanostructrues ranging from 0D to 3D through chemical or biological process. In bottom-up approach, small building blocks self-assemble into the final nanostructures using covalent and/or noncovalent bonds. Compared to top-down approach, this technique can easily make nanomaterials with less defects, desired sizes and shapes. Generally, the bottom-up approach can be sub-divided into gas phase and liquid phase techniques.

Chemical vapor deposition (CVD) is one of the most effective gas phase processes used to prepare nanoscale materials. This method is referred to a chemical reaction happened between a substrate and a gaseous precursor. CVD method has been widely used for the production of carbon based nanomaterials and is a promising method for industrial scale-up synthesis. Other gas phase techniques include laser ablation, plasma spray, and arc discharge.

In liquid phase methods, the most established one is sol-gel processing, which is based on hydrolysis and condensation reactions from various molecule precursors to generate nanomaterials. Sol-gel technique has a long history to make ceramic materials and offers several advantages like up-scalable, low operating temperature and low cost. In the area of nanotechnology, this method is employed to prepare oxide nanomaterials. Common sol-gel precursors are metal alkoxides and inorganic salts. After the hydrolysis and polycondensation reactions of precursors, a stable colloidal solution (sol) is formed for the further formation of a gel-like three dimensional network. Then, the final nanoscale products can be prepared after various processes like drying and thermal treatment. High purity and uniform oxide nanomaterials with a variety of shapes such as nanoparticles, nanofibers, nanofilms and nanoporous have been prepared with sol-gel technique. Additional liquid phase methods include hydrothermal, sonochemical and microemulsion processing [48-51].

Hydrothermal processing can be defined as chemical reactions in the present of aqueous or non-aqueous solvents at high temperature and high pressure in a closed system. This technology is suitable for the processing of advanced nanomaterials covering metal, metal oxides, titanates, carbon, silicates, and nanocomposites for a wide variety of nanotechnology applications [52, 53].

In sonochemistry, a powerful ultrasound radiation (20 kHz to 10 MHz) is applied in chemical reactions and processes. It is known that sound waves consist of a series of compressions and rarefactions caused by the vibrational motion of the molecules within a solution through which they are traveling. At sufficiently high powers, cavitation bubbles containing small amounts of solvent vapor will form during the rarefaction cycles and do not fully collapse during the succeeding compression cycles. The bubbles grow in size through the period of a few subsequent cycles to an equilibrium size. This process is known as rectified diffusion. These bubbles will collapse in a process known as acoustic cavitation when they become unstable (Fig. 1.8). A large amount of energy is released almost instantaneously. Depending on the ultrasonic frequency, localized "hotspot" with extreme temperatures (~5000 K) and pressures (~1000 bar) as well as fast heating/cooling rates (10^{10} K s^{-1}) can be generated and a high velocity jet of liquid can be formed within each bubble at the point of cavitation bubble collapse. The driving force in sonochemistry is acoustic cavitation, which can be used to enhance the rate of a chemical process in liquid [54]. This technique has been used to produce a large volume of nanomaterials since the unique conditions produced by acoustic cavitation can facilitate the formation of very small nanoparticles and allow the reactions to occur under normal conditions that would otherwise require high temperatures, high pressures, or long reaction times [55, 56].

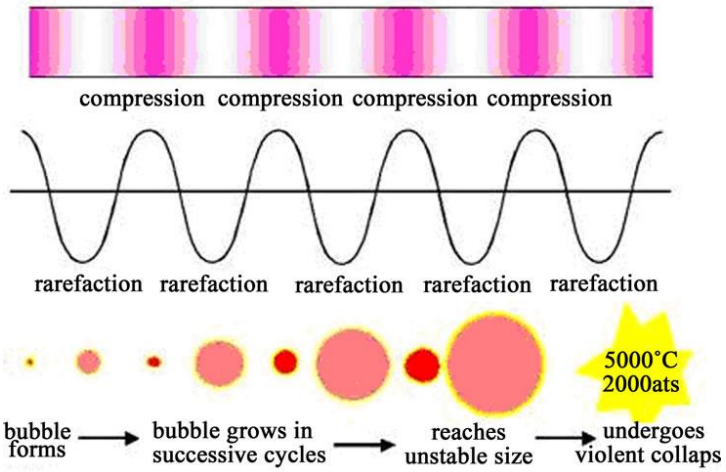

Figure 1.8 The process of acoustic cavitation. Adopted from Ref. [54].

Chemical/electrochemical depositions of metal, alloy nanoparticles and nano-semiconductors play an important role in the development of the fields of energy, environment and biomedicine [57]. Chemical deposition is an autocatalytic method of depositing a desired metal from metal ions by a reducing agent onto a substrate in a controlled size, shape and distribution. Chemical deposition is a powerful tool in the production of novel functional nanomaterials and can be easily combined with other nanofabrication methods to provide possibility for the formation of desired nanoscale features. Common reducing agents used in chemical deposition include hypophosphite, borohydride, alkylamine boranes and hydrazine. Each agent requires different reaction conditions [58]. In electrochemical deposition, oxidations and reductions take place on anode and cathode respectively. The desired metals or alloys are coating on to the surface of cathode (working electrode) by the reduction of metal ion or its complex from an aqueous or organic electrolyte. Compared to chemical deposition, electrochemical deposition needs an external source of electric current to reduce metal ions [59]. According to Nernst equation, the potential E of the electrode can be determined as a function of the concentration of the products and reactants in the equilibrium state:

$$E = E^0 + \frac{RT}{nF} ln \frac{[O]}{[R]} \tag{1.3}$$

where E^0 is the standard electrode potential.

The mass deposited on the cathode (working electrode) during the electrolysis can be calculated from Faraday's law:

$$m = \frac{QM}{nF} \tag{1.4}$$

where m is the mass of the deposit on the electrode (in grams), Q is the total electric charge (in coulombs) during the process [1]. For the fabrication of nanomaterials, electrochemical deposition

has some advantages compared with other conventional methods, such as ability to achieve atomic deposition, low cost, fast reaction rate, high purity, ability to coat surface uniformly, easy to produce nanocomposite and so on. Various nanostructures (nanoparticles, nanowires, nanotubes, amorphous film, etc.) have been obtained through controlling the reaction parameters during electrochemical deposition [60].

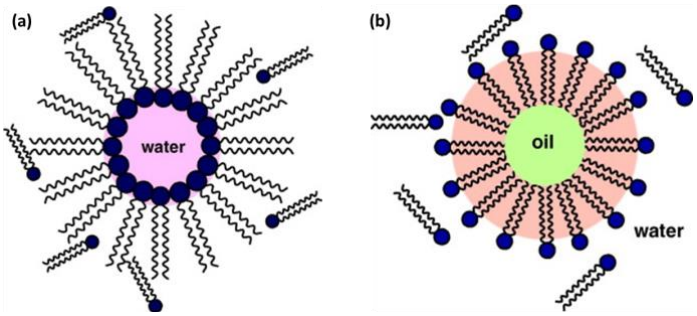

Figure 1.9 (a) Water in oil microemulsion; (b) Oil in water microemulsion. Adopted from Ref. [61].

Microemulsions are nanosized water/oil droplets dispersed in oil/water phase and stabilized by surfactant molecules (Fig. 1.9). This water in oil or oil in water micromulsions have been employed to prepare uniform and size controlled metal nanoparticles, metal oxides, core-shell nanoparticles, and polymeric nanoparticles [61].

Microbial synthesis refers to a green chemistry approach to make nanomaterials (gold, silver, gold-silver alloy, quantum dots, magnetite nanoparticles, etc.) by microscopic organisms, such as bacteria, viruses, yeasts and so on. In recent years, this method has attracted a great deal of attention due to a growing concern for the development of environment friendly methods [62].

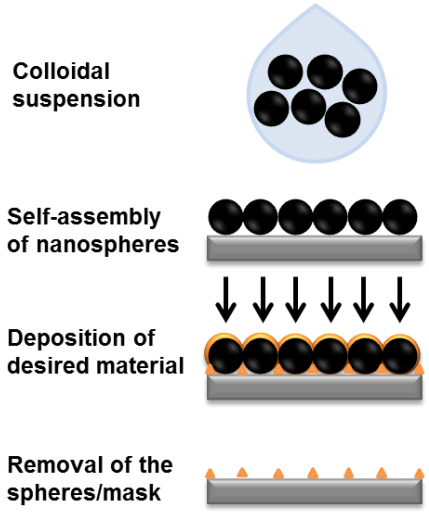

Figure 1.10 Schematic illustration of the nanosphere lithography process.

In order to combine the advantages of different approaches, various hybrid approaches have been proposed by many researchers to fabricate advanced nanomaterials. Take nanosphere lithography as example, this technique is based on two

steps, the first of which is the preparation of a colloidal crystal mask from a suspension containing monodisperse spherical colloids. The desired material (Au, Ag, etc.) is then deposited through the mask. After the removal of the mask, a nanopattern substrate with well-defined size, shape and spatial order is formed (Fig. 1.10). Nanosphere lithography is a straightforward and inexpensive technique to produce a wide variety of one, two, or three-dimensional nanoarrays [51, 63].

1.3 One dimensional nanotubes

1.3.1 Carbon nanotubes: structure and fabrication

Carbon nanotubes (CNTs), as a new class of materials, have been considered as a hot topic in many research areas and have a profound impact on a wide range of applications because of their unique electronic, excellent chemical, and outstanding mechanical properties [64]. CNTs are made of cylinders of sp^2–hybridized carbon atoms with several nanometers in diameter and many microns in length. There are two classes of CNTs, single-walled carbon nanotubes (SWNTs) and multi-walled carbon nanotubes (MWNTs). SWNTs can be considered as one rolled up graphene sheet, while MWNTs are concentric tubes separated by about 0.34 nm of two or more rolled-up graphene sheets [65, 66]. SWNTs have very unique electrical properties, depending on the chirality of the wrap, they can behave as either metals or semiconductors [67]. Here, we define a chiral vector Ch on a hexagonal lattice as $na_1 + ma_2$, where a_1 and a_2 are the unit vectors of the hexagonal lattice, integers n and m are the numbers of unit vectors along two directions of the unrolled graphene sheet, chrial angle θ is defined as the angle between the vector Ch and the (n, 0) direction as shown in Fig. 1.11. Generally, three types of SWNTs can be formed, armchair SWNTs (n=m, $\theta=30^\circ$), zigzag SWNTs (m=0, $\theta=0^\circ$), and chiral SWNTs ($n \neq m$, $n>m, 0^\circ<\theta<30^\circ$) [68]. The value of (n-m) is related to the electronic properties of nanotube, SWNT often shows metallic conductivity when

it is fully benzenoid (e.g. armchair SWNT). It's found that SWNT is metallic if (n-m) is a multiple of 3, otherwise, it is semiconducting [69].

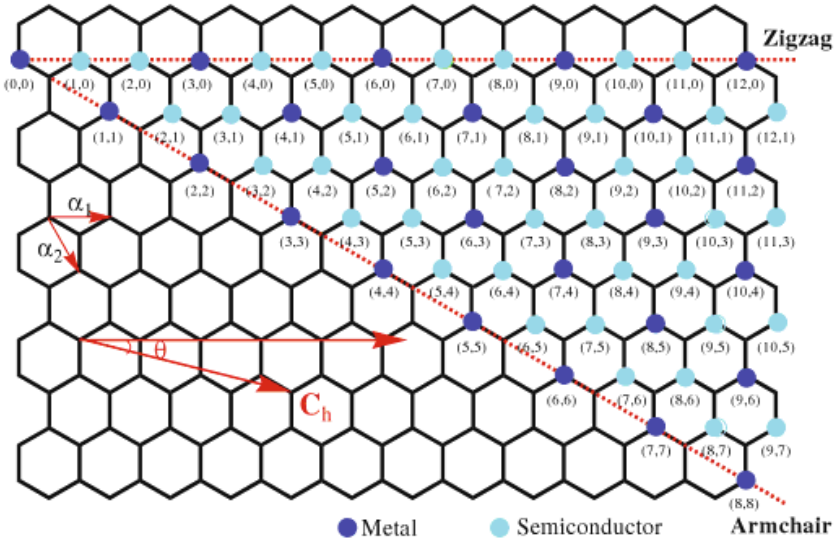

Figure 1.11 Schematic diagram of the chiral vector on the graphene sheet. Adopted from Ref. [70].

Since the discovery of carbon nanotubes, researchers have developed many different methods to produce CNTs. Currently, there are three main methods: arc discharge, laser evaporation and chemical vapor deposition. Arc discharge and laser evaporation are high temperature preparation techniques, and are first used to produce CNTs. Arc-discharge remains as an important method of carbon nanotube synthesis, the carbon nanotube discovered by Iijima in 1991 was prepared using this technique, the first synthesis of single walled carbon nanotube in 1993 was also using this method [71, 72]. In this technique, an electrical arc between two graphite electrodes was used to vaporize the graphite target at very high temperatures(~4000º C) [73]. Although the crystallinity of arc-grown CNTs is very high, many kinds of graphitic debris are also formed. The laser evaporation process was developed by Smalley and co-workers in 1995 [74], which is technically similar to the arc discharge method. The process of laser evaporation utilizes a high power laser to

vaporize graphite target. Carbon nanotubes produced by laser ablation of high purity but the yield is very low. These two methods also suffer from some other disadvantages, such as costs are high, dimensions of the tubes can't be precisely controlled, and scaling up is often very difficult [75]. Nowadays, the most popular and widely used method of producing CNTs, because of its low cost, high yield, and ease of scale-up [76], is CVD method. In this process, thermal decomposition of hydrocarbon vapor (e.g. methane, acetylene, xylene, benzene, carbon monoxide etc.) which diluted in the stream of inert gas in the furnace system is catalyzed by a metals catalyst (e.g. Fe, Co, Ni, etc.) deposited on a substrate (e.g. silicon, alumina, $CaCO_3$, magnesium oxide, etc.) [77-80]. The two widely-accepted growth mechanisms for CNTs growth in CVD method include tip-growth model and base-growth model (Fig. 1.12). Hydrocarbon vapor decomposes into carbon and hydrogen species when it gets in contract with the catalyst metal. When the interaction of catalyst with substrate is weak, hydrocarbon decomposes on the top of the catalyst surface. Carbon dissolves in the catalyst particle and diffuses down through the particle. The as-dissolved carbon precipitates out across the bottom of the catalyst and crystallizes in the form of graphitic cylinder. This is called tip-growth model as shown in Fig. 1.12(a). On the other hand, when the interaction of catalyst with substrate is strong, carbon diffuses upward, and CNT grows from the metal catalyst (Fig. 1.12(b)) [81, 82].

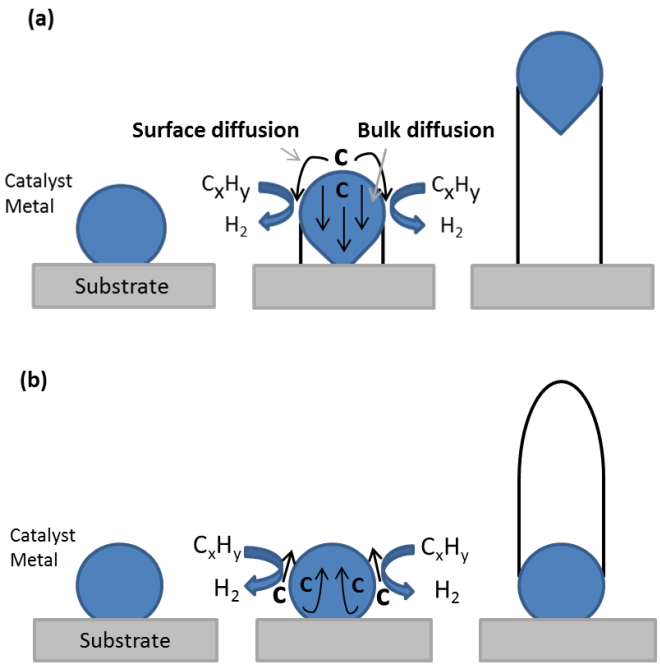

Figure 1.12 Two types of CNT growth: (a) tip-growth model, (b) base-growth model.

The characteristics of carbon nanotubes produced by CVD method can be influenced by many parameters such as temperature, operation pressure, reaction time, hydrocarbon, catalyst, and substrate [83, 84]. By adjusting these parameters, the diameter, length, orientation, alignment, purity, yield and quality of CNTs can be controlled. The temperature plays an very important role in CNT growth, general experiments prove that low-temperature CVD (600-900°C) yields MWNTs, whereas high temperatures (900-1200°C) gives SWNTs. Therefore, it is possible to selectively grow SWNTs or MWNTs if other parameters are fixed [85]. Formation of SWNTs or MWNTs also can be controlled by proper selection of catalyst materials and their concentration. Basically, lower concentration and small size (few nm) favor SWNTs growth, whereas high concentration and big size (few tens nm) exhibit MWNTs formation. [86-88]. The morphology and the quality of produced CNTs strongly depend upon the substrate materials, same catalyst may work differently on different kinds of substrate. The use of various substrates allows CNT growth in several structural forms, like straight, branched, coiled, aligned or films [89-91]. Besides temperature, catalyst and substrate material, carbon source also has an detrimental effect on the morphology of carbon nanotubes [92]. Thus, CVD method provides the possibility to design special types of CNTs which may bring new development to the area of nanomaterials.

1.3.2 Electrochemistry of carbon nanotubes

In the past few years, thousands of papers have been published in the field of electrochemistry of carbon nanotubes. A large body of work suggests that the electrochemical activity of sidewalls and ends of the tubes is very different [93]. Compton et al. studied the redox reaction of 1 mM ferricyanide at different kinds of electrodes, as shown in Fig. 1.13b, they found that the electrochemical behavior of CNTs is similar to the edge plane of highly ordered pyrolytic graphite (HOPG) [94, 95]. They also indicated that the pristine sidewalls of CNTs equate to the basal plane

of HOPG and the open ends or tips of CNTs have fast electron transfer rates and act as the edge plane of HOPG (Fig. 1.13a). The defects on the open ends are considered responsible for the electrochemical activity of CNTs [96, 97].

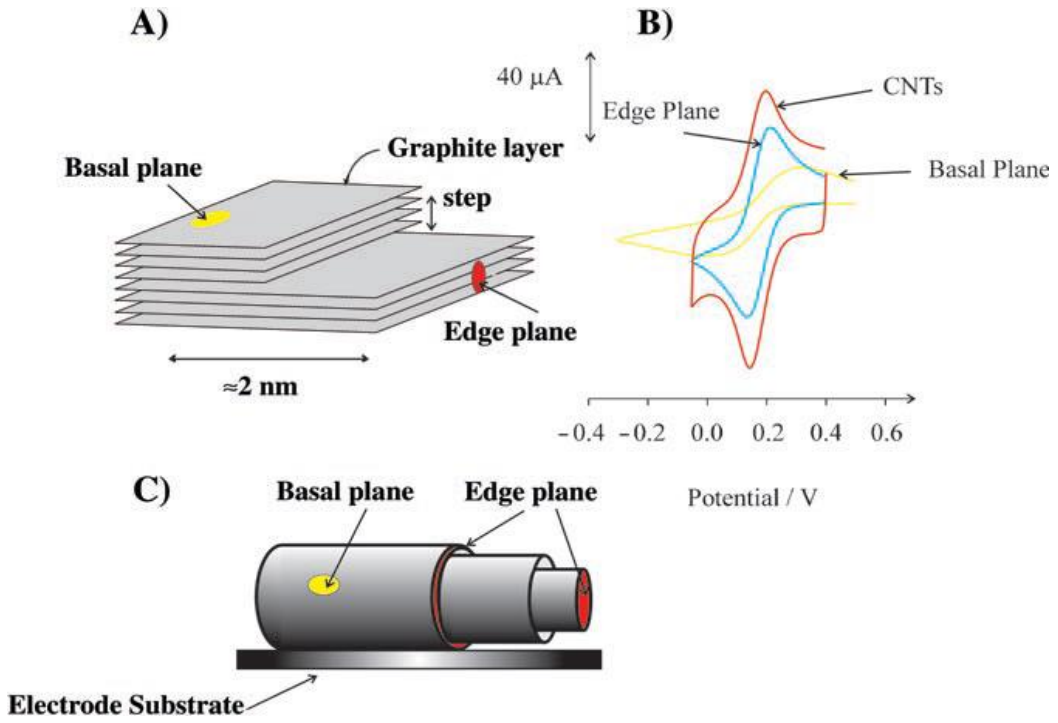

Figure 1.13 (a) Schematic representation of a crystal of highly ordered pyrolytic graphite where the layers of graphite have an interlayer spacing of 3.35 Å. (b) The difference in the voltammetric response for the reduction of ferricyanide in an aqueous solution using basal-plane and edge-plane pyrolytic graphite electrodes. Note the identical response for the CNT-modified electrode compared with the edgeplane pyrolytic graphite electrode. (c) A single MW-CNT on an electrode surface where the edge-plane-like sites are shown at the end of the tube and along the tube axis. Adopted from Ref. [97].

However, there are many factors governing electrochemistry of carbon nanotubes, thus some fundamental issues still need to be addressed: (1) Whether the edge plane like defects on the open

end of the tubes are the only important defects which can affect the electrochemical activity of CNTs, or the defects on the sidewalls also can make contribution. Is this dependent on the type of CNT employed? (2) Do different nanotube orientations and arrangements have different activity? An impartment work to study the role of nanotube tips and sidewalls, and their oxidation states in the electrochemistry of CNTs was carried out by Gong and coworkers. In their experiment, super long (~5 mm) vertically aligned carbon nanotubes (SLVA-CNTs) were connected to a copper wire to form a CNT electrode (Fig. 1.14 step 1). The CNT electrode with only the nanotube tip exposed was prepared by thoroughly masking the CNT arrays with a non-conducting polymer and then partially cutting off the polymer coated CNTs (Fig. 1.14 step 2-3). CNT electrode with only the nanotube sidewall exposed was produced by selectively coating the two ends of the polymer coated CNTs (Fig. 1.14 step 4). Then both the electrodes were electrochemical activated in acidic solution by cycling potential scanning to prepare the corresponding nanotube electrodes with oxygen-containing surface functionalities. They found that the relative electrochemical sensitivity to the nanotube tips and sidewalls and their oxidation states varied with the type of redox probe investigated and the redox reaction involved. For example, the CNTs tip and its oxidation state showed an enhanced electron-transfer rate for the faradaic electrochemistry of postassium hexacyanoferrate ($[Fe(CN)_6]^{4-/3-}$). Conversely, the H_2O_2 oxidation was more sensitive to the nanotube sidewall than its end-tip. The electrochemical oxidation of β-nicotinamide adenine dinucleotide disodium salt hydrate (NADH) was found to be more favorable at oxidized tip and sidewall than the basal or edge plane of carbon atoms, similar results was observed for the oxidation of cysteine at the CNT electrodes. The electrochemical behavior of ascorbic acid (AA) oxidation and oxygen reduction was most sensitive to the oxidized tip and least sensitive to the unoxidized sidewall [98].

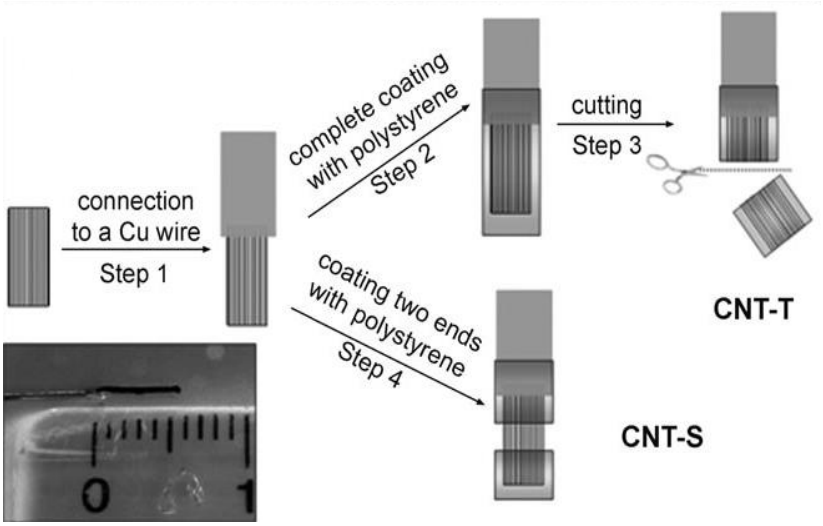

Figure 1.14 A schematic representation of the procedure for preparing the CNT electrodes with only the nanotube tip (CNT-T) or sidewall (CNT-S) accessible to electrolyte. Adopted from Ref. [98].

For SWNTs, the situation is different. Heller and coworkers reported the use of individual SWNT as nano-electrode for electrochemistry study. With only the SWNT sidewall exposed to electrolyte, they obtained a steady state electrochemical current and a very high rate of electron transfer. They also found that metallic and semiconducting SWNTs yielded similar steady-state voltammetric curves [99]. Holloway and coworkers found that the electroactive sites on SWNT also resided at the open ends of the tubes and were considered responsible for the electrochemical activity. Their work demonstrated that the closed-ended, pristine SWNTs could be oxidatively opened by applying a suitable electrode potential. Enhanced electrochemical activity was obtained for the SWNTs after electrochemical opening [100]. Liu and coworkers found that the aligned SWNT arrays showed reversible electrochemistry for ferricyanide oxidation, while a quasi-reversible electrochemistry was observed for randomly arranged acid purified SWNTs. The excellent

electrochemical performance of the aligned nanotube array electrode were attributed to the increased end groups on the electrode [101].

Much of the work on studying CNT electrochemical activity infer the contribution of defects and oxygen containing groups, it turns out that the role of defects and oxygen containing groups is one of the key issues on understanding electrochemistry of carbon nanotubes. And It's possible to change the electrochemical activity of carbon nanotubes by inducing defects or oxygen containing groups on the sidewalls or the open ends of tubes [102]. Nanotubes are not ideal structures but contain some defects which result from structural changes during the synthesis without the introduction of impurity atoms. The unique defect in graphene lattice is so called Stone-Wales defect, which is the consequence of the transformation of four hexagons into two pentagons and two heptagons, and thus is also referred to a 7-5-5-7 defect or 5–7 pair defect [103]. As presented in Fig. 1.15a, the 5–7 pair defect formation can be interpreted as the rotation of a C–C bond in a hexagonal network and thereby induces a local deformation of the graphitic sidewall [104]. These non-hexagonal pairings may cause bends or other structural changes along the CNT axis and thereby provide defects to CNTs for further reactions.

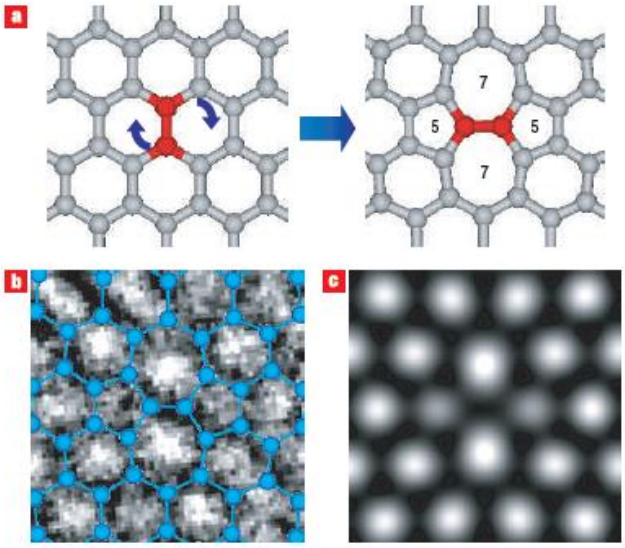

Figure 1.15 Atomic arrangement of the Stone–Wales (SW) model. (a) The SW transformation leading to the 5–7–7–5 defect; (b) HR-TEM image obtained for the atomic arrangement of the SW model; (c) Simulated HR-TEM image for the model shown in (b). Adopted from Ref. [104].

1.3.3 Nitrogen doped bamboo shaped carbon nanotubes (BCNTs)

The doping of carbon nanotubes with foreign atoms, such as boron, nitrogen also can bring structural and electrochemical property changes to carbon nanotubes. The incorporation of boron or nitrogen atoms into the graphene lattice can chemically active the rather passive carbon nanotube surface. Compared to boron doping, nitrogen doped carbon nanotube has received much more attention in many areas, especially in electrochemistry related areas [105].

By controllably placing non-hexagonal pairings or foreign atoms in the graphene lattice of CNT, new structures of CNTs such as coiled [106], branched [107], bamboo-shaped [108] can be synthesized (Fig.1.16). These new forms of CNTs may exhibit novel electrochemical properties, which are different compared to conventional carbon nanotubes and may open a way for future applications [109, 110]. Among them, nitrogen doped bamboo-shaped carbon nanotubes (BCNTs) have become a hot topic of increased interest in the field of carbonaceous materials. The most eye-catching features of BCNTs are their bamboo shaped structure associated properties.

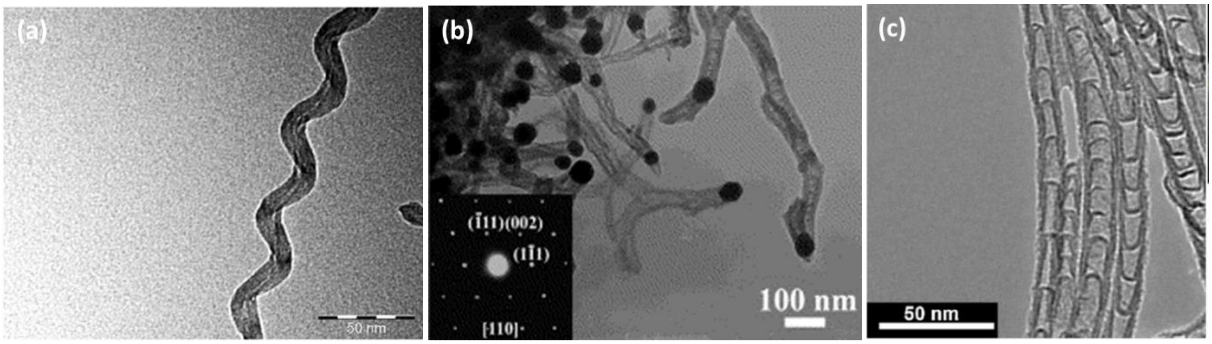

Figure 1.16 (a) Coiled CNTs synthesized on Co-Pr/SiO_2 catalysts with 7.5% Co-2.5% Pr with CVD method. Adopted from Ref. [111]; (b) Multi-branched CNTs on an alkali-element modified Cu/MgO catalys by CVD method. Adopted from Ref. [112]; (c) Bamboo-shaped CNTs synthesized by CVD method using a mixture of C_2H_6/Ar/NH_3 on an alumina supported iron catalyst. Adopted from Ref. [113].

The most wildly used strategy to prepare BCNTs is to incorporate nitrogen during synthesis of the CNT [105], such as the pyrolysis of nitrogen containing organic compounds [114-116] and CVD of nitrogen containing carbon feedstock over a supported transition metal [117-119]. CVD is the most common and straightforward method to synthesize BCNTs. As we known, nitrogen has five valence electrons and carbon has four, an extra electron is brought into the graphene lattice. Thus the local electronic environment of CNT surface layer is changed due to the introduction of nitrogen [120]. X–ray photoelectron spectroscopy (XPS) analysis is often carried out to study the electronic effect of nitrogen incorporation into CNT graphene layers. There are various types of nitrogen can be distinguished in the N1s spectrum of nitrogen doped CNTs: pyridinic nitrogen (398.5 ± 0.2 eV, N atoms substitute a carbon atom of the six member ring and form two bonds with neighboring two carbon atoms), substitutional or quaternary nitrogen (401.2 ± 0.2 eV, N atoms in graphene lattice bonded with three carbon atoms), pyrrolic nitrogen (400.5 ± 0.2 eV, N atoms substitute a carbon atom of the five member ring) and oxidized N species (402.9 ± 0.2 eV, N atoms bonded with oxygen atoms) (Fig. 1.17) [121, 122].

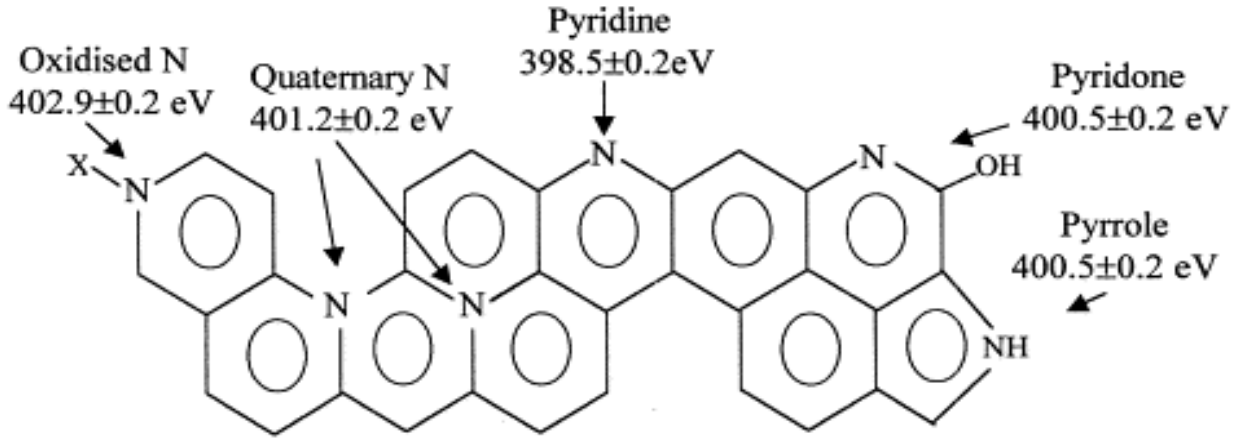

Figure 1.17 Different nitrogen functionalities in a graphitic sheet. Adopted from Ref. [121].

BCNTs have enhanced electronic properties caused by the extra valence electron provided by the incorporation of nitrogen into the graphitic lattice compared to undoped carbon nanotubes. It is believed that BCNTs possess a large amount of structural defects on their surface due to the nitrogen doping and their bamboo structure. BCNTs could provide more active sites for the chemical and electrochemical processes than hollow CNTs and offer new opportunities in the development of many areas, such electronic devices, lithium ion battery, electrochemical biosensors, electrocatalysis and so on [123-125].

1.3.4 Titanium dioxide (TiO_2) nanotube arrays

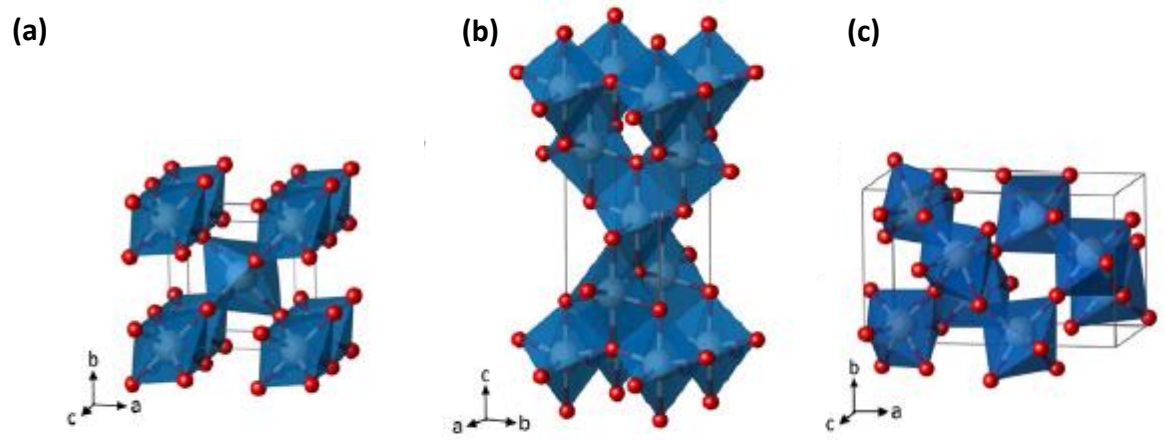

Figure 1.18 Crystal structures of TiO_2 (a) Rutile (b) Anatase (c) Brookite. Ti (white ball) and O (red ball). Adopted from Ref. [126].

Titanium dioxide (TiO_2), known as titania, is the most extensively studied transition-metal oxides in material science due to their properties such as non-toxic, environmentally friendly, corrosion-resistant, biocompatibility, unique ionic and electronic properties. Thus, the applications of TiO_2 cover many areas in industry and medicine [39]. TiO_2 has three types of crystal structures: rutile (tetragonal, Fig. 1.18a), anatase (tetragonal, Fig. 1.18b), and brookite (orthorhombic, Fig. 1.18c).

All of them are networks of distorted TiO_6 octahedra unit, in which Ti^{4+} is at the center and O^{2-} ions are at the corners [126, 127]. When amorphous TiO_2 is annealed, anatase is formed at the temperature from 300- 500 ºC, while rutile is formed at 500 ºC or higher. Brookite can't be formed under normal laboratory conditions but is obtained as a mineral [128].

Nano-sized TiO_2 nanomaterials can be made in different forms, such as nanoparticles, nanofibers, nanotubes and so on. TiO_2 nanotube arrays are vertically aligned on the underlying Ti substrate. Besides the common properties of TiO_2, they have some unique advantages including large surface area, highly ordered one dimensional, one-end open tubular structure and good biocompatibility. Such vertical aligned TiO_2 nanotube array has a broad range of applications. One of the most investigated applications of TiO_2 nanotubes is solar cells. TiO_2 nanotube is one of the most efficient photocatalyst. TiO_2 nanotube also can be applied in Li-ion batteries, gas sensors, and supercapacitors. In biomedical areas, the application of TiO_2 nanotubes is still a very early stage but possess great potentials due to their high biocompatibility, good corrosion resistance in biological environments and nanotubular geometry. TiO_2 nanotubes could influence cell adhesions on their surface and show potential applications as implant materials. Another potential application of TiO_2 nanotubes in biomedical area is drug delivery [129].

During the past few years, a considerable number of different approaches have been employed to synthesize TiO_2 nanotube, such as hydrothermal reactions, anodic aluminum oxide (AAO), atomic layer deposition, electrospining and electrochemical anodization [130]. Among them, electrochemical anodization is a simple, reliable straightforward and efficient process to prepare well-aligned and highly ordered TiO_2 nanotube arrays [130].

Electrochemical anodization is carried out typically in a two electrode system in an electrochemical cell with a suitable electrolyte (Fig. 1.19a). The metal of interest acts as a working

electrode (anode), while an inert counter electrode (usually platinum or carbon) is often used as cathode electrode. The metal is oxidized to a metal oxide when applying a sufficiently high anodic voltage. The whole process is controlled by many anodization parameters. Since the first work of the synthesis of self-ordered TiO_2 nanostructures using electrochemical anodizing process in a fluoride electrolyte by Zwilling and coworkers [131], increased research interest has been devoted to find the optimal electrolyte and experimental parameters to fabricate high quality TiO_2 nanotube arrays. The mechanism of TiO_2 nanotube array synthesis using electrochemical anodization is shown in Fig. 1.19b. The first step is the formation of an oxide barrier layer of TiO_2 on the electrolyte-metal interface due to the anodic oxidation.

$$Ti^{4+} + 2H_2O \rightarrow TiO_2 + 4H^+ \quad (1.5)$$

The large current density observed at the initial stage in Fig. 19c indicates the oxidation of Ti to Ti^{4+}. The followed rapid decrease is attributed to the formation of oxide layer via above hydrolysis reactions.

When constant voltage is applied, because the present of F^- in the electrolyte, a competition between the formation of oxide layer and the dissolution of TiO_2 occurs and the formation of pits can be observed (Fig.1.19b).

$$6F^- + TiO_2 + 4H^+ \rightarrow [TiF_6]^{2-} + 2H_2O \quad (1.6)$$

Thus, at step II, the decrease of current caused by the formation of corrosion pits can be found in Fig.1.19c. In addition, the dissolution rate of TiO_2 at these pits is faster than other areas. As the anodization time increases, pits enlarge and become nanopores. Meanwhile, the interpore regions also undergo the dissolution of TiO_2 and finally breakdown. This event is marked by an increase in current density (Fig.1.19c). Then equilibrium of oxide layer formation and dissolution is established, completely developed nanotubes are formed and the current density achieves a constant value over time [39, 130, 132, 133].

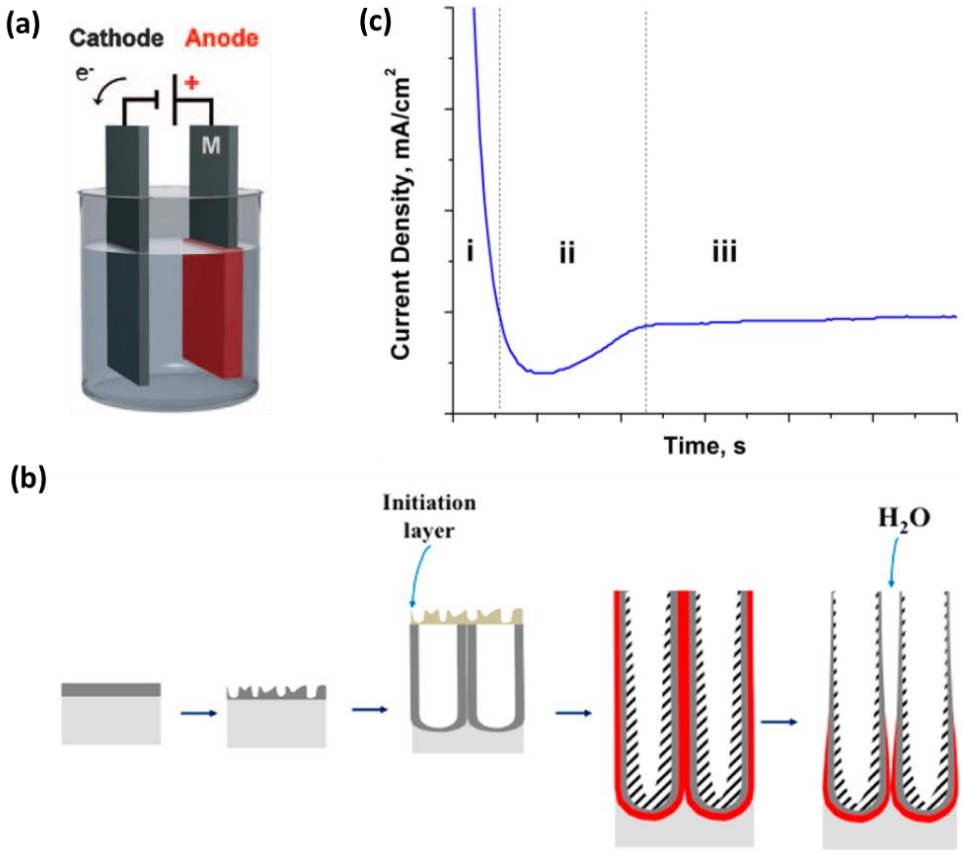

Figure 1.19 (a) The electrochemical anodization process. Adopted from Ref.[39]; (b) Schematic of growth sequence of TiO_2 nanotube growth. Adopted from Ref.[129]; (c) A typical current density vs. time plot produced during the anodization process. Adopted from Ref. [133].

The growth of TiO_2 nanotube array can be influenced by many fabrication factors, including electrolyte, reaction time, applied voltage. It has been found that the length and diameter strongly affect by the electrolyte. Generally, there are two wildly used electrolytes: aqueous electrolyte such as HF or NH_4F^- based electrolyte and organic electrolyte such as ethylene glycol containing F^- ions and H_2O. In aqueous electrolyte, the length of as prepared nanotubes is limited to a few hundred nanometers. However, in organic electrolyte, the nanotubes are much longer. The reason of this phenomenon is that the dissolution of TiO_2 is limited in organic electrolyte since the amount

of H_2O in this type of electrolyte is much less than in aqueous electrolyte. On the other side, due to the high dissolution rate of oxides in aqueous electrolyte, the surface of as prepared nanotubes is not smooth but has some other morphological features. Meanwhile, applied voltage and reaction time also can influence the morphology of formed nanostructures [134].

1.4 Applications of nanomaterials in electrochemistry

The combination of electrochemistry and nanotechnology provides researchers new possibilities to control surface structures of electrode at the molecular level and to fabricate nanosize electrochemical devices with excellent performance. It's believed that nanotechnology has played and will continue to play a vital role in the developments of electrochemistry. The main focus of this thesis, therefore, is on developing novel strategies based on nanomaterials for two impartment areas of electrochemistry: electrocatalysis and electrochemical biosensor.

1.4.1 BCNTs in electrocatalysis of small organic molecules

Small organic molecules like methanol and ethanol are potential fuels for low-temperature fuel cells. A fuel cell is an electrochemical device which converts the chemical energy residing in a fuel into electrical energy. Like other electrochemical cells, fuel cells consist of an anode, a cathode and an electrolyte. At the anode, the oxidation of fuel with anode catalyst occurs and results in positively charged ions and negatively charged electrons. The ions and electrons are drawn from the anode to the cathode through the electrolyte and an external circuit, respectively. At the cathode, the ions and electrons react with oxygen in the present of cathode catalyst to produce water or carbon dioxide. Fuel cells have different types according to their working electrolyte or working temperatures, such as proton exchange membrane fuel cells (PEMFCs), direct methanol fuel cells (DMFCs), phosphoric acid fuel cells (PAFCs), solid oxide fuel cells (SOFCs), molten carbonate fuel cells (MCFCs), alkaline fuel cells (AFCs) and so on. Among them, PEMFCs, DMFCs and

PAFCs are low-temperature fuel cells. Usually, all of them use hydrogen as their fuel except DMFCs. In recent years, interest in the development of direct liquid fuel cell has increased considerable due to its advantages: easy of handling and storing liquid fuel and low operating temperature. These cells are promising technology of choice for portabe electronics powered by miniature fuel cell. As two most common liquid fuels, most investigators are exploring DMFCs, while some are focus on direct ethanol fuel cells (DEFCs) [135, 136]. The corresponding half-cell reactions are showing below:

Anode reaction: $CH_3OH + H_2O \rightarrow CO_2 + 6\ H^+ + 6e^-$ (DMFCs) (1.7)

$CH_3CH_2OH + 3H_2O \rightarrow 2CO_2 + 12\ H^+ + 12e^-$ (DEFCs) (1.8)

Cathode reaction: $nO_2 + 4nH^+ + 4ne^- \rightarrow 2nH_2O$ (1.9)

The catalytic performance of the anode electrodes is an important factor which would influence the performance of the DMFC/DEFC systems. Pt supported on carbon black is the most popular anode electrocatalyst and also the only commercially available anode catalyst so far. Many different approaches have been applied to enhance the electrocatalytic activity of Pt nanoparticles during the methanol/ethanol oxidations [137].

The modification of electrode surface with nanomaterials has been proven to be an effective mean to increase the electrochemically active surface area of the electrode and facilitate faster diffusive mass transport on the electrode surface [138]. Carbon nanotubes are one of the most attractive support materials for electrocatalyst and have been extensively reported to enhance its performance in various electrochemical catalytic reactions, such ethanol oxidation [139, 140], methanol oxidation [141, 142], oxygen reduction [123, 143], carbon monoxide oxidation [144],

formic acid oxidation [145], formaldehyde oxidation [146], carbon dioxide reduction [147], glucose oxidation [148], hydrogen peroxide oxidation [149, 150] and so on. As a new form of carbon nanotubes, nitrogen doped bamboo shaped carbon nanotubes (BCNTs) have demonstrated promising potential for electrocatalyst applications due to their enhanced electronic and electrochemical properties compared to hollow CNTs [151-153]. Additionally, the high density defects on their surface can act as anchor for Pt nanoparticles loading [154]. Thus they provide possibilities to deposit Pt nanoparticles with small size, good dispersion and stabilization without any functionalization process. The aims of chapter 2 and 3 is to investigate the potential of using BCNTs as electrocatalyst support materials of high loaded Pt nanoparticles for improving the activity of the ethanol/methanol electro-oxidation.

1.4.2 BCNTs in bioelectrocatalysis of hydrogen peroxide

Hydrogen peroxide (H_2O_2) is a widely used chemical in clinical and environmental research and also an important contaminant in several industrial products and wastes. The detection of H_2O_2 plays a pivotal role in many biosensors, because they rely on the detection of H_2O_2 generated through an enzymatic reaction. The determination of H_2O_2 often achieves through the collection of the electrochemical signal produced by an electrochemical reaction electrocatalyzed by an enzyme horseradish peroxidase (HRP) (Fig. 1.20) [155, 156].

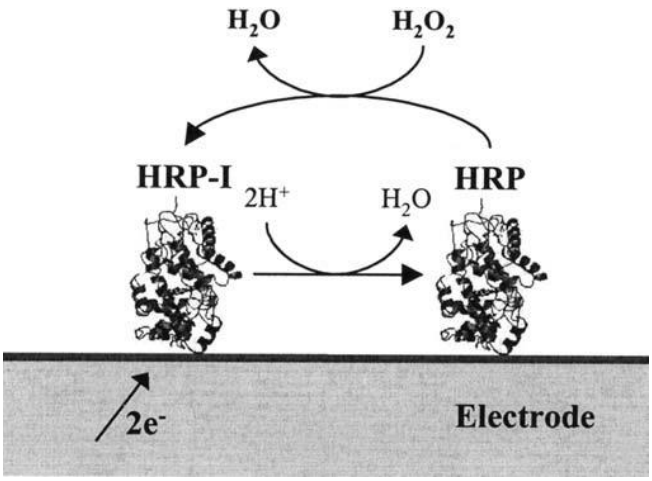

Figure 1.20 The mechanism of electrocatalysis of H_2O_2 by HRP. Adopted from Ref. [155].

The direct electron transfer between the redox active center of enzyme and the electrode without mediators is significant to the development of the practical use of enzymes in biosensors and biofuel cells. However, the active centers of enzymes are surrounded by a thick protein layer and located deeply in hydrophobic cavity of molecules, and the direct electrochemistry of enzyme is very difficult [21, 22]. Therefore, the use of an electrical connector is required to enhance the transportation of electrons. CNTs, with their small size, extraordinary electrochemical properties, and high specific surface area, have been widely used to promote electron transfer between the electrode and the redox center of enzyme [157]. One of the major challenges for the immobilizations of enzyme on CNT is how to achieve stable attachment of enzyme while still retaining their bioactivity. Methods for linking enzyme onto CNTs include noncovalent and covalent interaction. Noncovalent approach can preserve the structural integrity and properties of enzyme as well as provide high surface loading of enzyme [158]. However, the interaction between enzyme and CNTs is not strong, thus the immobilized enzyme may be gradually lost during the use. This limitation can be overcome by adsorbing enzymes onto polymer modified CNT system. Chitosan, as a water-soluble, environmentally friendly, biocompatible polymer, displays excellent film-forming ability, good adhesion and has been often used to construct a bioelectrochemical platform for the direct electron transfer (DET) of enzymes. For example, Zhang and coworkers found that the chitosan-induced solubilization of CNT facilitated the electrooxidation of nicotinamide adenine dinucleotide based on dehydrogenase enzymes [159]. Zhou and coworkers reported the immobilization of enzyme molecules onto chitosan wrapped SWNT film for the development of a new type of very sensitive, stable, and reproducible electrochemical biosensors for the detection of glucose [160]. Ichi and coworkers demonstrated a novel combined chitosan-carbon-nanotube-enzyme biocathode with a greatly enhanced the performance for glucose biofuel

cells by creating a protective microenvironment, preventing the loss of the electrocatalytic activity of the enzyme, and providing good oxygen diffusion [161]. In order to take the advantages of BCNTs, in chapter 4, a hybrid organic-inorganic nanocomposite film of BCNTs/Chi is constructed to immobilize HRP. The direct electrochemical behavior of HRP towards electrocatalytic reaction of H_2O_2 is studied.

1.4.3 TiO_2 nanotubes in electrochemical sensing of glucose

Glucose biosensors account for about 90% of the biosensor marker worldwide. The stability, cost, quality assurance and response time are the major challenges to provide a tight monitoring of glucose levels in blood diagnosis, food industries, bio-processing and biofuel cells [162]. The majority of the current glucose biosensors are enzymatic amperometric glucose biosensors. They are based on using enzyme glucose oxidase (GOx), have been intensively studied in the last few decades and also are the most common devices commercially available [163]. Since the first glucose biosensor developed by Clark and coworkers in 1962 [164], tremendous efforts have been devoted in the development of reliable devices. Glucose biosensors can be historically divided into three generations (Fig. 1.21).

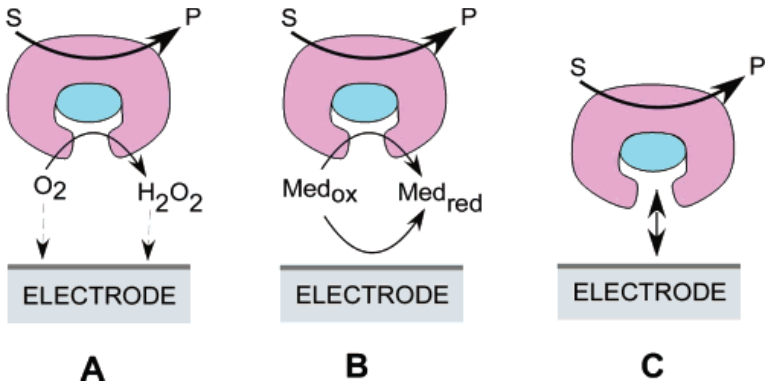

Figure 1.21 Three generations of amperometric enzyme electrodes for glucose based on the use of natural oxygen cofactor (a), artificial redox mediators (b), or direct electron transfer between GOx and the electrode (c). Adopted from Ref. [162].

The first generation is relied on oxygen and detecting the concentration of hydrogen peroxide based on the following reaction. The reduced form of the enzyme ($FADH_2$) is produced through the reduction of the flavin group (FAD) in the enzyme by reaction with glucose. Then, H_2O_2 and the oxidized form of the enzyme GOx (FAD) are generated via the reoxidation of the flavin by oxygen. The amount of hydrogen peroxide produced is measured [163].

$$GOx(FAD) + glucose \rightarrow GOx\ (FADH_2) + gluconolactone \quad (1.10)$$

$$GOx\ (FADH_2) + O_2 \rightarrow GOx\ (FAD) + H_2O_2 \quad (1.11)$$

This method is dependent on the oxygen concentration which is not easy to maintain constantly. In second generation, oxygen is replaced by oxidizing reagents called mediators, which could shuttle electrons from the redox center of the enzyme to the surface of the electrode. Mediators should be nontoxic, stable in both the oxidized and reduced forms, such as quinones, organic conducting salts, dyes, ruthenium complexes, ferrocene, and ferricyanide derivatives [3]. Nanomaterials such SWNTs [35] and gold nanoparticles [165] also have been used as electrical connectors between the electrode and the redox center of GOx.

The goal of the third generation is to eliminate the usage of mediator in the sensors. In this case, the electron directly transfers from glucose to the electrode through the active site of the enzyme. Without mediators, high selectivity can be achieved owing to the low operating potential. In order to avoid the use of mediators, new forms of electrode need to be developed [166].

The enzymatic glucose biosensor is still the mainstream of the biosensors. However, some issues caused by the intrinsic nature of enzymes greatly hinder the development of enzymatic glucose biosensor. Many factors including pH, temperature, chemicals, humidity can influence the activity the enzyme. When exposed to harsh environment, GOx quickly loss its activity. Thus, the stability of enzymatic glucose biosensor is a big challenge and need to be addressed [167]. In order to keep

the activity of GOx on the electrode, various strategies have been applied, such as the usage of polymer [168], sol-gel structure [169], cross linker [170] and so on. However, these efforts only can make sure the enzyme has high activity in a short-time.

Non-enzymatic glucose biosensors, based on the oxidation of glucose catalyzed by electrolycatalysts, avoid the usage of enzyme and can be consider as the third generation of glucose biosensor. Common electrocatalysts for glucose oxidation include transition metal (Pt, Au, Ag, Ni, Cu) nanoparticles, metal oxide (NiO, CuO, CoO) nanoparticles and carbon based nanomaterials (CNT, graphene) [167]. Among them, copper oxide (CuO) is one of the most extensively studied catalysts for non-enzymatic glucose biosensors due to its properties of low cost, non-toxic and easy to produce. Huang and coworkers proposed a non-enzymatic glucose biosensor by immobilizing three different nanostructures of CuO (nanoparticles, nanoplatelets, nanorods), respectively, on a glassy carbon electrode (GCE) in the present of Nafion. The electrochemical results showed that CuO nanoparticles exhibited the highest catalytic effect on glucose oxidation compared to CuO nanorods or nanoplatelets. Amperometric response showed that the CuO nanoparticle-modified electrode had a good linear range and a sensitivity of 1.43 mA cm^{-2} mM^{-1} in NaOH [171]. Ibupoto and coworker developed a glucose sensor using CuO nanosheets which were grown on a gold coated glass substrate. The proposed CuO nanosheets non-enzymatic sensor showed a sensitivity of 5.20×10^2 μA/mM cm^2 for glucose sensing [172]. Jiang and coworkers reported a CuO nanoparticles-modified MWNTs array electrode for sensitive nonenzymatic glucose detection. At an applied potential of +0.40 V, the CuO/MWNTs electrode presented a high sensitivity of 2596 μA mM^{-1} cm^{-2} to glucose [173].

The most accepted mechanism for the oxidation of glucose on the CuO modified electrode in an alkaline medium is as follows. During the electrochemical measurement, Cu (II) on the CuO

modified electrode was first oxidized to Cu (III). The produced oxidative Cu (III) catalyzed glucose to generate gluconolactone and then gluconolactone is further oxidized to glucose acid, as schematically shown in Fig. 1.22 [174].

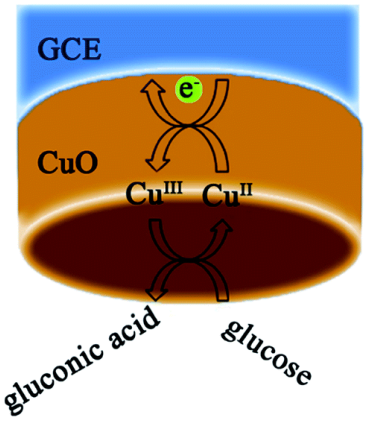

I) $CuO + OH^- \rightarrow CuOOH + e^-$

II) $CuOOH + e^- + glucose \rightarrow CuO + OH^- + gluconic\ acid$

Figure 1.22 Schematic of a reaction pathway during the non-enzymatic electro-oxidation of glucose on the surface of the CuO modified electrode in an alkaline medium. Adopted from Ref. [175].

On the other hand, TiO_2 nanotubes have been explored as promising nano sized electrode candidate for electrochemical biosensors. Besides large surface area, highly ordered one dimensional, one-end open tubular structure and good biocompatibility, TiO_2 nanotubes offer the following additional benefits: 1) Structure and morphology control of the tubes during the synthesis provides possibilities for the different designs of electrode; 2) Vertically aligned nanotube arrays facilitate more rapid electron transfer compared to randomly distributed nanotubes due to the directly transfer of electrons along the vertical direction of the tubes; 3) Strong adhesions between TiO_2 nanotubes and Ti substrate avoid the loss in electrochemical activity in the long term practical

operations; 4) The structure of TiO_2 nanotube/Ti forms an n-type semiconductor/metal Schotty-type contact, which would enhance the rapid transport of surface reaction electrons to the metal surface. Kafi and coworkers reported a promising H_2O_2 biosensor based on the co-immobilization of HRP and chitosan onto Au-modified TiO_2 nanotube arrays. In their work, the titania nanotube arrays were directly grown on a Ti substrate using anodic oxidation and then coated with a layer of gold film. The results in their work showed that the Au-modified TiO_2 nanotube arrays provide excellent sensing platform for the immobilization of HRP and the proposed electrochemical biosensor exhibited a low detection limit with high stability and very good reproducibility for the detection of H_2O_2 [176]. Similarly, Wang and coworkers presented a glucose biosensor based on GOx modified TiO_2 nanotubes. The enzyme was cross linked onto the nanotubes. A detection limit as low as 3.8 μM was achieved for the as-prepared glucose biosensors with good reproducibility and long-time storage stability [170]. The same authors proposed a TiO_2 nanotubes based non enzymatic electrochemical biosensors for sensing H_2O_2. In their protocols, reduced graphene oxide was modified onto the TiO_2 nanotubes for the deposition of silver nanoparticles. The results demonstrated that the proposed electrode responded to H_2O_2 with a sensitivity of 1152 μA mM^{-1} cm^{-2} at a working potential of −0.6 V [177]. Herein, in chapter 5, a non-enzymatic glucose based on CuO nanoparticle coated TiO_2 nanotubes is described in detail.

1.4.4 Gold nanoparticles in electrochemical sensing of *Clostridium difficile* toxins

Clostridium difficile (*C. difficile*) is a spore-forming, gram-positive and anaerobic bacterium. It is the major cause of antibiotic-associated diarrhea and almost all cases of pseudomembranous colitis [178]. During the *C. difficile* infection (CDI), two exotoxins with similar structure and function were released: toxin A (TcdA) and toxin B (TcdB). Both TcdA and TcdB are cytotoxic, pro-inflammatory, and enterotoxic in human intestine [179]. They are primarily responsible for

the diseases associated with the infection [180]. The incident of *C. difficile* infection is increasing dramatically during the past few years. There are at least 250,000 CDI cases per year and more than 14,000 deaths were reported due to CDI in US alone and the associated cost is about $1.1 to $3.2 billion every year [179, 181, 182]. Early diagnosis is essential for the better control and management of CDI, therefore, much research has been focus on the rapid diagnosis and treatment of CDI in hospital settings [183].

The diagnosis of *C. difficile-associated diarrhea* is mainly based on clinical features and detection of *C. difficile* organisms and toxins [184]. Methods currently in use for the organism identification include stool culture, the detection of glutamate degydrogenase (GDH), and polymer chain reaction (PCR) [185]. Stool culture for *C. difficile* is seldom performed clinically now due to its inconvenience and slow turnaround time. Another disadvantage is that this method cannot specifically distinguish toxigenic from non-toxigenic strains [182]. GHD test detects enzyme that is produced by *C. difficile* isolates, which is not specific for toxin producing *C. difficile* becasue GHD is produced by both toxigenic and non-toxigenic organisms [186]. PCR assay can rapidly and specifically detect present of *C. difficile* toxin gene, but it requires special equipment and is limited by high cost [182]. The *C. difficile* toxin A&B detection assay is to detect toxins produced by *C. difficile* bacteria in a stool sample. There are two main assays for the toxin detection: tissue culture assay for cytopathic effection induced by the toxins and enzyme-linked immunosorbent assay (ELISA) [187] for the toxins bind to their specific antibodies. The tissue culture assay is labor intensive and often requires 24-48 hours to give results [188]. ELISA is the most commonly used for detecting TcdA and TcdB. It is rapid, easy to perform, and widely available, however, it is not as sensitive as tissue culture cytotoxin assay [187]. Therefore, a rapid and simple test with

high sensitivity and specificity for detecting *C. difficile* toxins is still challenging but highly desirable.

As we mentioned in section 1.1.4, electrochemical immunosensors, based on a specific interaction between antibody and antigen, provide sensitive and selective detectable electrochemical signals. The basic unit of each antibody is an immunoglobulin (Ig) monomer, which is composed of two identical heavy (H) and two identical light (L) polypeptide chains bound by disulfide (sulfur- sulfur) bonds, forming a shape like the letter 'Y' (Fig. 1. 23). The heavy chain (blue) consists of one variable region (V_H) and several constant domains (C_H1, C_H2 and C_H3). While the light chain (red) has one variable domain (V_L) and one constant domain (C_L). The base of the "Y" is responsible for the interaction with cell surface receptors, which is called the F_C ("fragment cristalyzable") region. It is composed of two constant domains (C_H2 and C_H3) of the two heavy chains. The region on an antibody that can bind antigens is called the Fab ("fragment antigen-binding") region, which contains one constant and one variable domain from each heavy and light chain of the antibody. The variable domain (V_H, V_L) is the most important region for the antigen binding, which is referred to as the F_V region. More specifically, the antibody-antigen interaction is achieved through six complementarity determining regions (CDRs), which are part of the variable domain. The single-chain fragment of variation (scF_V) consists of the variable domains of the heavy and light chains that have been combined into a single polypeptide, recognizing one antigen molecule at a time. Compared to conventional antibodies, heavy chain antibodies are devoid of the entire light chains and the first constant domain (C_H1) in the heavy chains. They are often present in camelids. For these antibodies, the attachment of antigen is achieved through one single variable domain on the heavy chains, referred to as V_HH or nanobody. Such single domain antibody fragments have several advantages for biotechnological applications result from their single domain nature. Their

high solubility, affinity and stability as well as small size make them high valuable in many diagnostics, therapeutics and biotechnological applications [189-192].

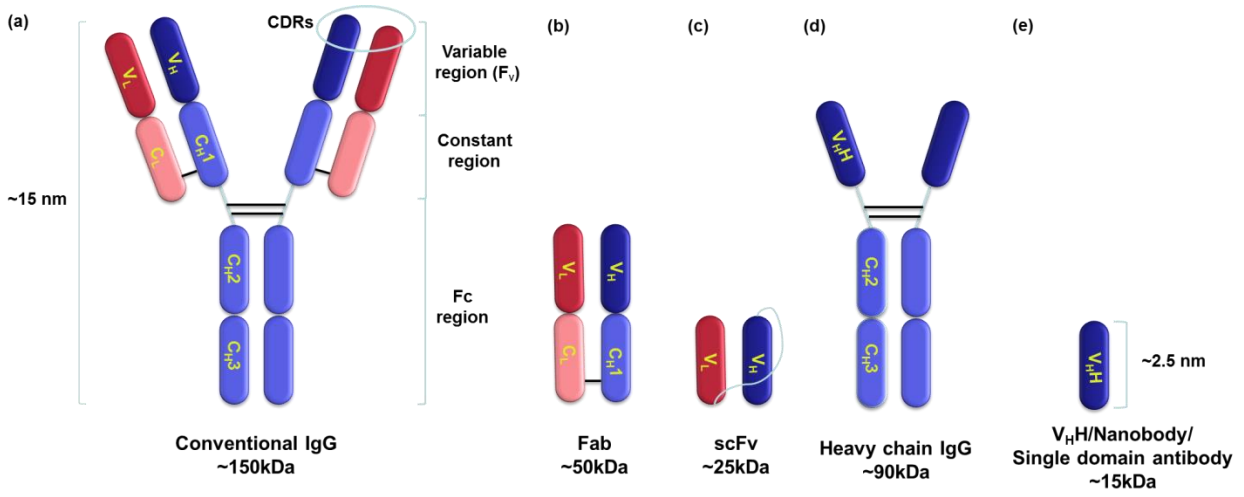

Figure 1.23 Structural features of different antibodies. (a) Conventioanl immunoglobulin G (IgG); (b) Fragment of antigen binding (Fab); (c) Single-chain fragment of variation (scFv); (d) Heavy chain IgG; (e) Nanobody/single-domain antibody (sdAb)/V_HH.

Similar to DNA biosensors, the antibody-antigen interactions often do not yield sensitive measurable signals. In general, electroactive indicators are required to provide or improve the electrochemical response in electrochemical immunosensor [27]. Another wildly used solution is to involve nanomaterials in the system to enlarge electrochemical signal. For nanomaterial based electrochemical immunosensors, the most common format is sandwich typed assay. In one case, the electrode is coated with nanomaterial first and then modified with capture antibodies. After the attachment of antigens, a secondary antibody conjugate labeled with electroactive tag is applied to provide or amply detection signal (Fig.1.24, left). In another case, capture antibodies are first coupled on the electrode, followed by the immobilization of antigens. The last step is to introduce

a secondary antibody conjugated co-labeled with nanomaterial and electroactive tag onto the electrode (Fig. 1.24, right). Nano sized particles are in the same range of dimension as nucleic acids, disease markers, proteins, and other biomolecules [193]. The field of biosensor has been interested in using nanoparticles as powerful tools for imaging and diagnosis in the past decade [194]. The synthesis of nanoparticles in bulk is much easier than that of other nanomaterials and can be achieved by a variety of methods [193]. Among different types of nanoparticles, gold nanoparticles (Au NPs) have been the most extensively used so far in electrochemical biosensors [195].

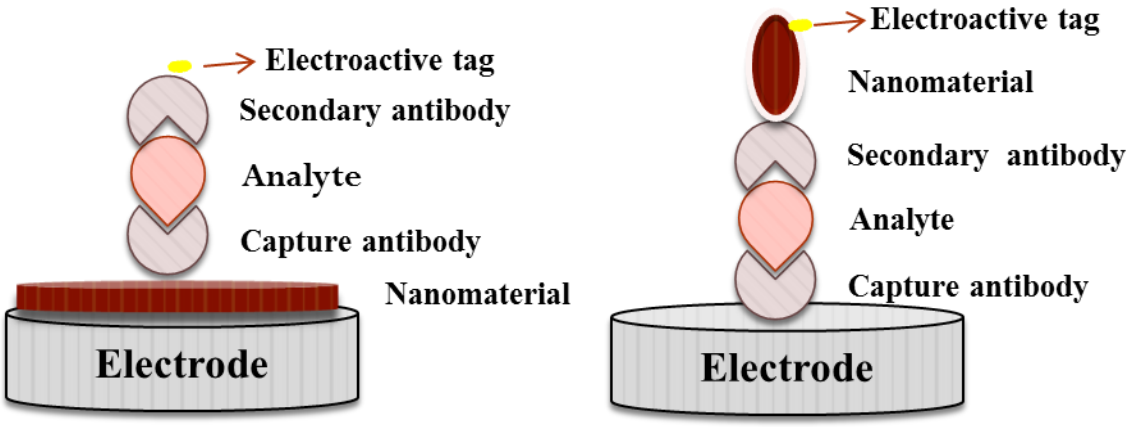

Figure 1.24 Sandwich-type electrochemical immunosensors.

Gold nanoparticles, which are practically non-toxic, have been used as a promising nanocarrier for therapy and diagnosis. Gold nanoparticles can be absorbed onto thiol-rich surfaces to form self-assembled nano-Au monolayers due to the strong interaction between -SH and Au. A wide range of biological ligands have been modified onto gold nanoparticle surface through the gold-thiolate bond [196]. Another critical property of gold nanoparticles is localized surface plasmon resonance (LSPR). At a specific wavelength of electromagnetic field, the delocalized electrons on the gold nanoparticle surface begin to oscillate collectively, resulting in a strong absorption band in the

visible region (Fig. 1.25). The absorption band is strongly dependent on the gold nanoparticle size, shape, surrounding microenvironment, and agglomeration state [195, 197]. The aggregation of gold nanoparticles often lead to a color change of nanoparticle solutions and a shift in LSPR peaks [198]. A series of colorimetric immunoassays based on shifting of the LSPR wavelength in response to gold nanoparticle aggregation caused by antibody-antigen interaction have been reported [37, 199]. In addition, gold nanoparticles have been served as fluorescence quenchers for fluorescence based sensing and one of the most popular substrates for surface enhanced raman scattering (SERS) biosensor in recent years [200, 201].

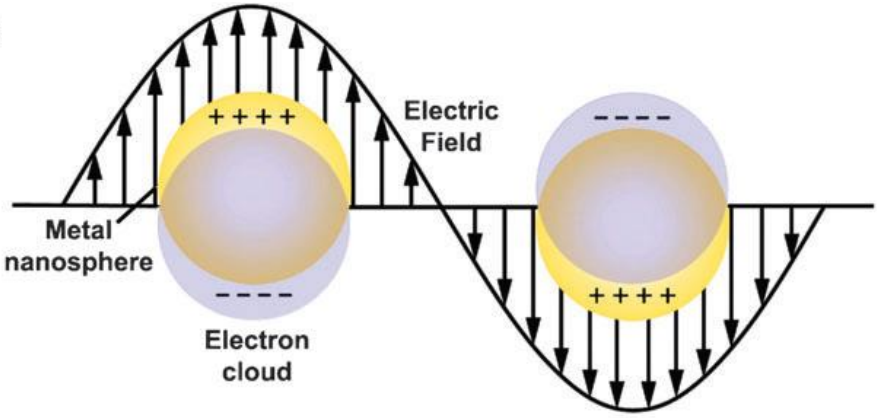

Figure 1.25 Basics of localized surface plasmon resonance (LSPR) of gold nanoparticles. Adopted from Ref. [197].

The ability of gold nanoparticles to serve as a platform for multi-functionalization of biomolecules retaining their bioactivity has motived researchers to explore potential applications in electrochemical biosensors. All these advantages combing with the characteristics of high surface to volume ratio and high surface energy provide new paths for developing novel electrochemical immunsensors based on gold nanoparticles with high sensitivity and excellent selectivity. The immobilization of antibody onto gold nanoparticles can be achieved through two mainly strategies:

the physical adsorption and the covalent binding [202]. It's well known that antibodies can be physically absorbed onto colloidal gold nanoparticle surface with retaining their biological activity [193]. The physical adsorption avoids the utilization of other chemicals and is a very popular method. This process can be achieved through hydrophobic interactions and ionic interactions. The hydrophobic interactions of antibody and colloidal gold nanoparticles happen between the hydrophobic part of antibodies and the surface layer on the colloidal gold nanoparticles [203]. The different charged surfaces of antibody and gold nanoparticle can form a conjugate through ionic interactions. For covalent binding, there are various strategies. Carboxyl groups can be active by N-Hydroxysuccinimide (NHS) and 1-Ethyl-3-(3-dimethylaminopropyl) carbodiimide (EDC) to form amine-carboxylate coupling between antibody and nanoparticle. The utilization of the direct attachment between thiolate molecule and gold surface is another important strategy [204].

Zhou and coworkers reported an immunosensor based on gold nanoparticles for the determination of hepatitis B surface (HBs) antigen. Au NPs were absorbed onto thionine modified gold electrode, following by the immobilization of antibodies. HRP, as the electrochemical active element, was then applied onto the electrode to block the nonspecific binding at the same time. The system was optimized to realize a reliable determination of HBsAg in the range of 2.56–563.2 ng/mL with a detection limit of 0.85 ng/mL [205]. Ahirwal and coworkers proposed a sandwich electrochemical immunosensor based on gold nanoparticles to detect human serum albumin. Glutathione capped Au NPs were covalently coupled with capture antibody (Ab_1) to form Au NPs/Ab_1 conjugates. The sandwich electrochemical immunoassay was produced with the immobilization of Au NPs/Ab_1 conjugates, antigens and secondary antibodies (Ab_2) labeled with HRP on a gold electrode. The detection limit of this electrode was 2 ng mL^{-1} of the analyte [206]. A similar gold nanoparticle based immunosensor for the detection of human cardiac troponin I (cTnI) by measuring open

circuit potential (OCP) was designed by Ahammad and coworkers. Au NPs were electrodeposited on indium tin oxide (ITO) electrode. Cystamine and glutaraldehyde were then intruded onto the electrode for the binding of capture antibody which against to cTnI. After the incubation with cTnI, HRP-conjugated anti-troponin antibody was attached onto the electrode. A linear dependence of OCP changes according to cTnI concentrations is observed in the range of concentration from 1 to 100 ng mL^{-1}[207]. Tang and coworker found that irregular-shaped gold nanoparticle performed better than spherical gold nanoparticles in electrochemical immunoassay for cancer biomarker α-fetoprotein (AFP) detection. In their protocol, carbon nanoparticles (CNPs)-functionalized biomimetic interface was used as the platform for immobilization of probe antibodies instead of using gold nanoparticles. The irregular-shaped gold nanoparticles-labeled HRP-anti-AFP conjugates (HRP-anti-AFP-ISNG), as trace label, were compared with spherical gold nanoparticles based conjugates. The results showed that the electrode using HRP-anti-AFP-ISNGs as trace labels exhibited high bioelectrocatalytic response toward enzyme substrate. The developed biosensor showed a low detection limit of 10 pg/mL [208].

Besides using electroactive molecular, electrochemical impedance spectroscopy also has been utilized to monitor antibody-antigen reaction for immunoassay application. As we mentioned in section 1.1.2, electrochemical impedance spectroscopy is very useful to monitor the bio-recognition event through capacitance, reactance and/or resistance changes at the modified electrode surface. Electrochemical impedance immunosensor based on gold nanoparticles have received considerable attention due to their advantages of label free and non-destructive. Wang and coworkers reported the use of Au NP based conjugation for impedance and capacitance signal amplification in biosensors for fluorescein detection. In this work, fluorescein was modified on a gold electrode with a self-assembled monolayer of 11-mercaptoundecanoic acid (11-MUA) in the

present of EDC/NHS. After the immobilization of goat anti-fluorescein coated with 10-nm Au nanoparticles, the capacitance and electrochemical impedance changed significantly [209]. Besides using Au NPs as secondary signal amplification element, another widely used strategy is to modify particles on the electrode first to form Au NP based platform for building sandwich assay. Rezaei and coworkers reported a human growth hormone (hGH) antibody/Au NP/1,6-hexanedithiol/gold electrode based immunosensor for the detection of hGH. Au NPs were coated on a gold electrode through the thiol groups of 1,6-hexanedithiol (HDT) monolayer. The positivity charged anti-hGH was immobilized electrostatically on the citrate capped Au NPs for capturing antigens. The limit of detection for hGH was about 0.64 pg mL^{-1} (Fig. 1.26) [210].

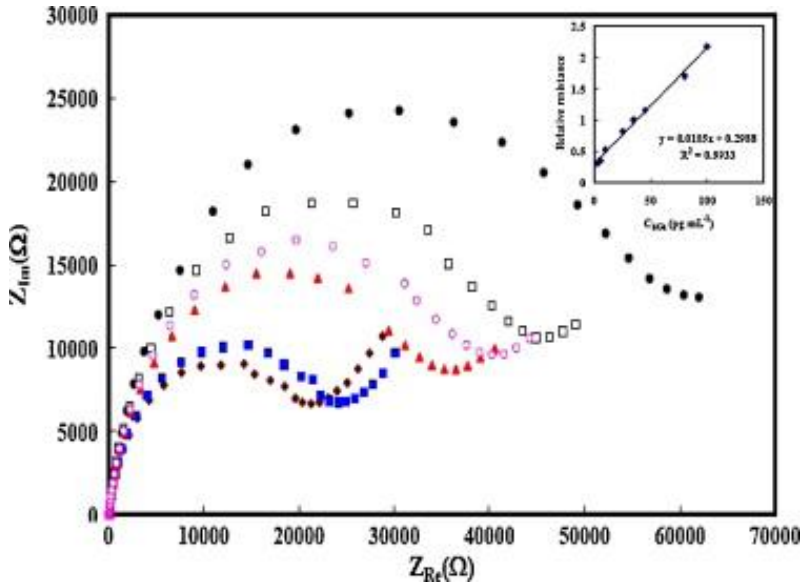

Figure 1.26 Nyquist diagrams of antibody/HDT/Au-colloid modified electrode (♦) and after treatment of: (■) 10 pg mL^{-1}; (▲) 17 pg mL^{-1}; (○) 35 pg mL^{-1}; (□) 80 pg mL^{-1}; (●) 100 pg mL^{-1} of hGH. Solution composition: 1 mM $K_3[Fe(CN)_6]/K_4[Fe(CN)_6]$, pH = 4.4containing of different concentrations of hGH. Voltage: 0.17 V, frequency range: 0.1 Hz to 100 kHz. Adopted from Ref. [210].

A similar immunosensor for detecting human IgG (hIgG) was reported by Chen and coworkers. In their work, Au NPs were self-assembled on a gold electrode through a layer of 1,6-hexanedithiol to absorb rabbit anti-hIgG antibodies. After the capture of target hIgG on the electrode, Au NPs labeled rabbit anti-goat IgG antibody and Au NPs labeled goat anti-hIgG antibody was applied on the electrode layer by layer. The impedance increments were observed to be linearly dependent upon the IgG concentration with a detection limit of 4.1 ng L^{-1} [211]. Gooding and coworkers reported an electrochemical impedance immunosensor based on gold nanoparticle for the detection of Hemoglobin A1c (HbA1c) in human blood. Au NPs were attached on the electrode through a layer of with 4-aminophenyl (Ph-NH_2). After the blocking of free amine groups with an oligo(ethylene glycol) (OEG-COOH) species, the Au NP surfaces were further modified with Ph-NH_2, followed by the attachment of an epitope N-glycosylated pentapep-tide (GPP). GPP, as an analogue of the HbA1c, can bind to anti-HbA1c IgG with high affinity. The interaction between the anti-HbA1c IgG and GPP caused an increase in charge transfer resistance. The amount of antigen was determined by a competitive inhibition assay where HbA1c was in analyte solution and GPP was on the electrode surface. HbA1c competed for the interaction with antibodies with GPP. The higher the concentration of HbA1c, the less uncomplexed antibody binds to the sensing interface and the lower the change of Rct. They found that the performance of the proposed immunosensor for detection of HbA1c in human blood was comparable to the clinical method [212].

Herein, the aim of chapter 6 is to combine the advantages of gold nanoparticles and electrochemical impedance immunosensor to develop a simple, fast, sensitivity, stable and label free nano-immunosensor to detect both TcdA and TcdB.

Reference

[1] A.J. Bard, L.R. Faulkner, 2nd, editor, Electrochemical Methods: Fundamentals and Applications, Wiley, 2001, p.

[2] R. Parsons, Chem. Rev. 90 (1990) 813-826.

[3] N.J. Ronkainen, H.B. Halsall, W.R. Heineman, Chem. Soc. Rev. 39 (2010) 1747-1763.

[4] F. Zhao, R.C. Slade, J.R. Varcoe, Chem. Soc. Rev. 38 (2009) 1926-1939.

[5] X. Dominguez-Benetton, S. Sevda, K. Vanbroekhoven, D. Pant, Chem. Soc. Rev. 41 (2012) 7228-7246.

[6] I.I. Suni, Trends Anal. Chem. 27 (2008) 604-611.

[7] Y. Wang, Z. Ye, Y. Ying, Sensors (Basel) 12 (2012) 3449-3471.

[8] C.F. Zinola, M.E. Martins, E.P. Tejera, N.P.N. Jr., Int. J. Electrochem. Sci. 2012 (2012) 1-2.

[9] N. Menzel, E. Ortel, R. Kraehnert, P. Strasser, Chem. Phys. Chem. 13 (2012) 1385-1394.

[10] R. Liu, J. Duay, S.B. Lee, Chem. Comm. 47 (2011) 1384-1404.

[11] M. Holzinger, A. Le Goff, S. Cosnier, Front. Chem. 2 (2014) 1-10.

[12] S.H. Lee, J.H. Sung, T.H. Park, Ann. Biomed. Eng. 40 (2012) 1384-1397.

[13] R.P. Singh, Int. J. Electrochem. Sci. 2011 (2011) 1-30.

[14] R.A.S. Luz, R.M. Iost, F.N. Crespilho, Nanobioelectrochemistry, F.N. Crespilho, editor, Nanomaterials for Biosensors and Implantable Biodevices, Springer-Verlag Berlin Heidelberg, 2013, p. 27-48.

[15] I.E. Tothill, World Mycotoxin J. 4 (2011) 361-374.

[16] S. Sagadevan, M. Periasamy, Rev. Adv. Mater. Sci. 36 (2014) 62-69.

[17] N. Gan, H. Jin, T. Li, L. Zheng, Int. J. Nanomedicine 6 (2011) 3259-3269.

[18] D. Grieshaber, R. MacKenzie, J. Voros, E. Reimhult, Sensors (Basel) 8 (2008) 1400-1458.

[19] K. Ariga, Q. Ji, T. Mori, M. Naito, Y. Yamauchi, H. Abe, J.P. Hill, Chem. Soc. Rev. 42 (2013) 6322-6345.

[20] J. Wang, Electroanalysis 17 (2005) 7-14.

[21] A. Ruhal, J.S. Ruhal, S. Kumar, A. Kumar, Cell. Mol. Biol. 58 (2012) 15-20.

[22] Y. Shao, J. Wang, H. Wu, J. Liu, I.A. Aksay, Y. Lin, Electroanalysis 22 (2010) 1027-1036.

[23] Z. Zhu, L. Garcia-Gancedo, A.J. Flewitt, H. Xie, F. Moussy, W.I. Milne, Sensors (Basel) 12 (2012) 5996-6022.

[24] J. Wang, Nucleic Acids Res. 28 (2000) 3011–3016.

[25] T.G. Drummond, M.G. Hill, J.K. Barton, Nat. Biotechnol. 21 (2003) 1192-1199.

[26] P. He, Y. Xu, Y. Fang, Microchim. Acta 152 (2005) 175-186.

[27] J.V. Veetil, K. Ye, Biotechnol. Prog. 23 (2007) 517-531.

[28] P. Bueno, C. Gabrielli, Nanostructured Materials for Electrochemical Energy Production and Storage, E. Leite, editor, Electrochemistry, Nanomaterials, and Nanostructures, Springer US, 2009, p. 3.

[29] E. Roduner, Chem. Soc. Rev. 35 (2006) 583-592.

[30] A.M. Smith, S. Nie, Acc. Chem. Res. 43 (2010) 190-200.

[31] X. Liu, M. Atwater, J. Wang, Q. Huo, Colloids Surf. B Biointerfaces 58 (2007) 3-7.

[32] M. Pumera, M.T. Castañeda, M.I. Pividori, R. Eritja, A. Merkoçi, S. Alegret, Langmuir 21 (2005) 9625-9629.

[33] H. Hou, X. Cao, Y. Yang, L. Fang, C. Pan, X. Yang, W. Song, et al., Chem. Comm. 50 (2014) 8201-8203.

[34] Z. Xu, Y. Hou, S. Sun, J. Am. Chem. Soc. 129 (2007) 8698-8699.

[35] F. Patolsky, Y. Weizmann, I. Willner, Angew. Chem. Int. Ed. Engl. 43 (2004) 2113-2117.

[36] K.I. Chen, B.R. Li, Y.T. Chen, Nano Today 6 (2011) 131-154.

[37] C. Wang, J. Irudayaraj, Small 4 (2008) 2204-2208.

[38] Z.M. Huang, Y.Z. Zhang, M. Kotaki, S. Ramakrishna, Compos. Sci.Technol. 63 (2003) 2223-2253.

[39] P. Roy, S. Berger, P. Schmuki, Angew. Chem. Int. Ed. Engl. 50 (2011) 2904-2939.

[40] L. Hu, G. Chen, Nano Lett. 7 (2007) 3249-3252.

[41] N. Sinha, J. Ma, J.T.W. Yeow, J. Nanosci. Nanotechnol. 6 (2006) 573-590.

[42] N. Jayaraju, D. Banga, C. Thambidurai, X. Liang, Y.-G. Kim, J.L. Stickney, Langmuir 30 (2014) 3254-3263.

[43] J.N. Coleman, M. Lotya, A. O'Neill, S.D. Bergin, P.J. King, U. Khan, K. Young, et al., Science 331 (2011) 568-571.

[44] Q. Zhang, N. Li, J. Goebl, Z. Lu, Y. Yin, J. Am. Chemi. Soc. 133 (2011) 18931-18939.

[45] S.C. Warren, L.C. Messina, L.S. Slaughter, M. Kamperman, Q. Zhou, S.M. Gruner, F.J. DiSalvo, et al., Science 320 (2008) 1748-1752.

[46] H. He, M. Zhong, D. Konkolewicz, K. Yacatto, T. Rappold, G. Sugar, N.E. David, et al., Adv. Funct. Mater. 23 (2013) 4720-4728.

[47] Z. Yan, R. Bao, D.B. Chrisey, Chem. Phys. Lett. 497 (2010) 205-207.

[48] J. Behari, Indian J. Exp. Biol. 48 (2010) 1008-1019.

[49] L.E. Euliss, J.A. DuPont, S. Gratton, J. DeSimone, Chem. Soc. Rev. 35 (2006) 1095-1104.

[50] A. Baron, D. Szewieczek, R. Nowosielski, AMME. 20 (2007) 83-86.

[51] P. Colson, C. Henrist, R. Cloots, J. Nanomater. 2013 (2013) 1-19.

[52] K. Byrappa, T. Adschiri, Prog. Cryst. Growth Charact. Mater. 53 (2007) 117-166.

[53] M. Yoshimura, K. Byrappa, J. Mater. Sci. 43 (2008) 2085-2103.

[54] S. Sana, K.C. Rajanna, K.R. Reddy, M. Bhooshan, M. Venkateswarlu, M.S. Kumar, K. Uppalaiah, Green and Sustainable Chemistry 02 (2012) 97-111.

[55] A. Tavakoli, M. Sohrabi, A. Kargari, Chem. Pap. 61 (2007) 151-170.

[56] H. Xu, B.W. Zeiger, K.S. Suslick, Chem. Soc. Rev. 42 (2013) 2555-2567.

[57] K. Wang, G. Liu, N. Hoivik, E. Johannessen, H. Jakobsen, Chem. Soc. Rev. 43 (2014) 1476-1500.

[58] C.R.K. Rao, D.C. Trivedi, Coord. Chem. Rev. 249 (2005) 613-631.

[59] C.A. Charitidis, P. Georgiou, M.A. Koklioti, A.F. Trompeta, V. Markakis, Manufacturing Rev. 1 (2014) 11.

[60] G. Injeti, B. Leo, Sci. Tech. Adv. Mater. 9 (2008) 043001.

[61] M.A. Malik, M.Y. Wani, M.A. Hashim, Arabian J. Chem. 5 (2012) 397-417.

[62] K.B. Narayanan, N. Sakthivel, Adv. Colloid Interface Sci. 156 (2010) 1-13.

[63] C.L. Haynes, R.P. Van Duyne, J. Phys. Chem. B 105 (2001) 5599-5611.

[64] L. Agui, P. Yanez-Sedeno, J.M. Pingarron, Anal. Chim. Acta. 622 (2008) 11-47.

[65] D. Eder, Chem. Rev. 110 (2010) 1348-1385.

[66] J.M. Schnorr, T.M. Swager, Chem. Mater. 23 (2011) 646-657.

[67] J. Li, Y. He, Y. Han, K. Liu, J. Wang, Q. Li, S. Fan, et al., Nano Lett. 12 (2012) 4095-4101.

[68] Y. Wu, X. Zhang, A.Y.T. Leung, W. Zhong, Thin Wall Struct. 44 (2006) 667-676.

[69] X. Lu, Z.F. Chen, Chem. Rev. 105 (2005) 3643-3696.

[70] W. Lin, C.P. Wong, Applications of Carbon Nanomaterials as Electrical Interconnects and Thermal Interface Materials, C.P. Wong, K.-S. Moon, Y. Li, editor, Nano-Bio-Electronic, Photonic and MEMS Packaging, Springer US, 2010, p. 87-138.

[71] J. Prasek, J. Drbohlavova, J. Chomoucka, J. Hubalek, O. Jasek, V. Adam, R. Kizek, J. Mater. Chem. 21 (2011) 15872-15884.

[72] S. Iijima, Nature 354 (1991) 56-58.

[73] L.L. Tian, X. Wang, L. Cao, M.J. Meziani, C.Y. Kong, F. Lu, Y. Sun, J. Nanomater. 2010 (2010) 742167.

[74] T. Guo, P. Nikolaev, A. Thess, D.T. Colbert, R.E. Smalley, Chem. Phys. Lett. 243 (1995) 49-54.

[75] M. Terrones, Annu. Rev. Mater. Res. 33 (2003) 419-501.

[76] M. Kumar, Y. Ando, J. Nanosci. Nanotechnol. 10 (2010) 3739-3758.

[77] G. Che, B.B. Lakshmi, C.R. Martin, E.R. Fisher, Chem. Mater. 10 (1998) 260-267.

[78] S.M. Toussi, A. Fakhru'l-Razi, C.A. Luqman, A.R. Suraya, IOP Conf. Ser.: Mater. Sci. Eng. 17 (2011) 012003.

[79] J.F. Colomer, C. Stephan, S. Lefrant, G.V. Tendeloo, I. Willems, Z. Konya, A. Fonseca, et al., Chem. Phys. Lett. 317 (2000) 83-89.

[80] Y. Homma, Y. Kobayashi, T. Ogino, J. Phys. Chem. B 107 (2003) 12161-12164.

[81] J.P. Tessonnier, D.S. Su, Chem. Sus. Chem. 4 (2011) 824-847.

[82] S.B. Sinnott, R. Andrews, D. Qian, A.M. Rao, Z. Mao, E.C. Dickey, F. Derbyshire, Chem. Phys. Lett. 315 (1999) 25-30.

[83] C. Ducati, J. Appl. Phys. 95 (2004) 6387-6391.

[84] A. Magrez, J.W. Seo, R. Smajda, M. Mionić, L. Forró, Materials 3 (2010) 4871-4891.

[85] M. Aksak, S. Kir, Y. Selamet, J. Optoelectron. Adv. Mater. Symposia 1 (2009) 281-284.

[86] A. Moisala, A.G. Nasibulin, E.I. Kauppinen, J. Phys.: Condens. Matter 15 (2003) S3011-S3035.

[87] C.L. Cheung, A. Kurtz, H. Park, C.M. Lieber, J. Phys. Chem. B 106 (2002) 2429-2433.

[88] Y. Li, R. Cui, L. Ding, Y. Liu, W. Zhou, Y. Zhang, Z. Jin, et al., Adv. Mater. 22 (2010) 1508-1515.

[89] N.R. Franklin, H. Dai, Adv. Mater. 12 (2000) 890-894.

[90] L. Qingwen, Y. Hao, C. Yan, Z. Jin, L. Zhongfan, J. Mater. Chem. 12 (2002) 1179-1183.

[91] J. Liu, S. Fan, H. Dai, MRS Bull. 29 (2004) 244-250.

[92] W.W. Liu, A. Aziz, S.P. Chai, A.R. Mohamed, C.T. Tye, Physica E Low Dimens. Syst. Nanostruct. 43 (2011) 1535-1542.

[93] T.S. Miller, N. Ebejer, A.G. Guell, J.V. Macpherson, P.R. Unwin, Chem. Commun. 48 (2012) 7435-7437.

[94] C.E. Banks, R.R. Moore, T.J. Davies, R.G. Compton, Chem. Commun. (2004) 1804-1805.

[95] R.R. Moore, C.E. Banks, R.G. Compton, Anal. Chem. 76 (2004) 2677-2682.

[96] C.E. Banks, T.J. Davies, G.G. Wildgoose, R.G. Compton, Chem. Commun. (2005) 829-841.

[97] C.E. Banks, A. Crossley, C. Salter, S.J. Wilkins, R.G. Compton, Angew. Chem. Int. Ed. Engl. 45 (2006) 2533-2537.

[98] K. Gong, S. Chakrabarti, L. Dai, Angew. Chem. Int. Ed. Engl. 47 (2008) 5446-5450.

[99] I. Heller, J. Kong, H.A. Heering, K.A. Williams, S.G. Lemay, C. Dekker, Nano Lett. 5 (2005) 137-142.

[100] A.F. Holloway, K. Toghill, G.G. Wildgoose, R.G. Compton, M.A.H. Ward, G. Tobias, S.A. Llewellyn, et al., J. Phys. Chem. C 112 (2008) 10389-10397.

[101] J. Liu, A. Chou, W. Rahmat, M.N. Paddon-Row, J.J. Gooding, Electroanalysis 17 (2005) 38-46.

[102] M. Pumera, Chemistry 15 (2009) 4970-4978.

[103] J.C. Charlier, Acc. Chem. Res. 35 (2002) 1063-1069.

[104] K. Suenaga, H. Wakabayashi, M. Koshino, Y. Sato, K. Urita, S. Iijima, Nat. Nanotechnol. 2 (2007) 358-360.

[105] P. Ayala, R. Arenal, M. Rümmeli, A. Rubio, T. Pichler, Carbon 48 (2010) 575-586.

[106] D. Fejes, K. Hernádi, Materials 3 (2010) 2618-2642.

[107] Y. Yin, Y. Chen, J. Yin, K. Huang, Nanotechnology 17 (2006) 4941-4945.

[108] Q. Lu, J.M. Moore, G. Huang, A.S. Mount, A.M. Rao, L.L. Larcom, P.C. Ke, Nano Lett. 4 (2004) 2473-2477.

[109] M. Zhang, J. Li, Mater. Today 12 (2009) 12-18.

[110] M. Terrones, A. Jorio, M. Endo, A.M. Rao, Y.A. Kim, T. Hayashi, H. Terrones, et al., Mater. Today 7 (2004) 30-45.

[111] A. Csató, A. Szabó, A. Fonseca, D. Vuono, Z. Kónya, A. Volodin, C. Van Haesendonck, et al., Catal. Today 181 (2012) 33-39.

[112] X. Tao, X. Zhang, J. Cheng, Y. Wang, F. Liu, Z. Luo, Chem. Phys. Lett. 409 (2005) 89-92.

[113] K. Chizari, I. Janowska, M. Houllé, I. Florea, O. Ersen, T. Romero, P. Bernhardt, et al., Appl. Catal. A: Gen. 380 (2010) 72-80.

[114] Y. Hao, L. Qingwen, Z. Jin, L. Zhongfan, Chem. Phys. Lett. 380 (2003) 347-351.

[115] S. Shanmugam, A. Gedanken, Electrochem. Comm. 8 (2006) 1099-1105.

[116] C.J. Lee, S.C. Lyu, H.-W. Kim, J.H. Lee, K.I. Cho, Chem. Phys. Lett. 359 (2002) 115-120.

[117] C.J. Lee, J. Park, Appl. Phys. Lett. 77 (2000) 3397-3399.

[118] C.H. Lin, H.L. Chang, C.M. Hsu, A.Y. Lo, C.T. Kuo, Diam. Relat. Mater. 12 (2003) 1851-1857.

[119] Y.Y. Wang, G.Y. Tang, F.A.M. Koeck, B. Brown, J.M. Garguilo, R.J. Nemanich, Diam. Relat. Mater. 13 (2004) 1287-1291.

[120] C.P. Ewels, M. Glerup, J. Nanosci. Nanotechnol. 5 (2005) 1345-1363.

[121] E. Raymundo-Piñero, D. Cazorla-Amorós, A. Linares-Solano, U.W. J Findb, R. Schlögl, Carbon 40 (2002) 597-608.

[122] L. Ma, A.H.C. Hart, S. Ozden, R. Vajtai, P.M. Ajayan, Farad. Discuss. 173 (2014) 9-46.

[123] Z. Chen, D. Higgins, Z. Chen, Carbon 48 (2010) 3057-3065.

[124] R. Lv, L. Zou, X. Gui, F. Kang, Y. Zhu, H. Zhu, J. Wei, et al., Chem. Commun. (2008) 2046-2048.

[125] J. Dong, X. Qu, L. Wang, C. Zhao, J. Xu, Electroanal. 20 (2008) 1981-1986.

[126] M. Landmann, E. Rauls, W.G. Schmidt, J. Phys.: Condens. Matter 24 (2012) 195503.

[127] S.D. Mo, W. Ching, Phys. Rev. B 51 (1995) 13023-13032.

[128] D. Regonini, A. Jaroenworaluck, R. Stevens, C.R. Bowen, Surf. Rev. Lett. Anal. 42 (2010) 139-144.

[129] K. Lee, A. Mazare, P. Schmuki, Chem. Rev. 114 (2014) 9385-9454.

[130] V. Galstyan, E. Comini, G. Faglia, G. Sberveglieri, Sensors (Basel) 13 (2013) 14813-14838.

[131] V. Zwilling, E. Darque-Ceretti, A. Boutry-Forveille, D. David, M.Y. Perrin, M. Aucouturier, Surf. Interface Anal. 27 (1999) 629-637.

[132] J. Tao, J. Zhao, C. Tang, Y. Kang, Y. Li, New. J. Chem. 32 (2008) 2164-2168.

[133] Y. Smith, R. Ray, K. Carlson, B. Sarma, M. Misra, Materials 6 (2013) 2892-2957.

[134] J.Y. Huang, K.Q. Zhang, Y.K. Lai, Int. J. Photoenergy 2013 (2013) 1-19.

[135] M.K. Debe, Nature 486 (2012) 43-51.

[136] E. Antolini, Appl. Catal. B: Environ. 88 (2009) 1-24.

[137] P.J. Kulesza, I.S. Pieta, I.A. Rutkowska, A. Wadas, D. Marks, K. Klak, L. Stobinski, et al., Electrochim. Acta 110 (2013) 474-483.

[138] N. Menzel, E. Ortel, R. Kraehnert, P. Strasser, Chemphyschem 13 (2012) 1385-1394.

[139] H. Song, X. Qiu, F. Li, Appl. Catal., A. 364 (2009) 1-7.

[140] D.J. Guo, J. Power Sources 196 (2011) 679-682.

[141] F. Kadirgan, S. Beyhan, T. Atilan, Int. J. Hydrogen Energy 34 (2009) 4312-4320.

[142] D.J. Guo, J. Power Sources 195 (2010) 7234-7237.

[143] K. Gong, F. Du, Z. Xia, M. Durstock, L. Dai, Science 323 (2009) 760-764.

[144] Y.M. Dai, T.C. Pan, W.J. Liu, J.M. Jehng, Appl. Catal. B: Environ. 103 (2011) 221-225.

[145] Z.Z. Zhu, Z. Wang, H.L. Li, Appl. Surf. Sci. 254 (2008) 2934-2940.

[146] Z.Z. Zhu, Z. Wang, H.L. Li, J. Power Sources 186 (2009) 339-343.

[147] P. Kang, S. Zhang, T.J. Meyer, M. Brookhart, Angew. Chem. 126 (2014) 8853-8857.

[148] J. Lin, C. He, Y. Zhao, S. Zhang, Sens. Actuator B-Chem. 137 (2009) 768-773.

[149] J. Narang, N. Chauhan, C.S. Pundir, Analyst 136 (2011) 4460-4466.

[150] X. Liu, C. Bu, Z. Nan, L. Zheng, Y. Qiu, X. Lu, Talanta 105 (2013) 63-68.

[151] Y. Shao, J. Sui, G. Yin, Y. Gao, Appl. Catal. B: Environ. 79 (2008) 89-99.

[152] L. Gan, R. Lv, H. Du, B. Li, F. Kang, Electrochem. Comm. 11 (2009) 355-358.

[153] L. Wang, L. Wang, H. Jin, N. Bing, Catal. Commun. 15 (2011) 78-81.

[154] S. Majeed, J. Zhao, L. Zhang, S. Anjum, Z. Liu, G. Xu, Nanotechnol. Rev. 2 (2013) 615-635.

[155] S. Ahammad, J. Biosens. Bioelectron. S9 (2013) 1-11.

[156] A.M. Azevedo, V.C. Martins, D.M.F. Prazeres, V. Vojinović, J.M.S. Cabral, L.P. Fonseca, Biotechnol. Annu. Rev. 9 (2003) 199-247.

[157] P. Pandey, M. Datta, B.D. Malhotra, Anal. Lett. 41 (2008) 159-209.

[158] W. Feng, P. Ji, Biotechnol. Adv. 29 (2011) 889-895.

[159] M. Zhang, A. Smith, W. Gorski, Anal. Chem. 76 (2004) 5045-5050.

[160] Y. Zhou, H. Yang, H.-Y. Chen, Talanta 76 (2008) 419-423.

[161] S. El Ichi, A. Zebda, A. Laaroussi, N. Reverdy-Bruas, D. Chaussy, M. Naceur Belgacem, P. Cinquin, et al., Chem. Comm. 50 (2014) 14535-14538.

[162] J. Wang, Chem. Rev. 108 (2008) 814-825.

[163] E.H. Yoo, S.Y. Lee, Sensors (Basel) 10 (2010) 4558-4576.

[164] L.C. Clark, Jr., C. Lyons, Ann. NY Acad. Sci. 102 (1962) 29-45.

[165] Y. Xiao, F. Patolsky, E. Katz, J.F. Hainfeld, I. Willner, Science 299 (2003) 1877-1781.

[166] Z. Zhu, L. Garcia-Gancedo, A.J. Flewitt, H. Xie, F. Moussy, W.I. Milne, Sensors 12 (2012) 5996-6022.

[167] P. Si, Y. Huang, T. Wang, J. Ma, RSC Adv. 3 (2013) 3487-3502.

[168] S. Hrapovic, Y. Liu, K.B. Male, J.H.T. Luong, Anal. Chem. 76 (2004) 1083-1088.

[169] I. Delfino, M. Portaccio, B.D. Ventura, D.G. Mita, M. Lepore, Mater. Sci. Eng. C Mater. Biol. Appl. 33 (2013) 304-310.

[170] W. Wang, Y. Xie, Y. Wang, H. Du, C. Xia, F. Tian, Microchimi. Acta 181 (2013) 381-387.

[171] F. Huang, Y. Zhong, J. Chen, S. Li, Y. Li, F. Wang, S. Feng, Anal. Methods 5 (2013) 3050-3055.

[172] Z. Ibupoto, K. Khun, V. Beni, X. Liu, M. Willander, Sensors 13 (2013) 7926-7938.

[173] L.C. Jiang, W.D. Zhang, Biosens. Bioelectron. 25 (2010) 1402-1407.

[174] S. Sun, X. Zhang, Y. Sun, S. Yang, X. Song, Z. Yang, Phys. Chem. Chem. Phys. 15 (2013) 10904-10913.

[175] X. Zhang, S. Sun, J. Lv, L. Tang, C. Kong, X. Song, Z. Yang, J. Mater. Chem. A 2 (2014) 10073-10080.

[176] A.K.M. Kafi, G. Wu, A. Chen, Biosens. Bioelectron. 24 (2008) 566-571.

[177] W. Wang, Y. Xie, C. Xia, H. Du, F. Tian, Microchim. Acta 181 (2014) 1325-1331.

[178] S. Khanna, D.S. Pardi, Mayo. Clin. Proc. 87 (2012) 1106-1117.

[179] G.P. Carter, J.I. Rood, D. Lyras, Gut. Microbes. 1 (2010) 58-64.

[180] D. Drudy, S. Fanning, L. Kyne, Int. J. Infect. Dis. 11 (2007) 5-10.

[181] M.J. LaMarche, J.A. Leeds, A. Amaral, J.T. Brewer, S.M. Bushell, G. Deng, J.M. Dewhurst, et al., J. Med. Chem. 55 (2012) 2376-2387.

[182] S.H. Cohen, D.N. Gerding, S. Johnson, C.P. Kelly, V.G. Loo, L.C. McDonald, J. Pepin, et al., Infect. Control Hosp. Epidemiol. 31 (2010) 431-455.

[183] A. Rodriguez-Palacios, S. Borgmann, T.R. Kline, J.T. LeJeune, Anim. Health Res. Rev. 14 (2013) 11-29.

[184] D. O'Connor, P. Hynes, M. Cormican, E. Collins, G. Corbett-Feeney, M. Cassidy, J. Clin. Microbiol. 39 (2001) 2846-2849.

[185] D.N. Gerding, S. Johnson, L.R. Peterson, M.E. Mulligan, J. Silva, Infect. Control Hosp. Epidemiol. 16 (1995) 459-477.

[186] C.M. Surawicz, L.J. Brandt, D.G. Binion, A.N. Ananthakrishnan, S.R. Curry, P.H. Gilligan, L.V. McFarland, et al., Am. J. Gastroenterol. 108 (2013) 478-498.

[187] T.D. Wilkins, D.M. Lyerly, J Clin. Microbiol. 41 (2003) 531-534.

[188] D.M. Musher, A. Manhas, P. Jain, F. Nuila, A. Waqar, N. Logan, B. Marino, et al., J. Clin. Microbiol. 45 (2007) 2737-2739.

[189] M.R. Kierny, T.D. Cunningham, B.K. Kay, Nano Rev. 3 (2012) 17240.

[190] S. Muyldermans, Annu. Rev. Biochem. 82 (2013) 775-797.

[191] A. Mujić-Delić, R.H. de Wit, F. Verkaar, M.J. Smit, Trends Pharmacol. Sci. 35 (2014) 247-255.

[192] M.M. Harmsen, H.J. De Haard, Appl. Microbiol. Biotechnol. 77 (2007) 13-22.

[193] N. Sanvicens, M.P. Marco, Trends Biotechnol. 26 (2008) 425-433.

[194] A. El-Ansary, L.M. Faddah, Nanotechnol. Sci. Appl. 3 (2010) 65-76.

[195] K. Saha, S.S. Agasti, C. Kim, X. Li, V.M. Rotello, Chem. Rev. 112 (2012) 2739-2779.

[196] W. Putzbach, N.J. Ronkainen, Sensors (Basel) 13 (2013) 4811-4840.

[197] C.M. Cobley, J. Chen, E.C. Cho, L.V. Wang, Y. Xia, Chem. Soc. Rev. 40 (2011) 44-56.

[198] D.A. Giljohann, D.S. Seferos, W.L. Daniel, M.D. Massich, P.C. Patel, C.A. Mirkin, Angew. Chem. Int. Ed. Engl. 49 (2010) 3280-3294.

[199] G. Zhou, Y. Liu, M. Luo, Q. Xu, X. Ji, Z. He, ACS Appl. Mater. Interfaces 4 (2012) 5010-5015.

[200] F. Luo, L. Zheng, S. Chen, Q. Cai, Z. Lin, B. Qiu, G. Chen, Chem. Commun. 48 (2012) 6387-6389.

[201] H.I. Peng, B.L. Miller, Analyst 136 (2011) 436-447.

[202] M.T. Castan˜eda, S. Alegret, A. MerkoÅi, Electroanalysis 19 (2007) 743-753.

[203] R.G. Rayavarapu, W. Petersen, C. Ungureanu, J.N. Post, T.G. van Leeuwen, S. Manohar, Int. J. Biomed. Imaging 2007 (2007) 29817.

[204] Y.C. Yeh, B. Creran, V.M. Rotello, Nanoscale 4 (2012) 1871-1880.

[205] Y. Zhuo, R. Yuan, Y. Chai, Y. Zhang, X.l. Li, Q. Zhu, N. Wang, Anal. Chim. Acta. 548 (2005) 205-210.

[206] G.K. Ahirwal, C.K. Mitra, Biosens. Bioelectron. 25 (2010) 2016-2020.

[207] A.J.S. Ahammad, Y.H. Choi, K. Koh, J.H. Kim, J.J. Lee, M. Lee, Int. J. Electrochem. Sci. 6 (2011) 1906-1916.

[208] J. Tang, B. Su, D. Tang, G. Chen, Biosens. Bioelectron. 25 (2010) 2657-2562.

[209] J. Wang, J.A. Profitt, M.J. Pugia, I.I. Suni, Anal. Chem. 78 (2006) 1769-1773.

[210] B. Rezaei, T. Khayamian, N. Majidi, H. Rahmani, Biosens. Bioelectron. 25 (2009) 395-399.

[211] H. Chen, J.H. Jiang, Y. Huang, T. Deng, J.S. Li, G.L. Shen, R.Q. Yu, Sens. Actuator B-Chem. 117 (2006) 211-218.

[212] G. Liu, S. Iyengar, J.J. Gooding, Electroanalysis 24 (2012) 1509-1516.

Chapter 2 Electrocatalytic activity of Pt nanoparticles on bamboo shaped carbon nanotubes for ethanol oxidation

Abstract

Recently, bamboo shaped carbon nanotubes (BCNTs) have received increased attention due to its bamboo shaped structure associated properties and its application in direct methanol/ethanol fuel cells. In this work, the potential to use BCNTs as support material for loading Pt nanoparticles to improve their performance towards ethanol oxidation was studied. The structure and nature of the resulting Pt-BCNTS composite were characterized by transmission electron microscopy (TEM) and energy dispersive spectroscopy (EDS) spectrum, it was found that Pt nanoparticles were homogeneously dispersed on the BCNTs surfaces with 23.5% by weight. Cyclic voltammogram (CV) indicated that the Pt-BCNTs catalysts displayed excellent electrocatalytic activity and long-term stability toward ethanol oxidation. The excellent performance may be attributed to the high dispersion of nanoscale Pt catalysts and the unique nature of BCNTs.

This work has been published in Electrochimica Acta 55 (2010) 8517-8520.

2.1 Introduction

Carbon nanotubes (CNTs) have attracted tremendous interests in the past decade due to their unparalleled physical, mechanical, and chemical properties [1-3]. In recent years, intensive research efforts have been conducted to explore their application as noble metal-catalyst supports to improve the efficiency of direct ethanol/methanol fuel cells [4-8]. Many metals and their alloys have been successfully deposited on the surface of CNTs [9-15]. However, synthesis of highly dispersed metal particles with small and uniform size still remains a formidable challenge since raw carbon nanotubes exhibit weak interaction with metal particles and tend to form bundles in aqueous solutions caused by their highly hydrophobic surfaces and strong intertube van der Waals interactions [16, 17]. Although many approaches have been developed to functionalize carbon nanotubes to achieve a high metal loading on CNT surface, most of them require strict reaction conditions together with highly complicated procedure. Doping of some foreign atoms was recently demonstrated to be a simpler and more effective way to control the structural and electronic properties of nanotubes [18-20]. Many articles show that the bamboo-shaped structures are formed as long as the reaction gases contain nitrogenous gas or the nitrogenous precursors are employed during preparation of CNTs [21-24]. The defective sites and active sites were introduced onto the surface of CNTs during their synthesis in order to obtain such nitrogen-doped bamboo shaped carbon nanotubes (BCNTs) [25]. BCNTs developed with this procedure were able to keep one-dimensional graphite nanostructure and were considered to possess higher chemical activity and stronger interaction with metal particles than conventional CNTs [26, 27].

Herein, we report successful synthesis of BCNTs through chemical vapor deposition (CVD) using an acetonitrile nitrogenous gas, and then deposited Pt nanoparticles onto the BCNTs surface by aqueous phase reduction. Neither rigorous reaction conditions nor complicated procedure were

needed in the whole process. The electrocatalytic activity of Pt-BCNTs for ethanol oxidation which has never been done before was also investigated in detail. It is found that Pt-BCNTs catalyst displayed a higher electrocatalytic activity than Pt-MWNTs catalyst. In addition, this technique is suitable for production beyond the laboratory-scale.

2.2 Experimental

2.2.1 Preparation of Pt-BCNTs composite material

Nitrogen-doped bamboo shaped carbon nanotubes (BCNTs) used in this work were synthesized via CVD by using acetylene (C_2H_2) and acetonitrile (CH_3CN) as the carbon and nitrogen source. Here, the catalyst of Fe/Mg with the weight ratio of 1/9 was put into a ceramic boat and set in the CVD reaction tube. The furnace was heated up to 800 °C. Then CH_3CN and C_2H_2 with the volume ratio of 7/1 were introduced into the tube for 15 mins. After the furnace was cooled to room temperature, the black products were collected, and then purified by HCl solution to remove the residual catalyst. The whole process was protected by N_2. The details are similar to those described in Ref [28]. For comparison, the undoped carbon nanotubes were prepared using C_2H_2 as carbon source while other conditions unchanged. BCNT-supported Pt catalysts were synthesized by using $NaBH_4$ as a reductive agent. As presented in Scheme 2.1, 5 mg of BCNTs was dispersed in 10 mL deionized water by ultrasonic vibration for 0.5 h. Then 0.5 mL of 0.0386 M H_2PtCl_6 was added to the BCNTs suspension with continuous stirring for 2 h. During this period, the charged $PtCl_6^{2-}$ was anchored on the surface of BCNTs. Next, 1.0 mL of 0.07 M $NaBH_4$ aqueous solution was slowly dropped into this mixture and vigorously stirred at room temperature for 12 h. The resultant product was purified by centrifugation, washed thoroughly with deionized water and then recovered from the sediment. Pt nanoparticles supported on undoped multi-walled carbon nanotubes (MWNTs) were also prepared under the same conditions.

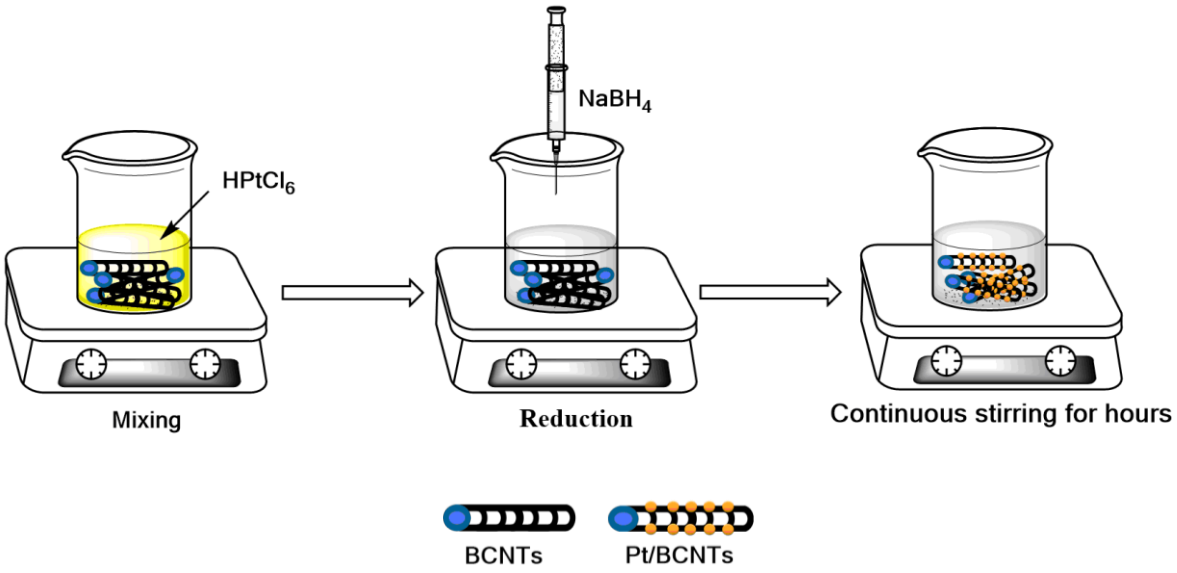

Scheme 2.1 Synthesis of Pt/BCNTs composite.

2.2.2 Preparation of Pt-BCNTs catalyst electrode

In order to investigate the electrochemical property by Cyclic voltammogram (CV), glassy carbon (GC) working electrodes, 3 mm in diameter, was polished with 1.0 and 0.3 μm alumina slurry sequentially and then washed ultrasonically in water and ethanol for a few minutes, respectively. 2 mg of Pt-BCNT catalyst sample, 0.25 mL of Nafion solution (0.1 wt %) and 0.5 mL of ethanol were mixed together using ultrasonic bath. A measured volume (10 μL) of this mixture was spread evenly by a micropipette onto the GC electrode surface twice, resulting in ~0.174 mg cm^{-2} Pt loading (assuming 100% reduction of Pt salt). The electrode was dried to evaporate the solvent. This modified electrode was called Pt-BCNTs electrode. The Pt-MWNTs electrode was also prepared in the same way with the Pt-MWNTs catalyst.

2.2.3 Measurements

Transmission electron microscopy (TEM, JEOL 100CX-II) operating at 100 kV was applied to characterize the morphology and particle size distribution. Energy dispersive spectroscopy (EDS) spectrum analysis was carried out on JSM-7000F (JEOL) scanning electron microscopy (SEM) to identify the presence of Pt and to compute the composition percentage of Pt-BCNTs. All electrochemical measurements were carried out using an Autolab PGSTA12 electrochemical workstation. A conventional cell with a three-electrode configuration was used throughout this work. The working electrode was modified glassy carbon electrode. Platinum wire and Ag/AgCl (saturated KCl) were used as the counter electrode and the reference electrode, respectively. All the electrolytes were deaerated by bubbling nitrogen (N_2) for 20 min before the experimental procedure. All the experiments were carried out at room temperature.

2.3 Results and discussion

2.3.1 TEM analysis

Fig. 2.1a presents a typical TEM image of the BCNTs, showing a very clean bamboo-shaped structure with diameter of 20-30 nm and wall thickness of 7-10 nm. The bamboo shape observed in nanotubes is characterized by segmented compartments, and the curvature of the compartment layers are all directed to the tube tip. The black dot on the bottom of the tube is the catalyst during the synthesis, which means that the growth of BCNTs is a base model. The roles of nitrogen in the formation of BCNTs are still under discussion. The diffusion of C and N through the catalyst particle to the growth site is the key point for understanding the growth mechanism of BCNTs. In the work reported by Jung and coworkers, they found that the nitrogen was incorporated mainly on the catalyst surface in NH_3 environment and affected the growth kinetics of CNT at catalyst surface. Enhancement of the BCNT growth due to the increase content of nitrogen was achieved.

They also proposed two possible roles of nitrogen in BCNT growth: 1) Enhance the formation of graphitic layer on the surface of catalyst; 2) Increase the separation of the graphitic layer from the catalyst surface. Their results showed that the major role of nitrogen in BCNT growth was different between the catalysts. In the case of Co catalyst, the major role of nitrogen is to enhance the formation of the graphitic layer. And the situation is different for Ni catalyst, both the two roles should be considered [29]. Lin and coworkers studied the role of nitrogen in CNTs growth with Fe, Co and Ni catalyst foils as substrates and CH_4/H_2 or CH_4/N_2 as source gases. The results indicated that the presence of nitrogen could prolong the passivation of catalyst surface and enhance carbon bulk diffusion in the catalyst surface [30]. Lee and coworkers proposed a detailed mechanism for the formation of compartment layer caused by nitrogen in BCNTs. According to their experiment, nitrogen was absorbed on the catalyst surface and restrained the surface diffusion of carbon. Thus, the wall growth controlled by carbon surface diffusion was reduced. However, the bulk diffusion of carbon increased due to the addition of nitrogen. As a result, the assumulation of carbon atoms at the inner surface of the catalyst enhanced, which was favorable for the formation of compartment layers in BCNTs [31]. On the other hand, the nitrogen containing pentagons can induce strong bending of the nanotubes, and greatly influenced the alignment of the CNT lattice [32]. The formation of bamboo shaped structure can be considered as the stacking of a series of graphitic conical. Therefore, the walls of BCNTs have a higher proportion of edge plans than that of hollow CNTs. Since the edge plans are highly defective, thus BCNTs have inherently higher defect density and can be expected to possess a better electrochemical property. Meanwhile, the incorporation of nitrogen into the hexagonal carbon lattice would disrupt the sp^2 hybridization of carbon atoms and favor the formation of pentagons and heptagons as well as increasing the reactivity of the tubes [33]. From Fig. 2.1b, it can be concluded that high loaded Pt nanoparticles

with a size of 3- 4 nm are well-dispersed on the BCNTs surface. We can also find that Pt nanoparticles distributed on BCNTs surface do not agglomerate even when they are present in high density. This is because defective and active sites are introduced on the carbon nanotube surface due to the N doping which tend to restrict the aggregation of nanoparticles. In contrary, the dispersion of Pt nanoparticles on MWNTs is unsatisfactory as shown in Fig.2.1c. The density of Pt nanoparticles on the MWNTs surface is low, and the degree of agglomeration is very high.

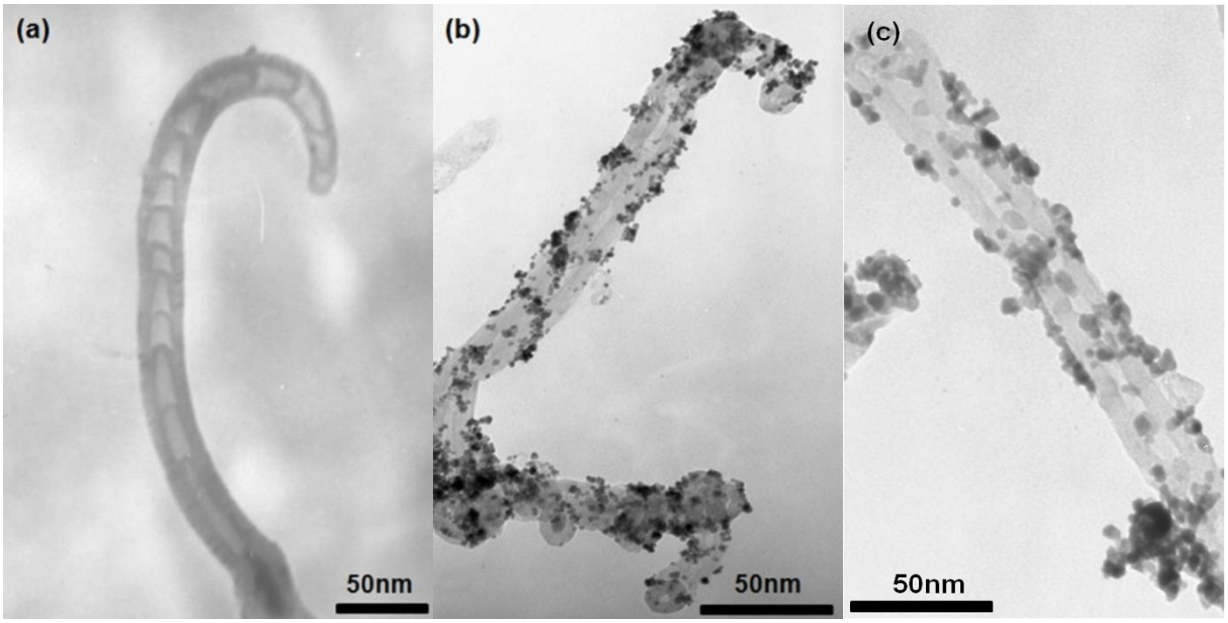

Figure 2.1 Transmission electron micrograph (TEM) images of (a) BCNTs, (b) Pt-BCNTs and (c) Pt-MWNTs composite materials.

2.3.2 EDS analysis

The EDS spectrum of the Pt-BCNTs composite materials is shown in Fig.2.2. The peaks of Pt and C originate from the carbon nanotube and Pt nanoparticles respectively. The Pt metal wt. % of the final composite is about 23.5 %. This value is a little bit higher than theoretical value (23 wt%, assuming 100% reduction of Pt salt), which is due to that EDS is a semi quantitative technique. Thus this value only can be used as a reference.

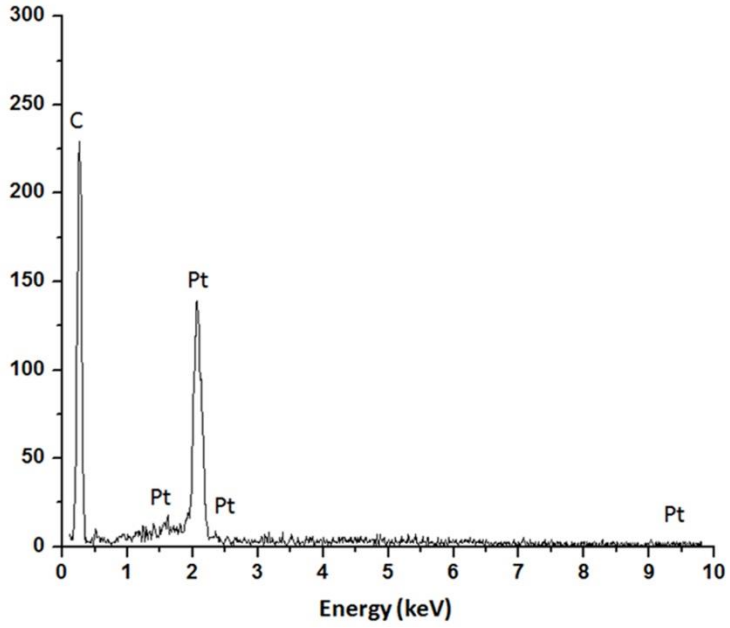

Figure 2.2 EDS spectra of Pt-BCNTs composite materials.

2.3.3 Electrochemical properties of Pt-BCNTs composite material

The electrochemical active surface area (ECSA) is one of the most important parameters to determine the catalytic properties of catalysts for ethanol oxidation, since this reaction is surface-sensitive. Generally, researchers use hydrogen adsorption curves to estimate the active specific surface area of Pt nanoparticles [34, 35]. ECSA can be calculated using the following equation: $ECSA = Q/q^0 \times M_{Pt}$. Here Q is the integrated area of the hydrogen desorption (μC) after the double layer correction, $q^0 = 210\ \mu C\ cm^{-2}$ is the charge of adsorption of a hydrogen monolayer on Pt [36], and M_{Pt} is the Pt loading on the electrode. Here, the CV curves of the GCE modified by the Pt-BCNTs and Pt-MWNTs catalyst in 0.5 M H_2SO_4 at a scan rate of 50 mV s^{-1} between -0.2 and +1.4 V are reported in Fig.2.3. The calculation results indicate that Pt/BCNTs have a higher ECSA around 58.7 $m^2\ g^{-1}$ than Pt-MWNTs (39.6 $m^2\ g^{-1}$), which means that Pt-BCNTs possess higher electrochemical active surface area. The high active surface area may be owed to the high

dispersion and small size of Pt nanoparticles on the BCNTs. It implied that BCNTs can promote the metal nanoparticles deposition and enhance the electrochemical active surface area of the electrocatalysts.

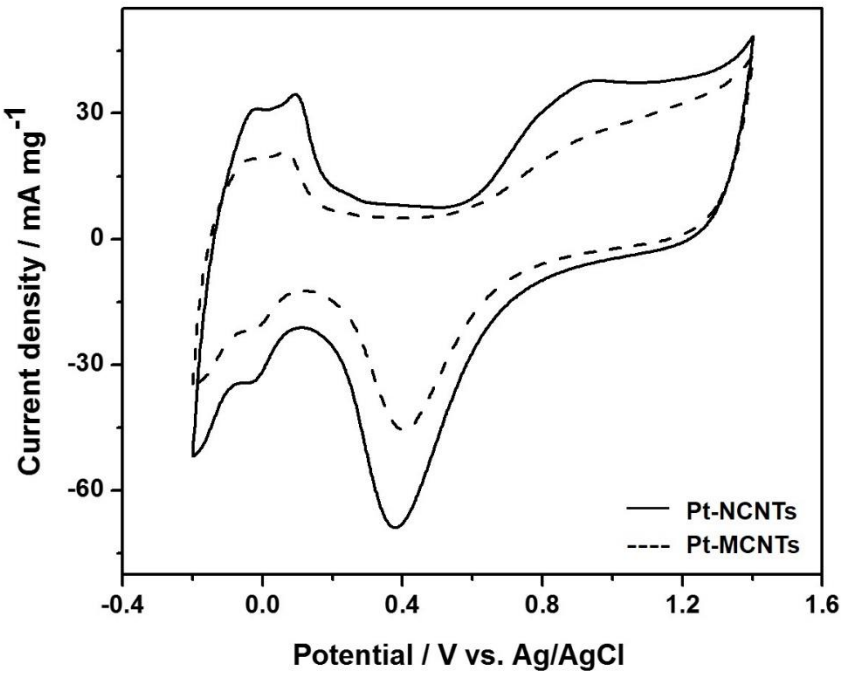

Figure 2.3 Cyclic voltammetry curves of Pt-MWNTs and Pt-BCNTs catalysts in 0.5 M H_2SO_4 solution. Scan rate: 50 mV s^{-1}.

The catalytic properties of Pt-BCNTs and Pt-MWNTs catalysts for the ethanol oxidation reaction have also been investigated by CV in 0.5 M H_2SO_4 + 0.5 M CH_3CH_2OH aqueous solutions (Fig. 2.4). CV was carried out in the potential window from -0.2 to +1.4 V at the rate of 50 mV s^{-1}. The current densities were normalized to the ECSA. The three typical CVs of ethanol oxidation can be observed at all the electrodes. In the forward sweep of solid curve, the first peak at about +0.72 V is mainly related to the formation of CO_2. The second peak at approximately +1.11 V corresponds

largely to the formation of CH_3CHO. In the backward sweep, another anodic peak is observed at around +0.43V owing to the removal of adsorbed intermediate generated during the oxidation of ethanol [37, 38]. It also can been seen that the current of Pt-BCNTs was greatly improved than the current of Pt-MWNTs. Compared to the dash curve which represents Pt-MWNTs, another visible difference found for solid curve which represents Pt-BCNTs was a lower peak potential. These results confirm that Pt-BCNTs catalysts have a better electrocatalytic activity than that of Pt-MWNTs for ethanol oxidation, which can be attributed to the high dispersion and the effective adhesion of Pt nanoparticles on BCNTs surface.

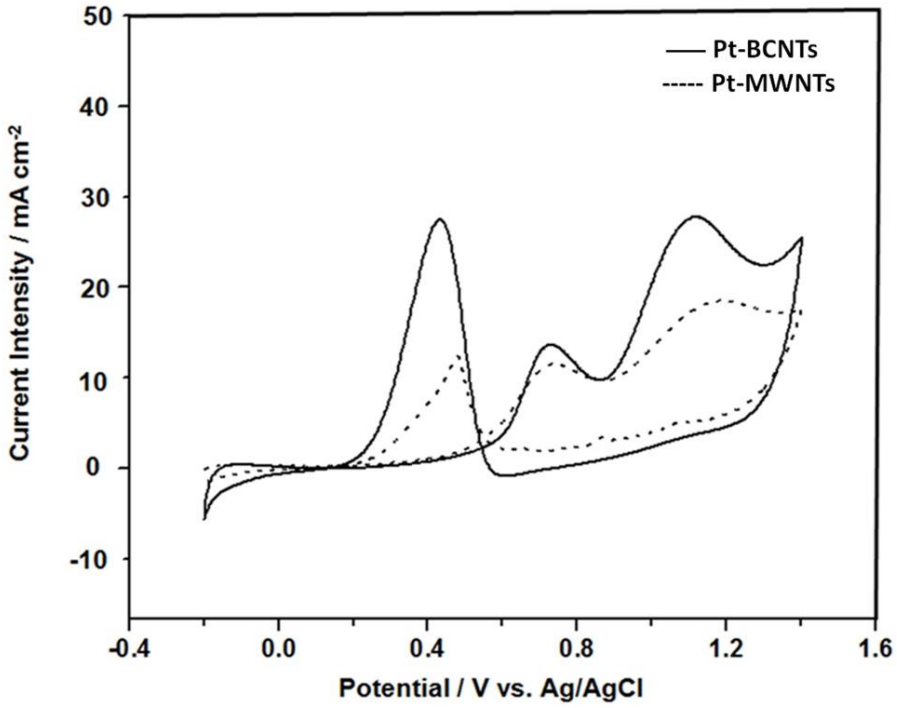

Figure 2.4 Cyclic voltammograms of Pt-MWNTs and Pt-BCNTs catalysts in 0.5 M H_2SO_4 + 0.5 M CH_3CH_2OH solution at a scan rate of 50 mVs^{-1}.

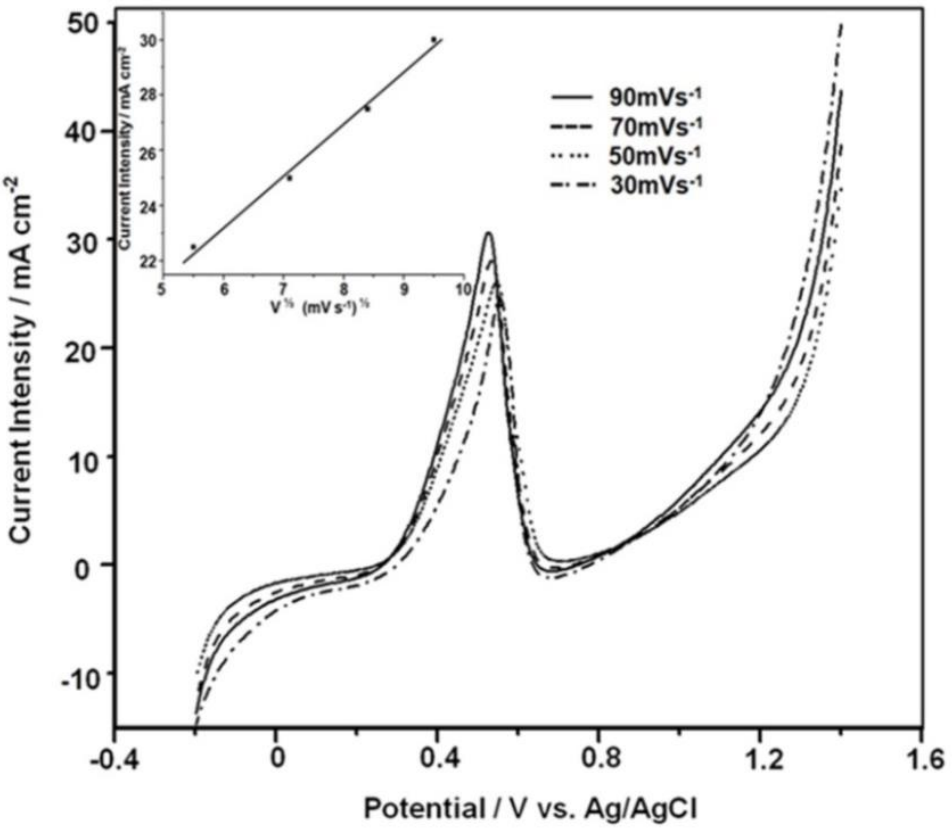

Figure 2.5 The linear sweep voltammograms of 0.5 M H_2SO_4 + 0.5 M CH_3CH_2OH solution at Pt-BCNTs catalyst at different scan rates. Insert: the plot of peak current density vs. square root of sweep rates.

We also characterized the peak currents at different scan rates. From Fig. 2.5, we can find that the peak current density for ethanol oxidation becomes higher with increasing scan rates. And also the peak current densities are linearly proportional to the square root of scan rate ($v^{½}$), as shown in the inset, suggesting that the electrocatalytic oxidation ethanol on Pt-BCNTs catalyst could be controlled by a diffusion process [39]. The above results demonstrate that doping of nitrogen atoms to carbon nanotube during the synthesis can greatly enhance the nucleation of nanocrystalline metals onto CNTs and promote the charge transfer from metals to the tubes by providing large numbers of defective sites and active sites on the surface. Also, Pt-BCNTs catalysts possessing highly active surface area will also supply more electrochemical reaction sites than Pt-MWNTs

composite materials. More importantly, it proves that doping foreign atoms to carbon nanotube is effective in the preparation of Pt-CNT anode electrocatalyst with high catalytic activity for ethanol oxidation.

Fig. 2.6 represents the chronoamperograms of Pt-BCNTs and Pt-MWNTs electrodes at 0.5 V in 0.5 M H_2SO_4 + 0.5 M CH_3CH_2OH aqueous solution. The decay of current follows the same trend for two catalysts and a more gradual decay with time was found for Pt-BCNTs catalyst. The sharp decrease at initial stage might be attributed to the double-layer charging and the formation of intermediate species such as COads on Pt NPs which can block the ethanol oxidation reaction to some degree. Meanwhile, Pt-BCNTs demonstrate a higher current density for a long time (1000s) compared with Pt-MWNTs, further reflecting their higher electrochemical activity.

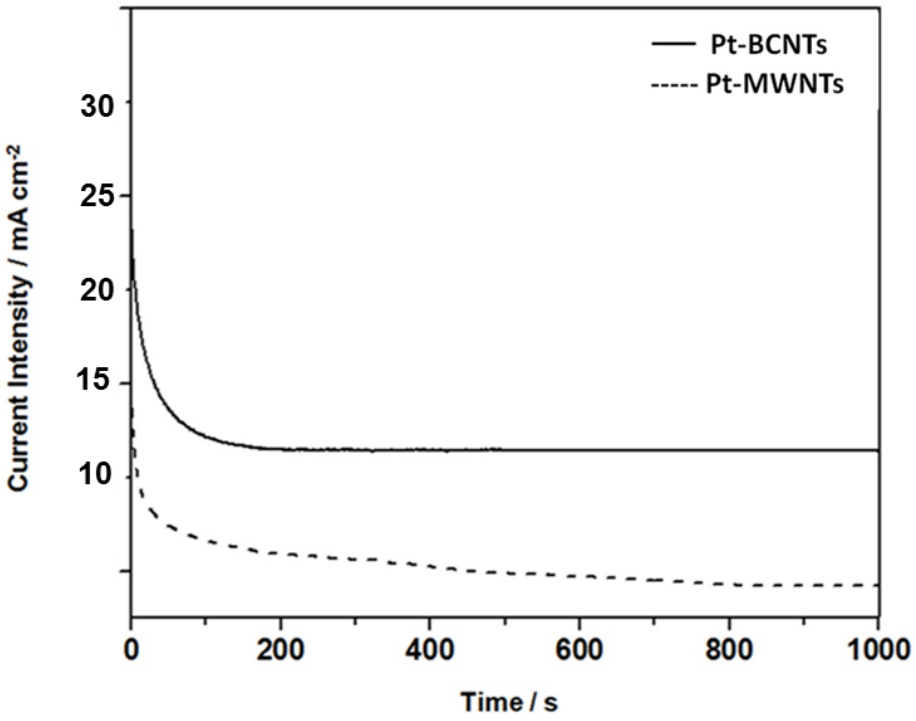

Figure 2.6 Chronoamperometry curves for Pt-MWNTs and Pt-BCNTs catalysts in 0.5 M H_2SO_4 + 0.5 M CH_3CH_2OH solution of 0.5 V.

2.4 Conclusions

In summary, highly dispersed Pt nanoparticles loaded on BCNTs were synthesized by a facile $NaBH_4$ assisted chemical reduction. The electrocatalytic properties of Pt on BCNTs have also been investigated. The Pt-BCNTs catalyst is found to display better electrocatalytic activity and stability for ethanol oxidation than Pt NP modified undoped carbon nanotube, which may be due to the defective sites and active sites caused by nitrogen doping on BCNT surface. These sites could allow a high loading of Pt nanoparticles and further promote the charge transfer on the electrode surface. The results demonstrate that Pt-BCNTs are an excellent candidate for electrolysis application and can be used to enhance its performance. Moreover, it provides vast array of new opportunities to use the special-structured carbon nanotubes for applications such as nanocomposite materials, biomedical engineering, nanoelectronics, energy storage, etc.

Acknowledgement

The authors greatly acknowledge the support from National Science Foundation (EEC-0823974).

References

[1] Z. Liu, S. Tabakman, K. Welsher, H.J. Dai, Nano Res. 2 (2009) 85-120.

[2] K.T. Lau, H.Y. Cheung, J. Lu, D. Hui, H.L. Li, J. Comput. Theor. Nanosci. 5 (2008) 23-35.

[3] J.H. Zhu, S.Y. Wei, J. Ryu, M. Budhathoki, G. Liang, Z.H. Guo, J. Mater. Chem. 20 (2010) 4937-4948.

[4] D. Wen, X.Q. Zou, Y. Liu, L. Shang, S.J. Dong, Talanta 79 (2009) 1233-1237.

[5] Z. Chen, D. Higgins, Z.W. Chen, Electrochim. Acta. 55 (2010) 4799-4804.

[6] C. J. Zhong, J. Luo, B. Fang, B. Wanjala, P. Njoki, R. Loukrakpam, J. Yin, Nanotechnology, 21 (2010) 062001(1-20).

[7] C.E. Banks, A. Crossley, C. Salter, S.J. Wilkins, R.G. Compton, Angew. Chem. Int. Ed. 45 (2006) 2533-2537.

[8] W.Z. Li, C.H. Liang, W.J. Zhou, J.S. Qiu, Z.H. Zhou, G.Q. Sun, Q. Xin, J. Phys. Chem. B 107 (2003) 6292-6299.

[9] N. Alexeyeva, J. Kozlova, V. Sammelselg, P. Ritslaid, H. Mandar, K. Tammeveski, Appl. Surf. Sci. 256 (2010) 3040-3046.

[10] H. J. Chen, S.J. Dong, Biosens. Bioelectron. 22 (2007) 1811-1815.

[11] B. Yue, Y.W. Ma, H.S. Tao, L.S. Yu, G.Q. Jian, X.Z. Wang, X.S. Wang, et al., J. Mater. Chem. 18 (2008) 1747-1750.

[12] Y.T. Kim, K. Ohshima, K. Higashumine, T. Uruga, M. Takata, H. Suematsu, T. Mitani, Angew. Chem. Int. Ed. 45 (2006) 407-411.

[13] H. Zhang, H. Cui, Langmuir 25 (2009) 2604-2612.

[14] S. Shanmugam, A. Gedanken**,** J. Phys. Chem. B 110 (2006) 2037-2044.

[15] J. Tashkhourian, M.R. Hormozi Nezhad , J. Khodavesi , S. Javadi, J. Electroanal. Chem. 633 (2009) 85-91.

[16] L. Gan, R. Lv, H.D. Du, B.H. Li , F.Y. Kang, Electrochem. Commun. 11 (2009) 355-358.

[17] L.F. Dong, Nanotechnology 20 (2009) 465602(1-5).

[18] Y.F. Tang, B.L. Allen, D.R. Kauffman, A. Star, J. Am. Chem. Soc. 131 (2009) 13200-13201.

[19] K.P. Gong, F. Du, Z.H. Xia, M. Durstock, L.M. Dai, Science 323 (2009) 760-764.

[20] J.P. Dong, X.M. Qu, L.J. Wang, C.J. Zhao, J.Q. Xu, Electroanalysis 20 (2008) 1981-1986.

[21] W.D. Zhang, Y. Wen, W.C. Tijiu, G.Q. Xu, L.M. Gan, Appl. Phys. A 74 (2002) 419-422.

[22] R.M. Yadav, P.S. Dobal, T. Shripathi, R.S. Katiyar, O.N. Srivastava, Nanoscale Res. Lett. 4

(2009) 197-203.

[23] Z.Y. Juang, J.F. Lai, C.H. Weng, J.H. Lee, H.J. Laic, T.S. Lai, C.H. Tsai, Diam. Relat. Mater. 13 (2004) 2140-2146.

[24] C.J. Lee, J. Park, J. Phys. Chem. B 105 (2001) 2365-2368.

[25] Q. H. Yang, P. X. Hou, M. Unno, S. Yamauchi, R. Saito, T. Kyotani, Nano Lett. 5 (2005) 2465-2469.

[26] Y. Okamoto, Chem. Phys. Lett. 420 (2006) 382-386.

[27] L. Gan, R. Lv, H.D. Du, B.H. Li , F.Y. Kang, Carbon 47 (2009) 1833-1840.

[28] C.N. He, N.Q. Zhao, C.S. Shi, X.W. Du, J.J. Li, J. Alloy. Compd. 433 (2007) 79-83.

[29] M. Jung, K.Y. Eun, Y.-J. Baik, K.-R. Lee, J.-K. Shin, S.-T. Kim, Thin Solid Films 398-399 (2001) 150-155.

[30] C.H. Lin, H.L. Chang, C.M. Hsu, A.Y. Lo, C.T. Kuo, Diam. Relat. Mater. 12 (2003) 1851-1857.

[31] C.J. Lee, S.C. Lyu, H.-W. Kim, J.H. Lee, K.I. Cho, Chem. Phys. Lett. 359 (2002) 115-120.

[32] R. Kurt, A. Karimi, Chem. Phys. Chem. 2 (2001) 388-392.

[33] S. Majeed, J. Zhao, L. Zhang, S. Anjum, Z. Liu, G. Xu, Nanotechnol. Rev. 2 (2013) 615-635.

[34] B.M. Babić, L.M. Vračar, V. Radmilović, N.V. Krstajić, Electrochim. Acta 51 (2006) 3820-3826.

[35] Z.C. Wang, D.D. Zhao, G.Y. Zhao, H.L. Li, J. Solid State Electrochem.13 (2009) 371-376.

[36] K. Honda, M. Yoshimura, T.N. Rao, D.A. Tryk, A. Fujishima, J. Electroanal. Chem. 514 (2001) 35-50.

[37] D.J. Guo, X.P. Qiu, L.Q. Chen, W.T. Zhu, Carbon 47 (2009) 1680-1685.

[38] F. Xiao, F. Q. Zhao, J.J. Zeng, B. Z. Zeng, Electrochem. Commun. 11 (2009) 1550-1553.

[39] K. Honda, M. Yoshimura, T.N. Rao, D.A. Tryk, A. Fujishima, K. Yasui, Y. Sakamoto, J. Electroanal. Chem. 514 (2001) 35-50.

Chapter 3 Bamboo shaped carbon nanotube supported platinum electrocatalyst synthesized by high power ultrasonic-assisted impregnation method for methanol electrooxidation and related density functional theory calculations*

Abstract

Carbon nanotubes (CNTs) with special forms may exhibit novel properties, which are different compared to conventional carbon nanotubes and may open a way for future applications. The nanotubes with a bamboo–like structure due to nitrogen doping have been well studied because of the increased attention for their bamboo shaped structure associated properties. In this work, bamboo shaped carbon nanotubes (BCNTs), synthesized by chemical vapor deposition (CVD) method, were investigated for direct methanol fuel cells (DMFC). Small sized platinum nanoparticles (Pt NPs) were dispersed onto BCNT surface through a high power ultrasonic assisted impregnation method in a short time. The structure and nature of the resulting Pt NP coated BCNT (Pt–BCNTS) composite were characterized by Transmission electron microscopy (TEM), X–ray diffraction (XRD), X–ray photoelectron spectroscopy (XPS) and energy dispersive spectroscopy (EDS). Density functional theory (DFT) calculations of Pt NPs coated on different structural CNTs showed that inclusion of nitrogen improved the catalytic performance of carbon nanotubes toward methanol electrooxidation. High electrochemical activity of BCNTs supported Pt NPs was demonstrated by the electrochemical studies.

This work has been published in International Journal of Hydrogen Energy 40 (2015) 2216-2224.

* The density functional theory calculation part in this work was cooperated with Brandon Bukowski and Prof. Deskins in Department of Chemcial Engineering in WPI.

3.1 Introduction

With the increasing environmental concerns and significant raise in the oil price, fuel cells have been investigated extensively in the scientific and engineering communities [1]. As one of the promising green energy sources, fuel cells are capable of offering high energy efficiency and delivering high energy density at low temperature [2]. The direct fuel cells based on the electrochemical oxidation of methanol have aroused wide research interests in recent years, as methanol is relatively low cost, easy to store and transport [3, 4]. The precious metal platinum (Pt) is widely used as the electrocatalyst for direct fuel cells, as Pt has several advantages such as high catalytic activity, chemical stability, high exchange current density, and a superior work function [3, 5–8]. In recent years, the use of carbon nanotubes (CNTs) as a support material to deposit Pt nanoparticles (Pt NPs) provides new ways to develop advanced electroelectrocatalyst materials [10].

Many reported methods for decorating CNTs with Pt NPs involve the functionalization of CNTs to create active sites for the reduction of metal ions because of the inertness of the CNT surface [11–13]. However, most of these approaches require strict reaction conditions together with highly complicated procedure [14, 15]. These disadvantages could be overcome by introducing defect sites in CNTs by changing their structure and further influence physical and chemical properties of carbon nanotubes [16, 17]. Many research groups have reported that doping nitrogen (N) into CNTs during their synthesis could yield bamboo–like nanotube structures, and thus introduce defect and active sites in CNTs [18–20]. Recently, the application of nitrogen doped bamboo shaped carbon nanotubes as a support for Pt NPs has shown promising results toward the electrochemical oxidation of small organic molecules [21–23].

A variety of methods have been successfully applied to prepare noble metal nanoparticles [24, 25].

Over the past few years, high power ultrasound, a cost–effective, easy to use and time saving technology, has been widely applied in the preparation of nanostructured materials to generate new products [26]. Herein, we report successful synthesis of bamboo shaped carbon nanotubes (BCNTs) with chemical vapor deposition (CVD) method, and then deposited Pt NPs onto BCNT surface by high power ultrasonic assisted impregnation method. The use of high power ultrasound for preparation of CNT–based metal nanoparticles was chosen because of the face that (i) Power ultrasound provide a uniform vibration environment for the growth of nanoparticles, resulting in better dispersion of nanoparticles on support material, (ii) Enhanced mass–transfer caused by the collapse of cavitation bubble, and (iii) Using power ultrasound can prevent the aggregation of CNTs and create nucleation sits on their surface for nanoparticles growth [27–29]. The electrocatalytic properties of as–prepared Pt NP coated BCNTs (Pt/BCNTs) were evaluated by typical electrochemical methods. Density functional theory (DFT) calculations were applied the first time to study the methanol decomposition reaction on BCNTs and BCNT based electrocatalysts.

3.2 Experimental

3.2.1 Preparation of Pt/BCNT composite material

BCNTs used in this work were synthesized via CVD by using acetylene (C_2H_2) and acetonitrile (CH_3CN) as the carbon and nitrogen source. The details are similar to those described in Ref [30, 31]. BCNT–supported Pt electrocatalysts were synthesized by using $NaBH_4$ as a reductive agent. As shown in Scheme 3.1, 5 mg of BCNTs were dispersed in 10 mL deionized water (DI water) by ultrasonication for 0.5 h. After the addition of 0.5 mL of 0.0386 M H_2PtCl_6 to the BCNT suspension with continuous stirring for 10 min, the mixture was placed into an ice bath. Then, a high–intensity ultrasonic probe (Ti–horn, 0.8cm diameter) was inserted into the center of the

mixture. 1.0 mL of 0.07 M $NaBH_4$ aqueous solution was slowly dropped into the mixture with applying a high power ultrasound (Ti–horn frequency: 40 kHz, max out power: 150 Watts) for 10 min. The resultant product was purified by centrifugation, washed thoroughly with DI water and then recovered from the sediment. Pt NPs supported on commercial multi–walled carbon nanotubes (MWNTs, Alfa, 20 nm diameters) (Pt/MWNTs) were also prepared under the same conditions.

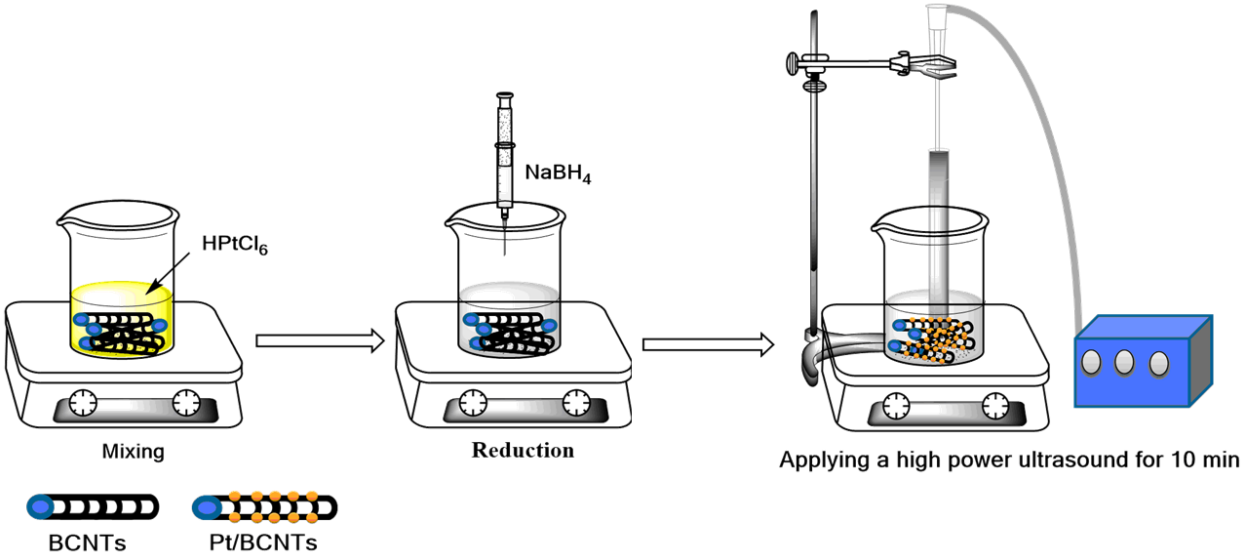

Scheme 3.1 Synthesis of Pt/BCNT composite with high power ultrasound.

3.2.2 Preparation of Pt/BCNT electrocatalyst coated electrode

Glassy carbon (GC) working electrodes, 3 mm in diameter, were polished with 1.0 and 0.3 µm alumina slurries sequentially and then washed ultrasonically with DI water and ethanol for a few minutes, respectively. 2 mg of Pt/BCNT electrocatalysts sample, 0.25 mL of Nafion solution (0.1 wt %) and 0.5 mL of ethanol were mixed together using an ultrasonic bath. A measured volume (10 µL) of this mixture was spread evenly by a micropipette onto the GC electrode surface twice, resulting in ~0.174 mg cm^{-2} Pt loading (assuming 100% reduction of Pt salt). The electrode was

then dried to evaporate the solvent. This modified electrode was labeled as Pt/BCNT electrode. Pt/MWNT coated electrode was prepared in the same way as the Pt/BCNT electrode.

3.2.3 Measurements

Transmission electron microscopy (TEM, JEOL 100CX–II) operating at 100 kV was applied to characterize the morphology and particle size. The presence of Pt was further identified by X–ray diffraction (XRD). X–ray photoelectron spectroscopy (XPS) data was obtained using a Physical Electronics Inc., 5000 Series Spectrophotometer with a mono-chromatic Al Kα x-ray at 37.5 W, a 200 μm spot area and a 45º angle of incidence. Energy dispersive spectroscopy (EDS) spectrum analysis was carried out on JSM–7000F (JEOL) scanning electron microscopy (SEM) to identify the presence of Pt and to compute the composition percentage of Pt–BCNTs. All electrochemical measurements were carried out using an Autolab PGSTA12 electrochemical workstation. A conventional cell with a three–electrode configuration was used throughout this work. The working electrode was modified glassy carbon electrode. Platinum wire and Ag/AgCl (saturated KCl) were used as the counter electrode and the reference electrode, respectively. All the electrolytes were deaerated by bubbling nitrogen gas (N_2) for 20 min before the experimental procedure. All the experiments were carried out at room temperature.

3.2.4 Modeling Details

Carbon nanotubes were modeled at the DFT level using the CP_2K code [32, 33]. A double–zeta basis set [34] for valence electrons and pseudopotentials [35, 36] for core electrons were used. The PBE exchange correlation [37] was also used. Periodic boundary conditions were applied with a simulation cell of dimensions 20 Å by 20 Å by 12.8 Å using a (6, 0) CNT. The CNT had 72 atoms with a diameter of 4.9 Å, giving a vacuum space of 15.1 Å between CNTs. K–point space was sampled by the Γ point.

3.3 Results and discussion

3.3.1 XRD analysis

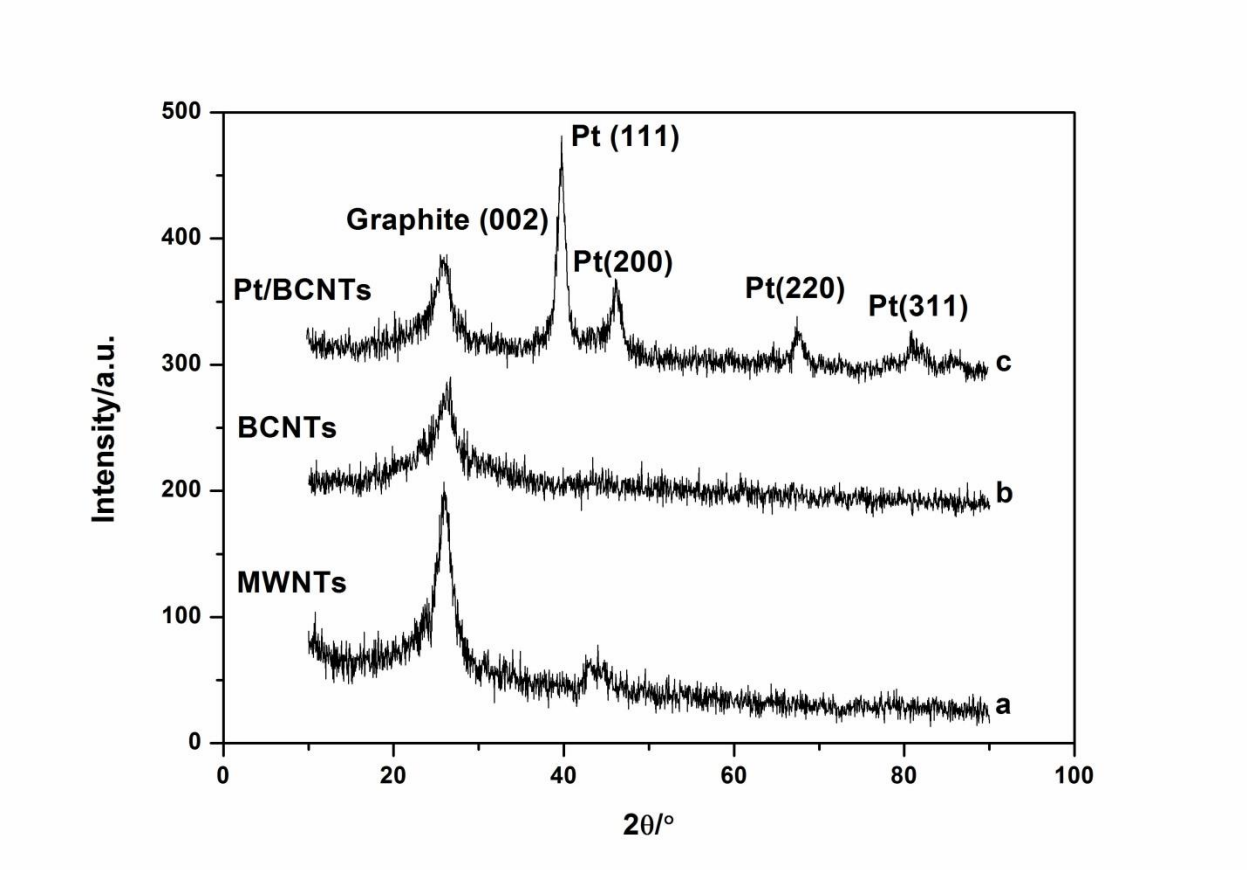

Figure 3.1 XRD patterns of (a) MWNTs, (b) BCNTs and (c) Pt/BCNTs.

Fig. 3.1 exhibits the XRD patterns of the MWNTs (a), BCNTs (b) and Pt/BCNT electrocatalysts (c). The diffraction peak located at a value of about 26° in the XRD patterns originates from (002) plane of graphitic structure of carbon nanotubes. The (002) peak of BCNTs is lower and broader than that of MWNTs due to a lower graphitization degree. The other four peaks found on curve c are characteristic of the face centered cubic (fcc) crystalline Pt (JCPDSICDD, Card No. 04–802), corresponding to the planes (111), (200), (220) and (311) at values of about 39°, 46°, 67° and 81°, respectively [38].

3.3.2 XPS analysis

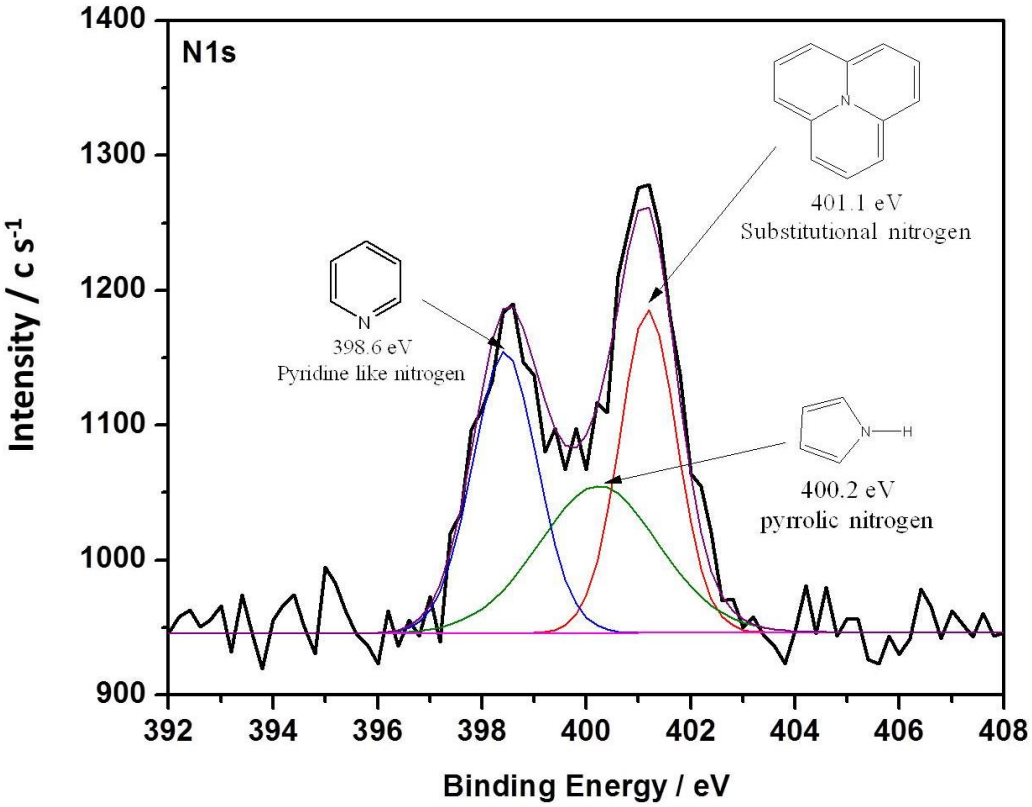

Figure 3.2 Deconvolution of the XPS spectra in the N 1s region for BCNTs.

XPS analysis was carried out to examine the present of nitrogen in the BCNT surface layer. The nitrogen atoms are inserted into the carbon atom matrix during the growth process and form a variety of nitrogen−carbon species in the final product BCNTs. The XPS surface atomic percentage of N on the surface of BCNT was measured to be 3.0%. The N1s line scan spectrum of BCNTs showing in Fig. 3.2 exhibits two obvious peaks and a weak peak between them. The first peak at 398.6 eV is usually assigned to pyridine–like nitrogen (pN) atoms while 401.1 eV is generally attributed to substitutional nitrogen (sN) atoms [39–41]. The weak peak at 400.2 eV is referred to pyrrolic nitrogen [39–41]. It can be observed that the ratio of the peak intensities is different where sN is the largest component, followed by pN.

3.3.3 TEM and EDS analysis

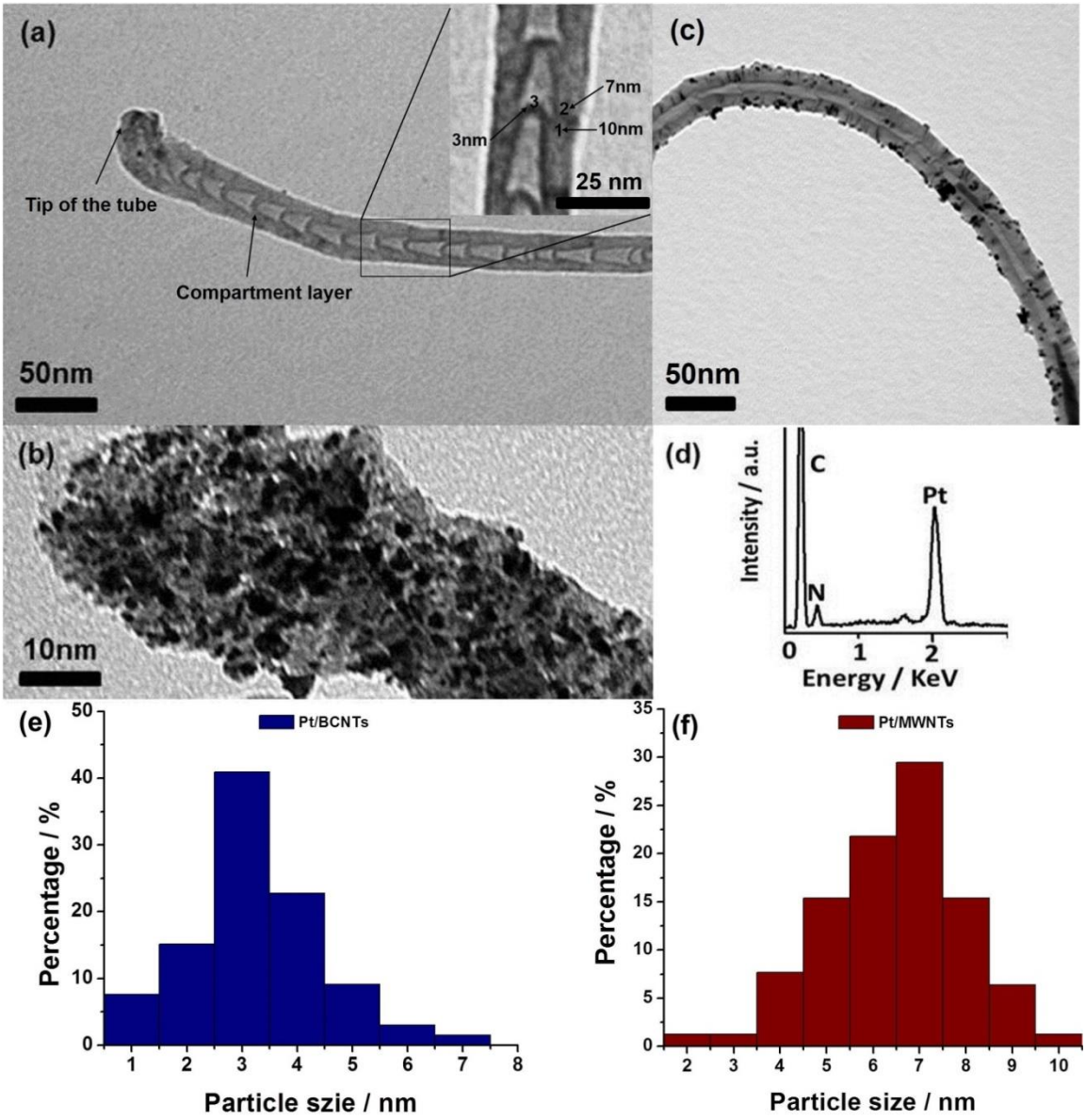

Figure 3.3 TEM images of (a) BCNTs, Insert: An enlargement of the rectangular area, (b) Pt/BCNTs, (c) Pt/MWNTs, (d) EDS spectra of Pt/BCNTs composite materials, the histograms of the distribution of Pt NPs on (e) BCNTs and (f) MWNTs.

A bamboo–shaped carbon nanotube with outer diameter of 25–30 nm is observed in Fig. 3.3a. The bamboo structure is characterized by segmented compartments, the curvatures of the graphitic

compartment layers are all directed to the tube tip. Meanwhile, there's no catalyst particles encapsulated in the closed tip. The insert of Fig. 3.3a shows an enlargement of the rectangular area. From the arrow marked position 1 to 2, the wall thickness changes from 10 nm to 7nm due to the formation of a graphitic compartment layer with the thickness of 3 nm (see arrow 3). Following the upward direction from position 2, the wall gradually increases again in thickness until it reaches the next compartment layer. Although the inner walls are away from the axis of the tube at a certain angle, the outer diameter keeps the same. The morphology of the synthesized BCNTs can be considered as the stacking of a series of graphitic conical. Therefore, the walls of BCNTs have a higher proportion of edge plans than that of hollow CNTs. Since the edge plans are highly defective, the synthesized BCNTs have inherently higher defect density and can be expected to possess a better electrochemical property [42–44]. On the other hand, the incorporation of nitrogen in to the hexagonal carbon lattice would disrupt the sp^2 hybridization of carbon atoms and favor the formation of pentagons and heptagons as well as increasing the reactivity of the tubes [45, 46]. Therefore, it can be observed that Pt NPs were homogeneously dispersed on the surface of BCNTs with a particle size range of 2–4 nm (Fig. 3.3b). However, the dispersion of Pt NPs on MWNTs is unsatisfactory as shown in Fig. 3.3c. The histograms of the distribution of Pt NPs on BCNTs and MWNTs were presented in Fig. 3.3e and Fig. 3.3f, respectively. Besides the effect of bamboo structure and nitrogen doping, the use of high power ultrasound during the electrocatalyst synthesis facilitates the formation of small sized nanoparticles and increase the particle dispersion on the BCNT surface as well. Good metal–carbon interaction and high surface area are very important factors that could influence the performance of carbon nanotube supported electrocatalysts. Therefore, Pt/BCNT electrocatalysts prepared by the high power ultrasound–assisted technique can be expected to exhibit high performance in DMFCs. The EDS spectrum of Pt/BCNTs

composite materials can be found in Fig 3.3d, the peaks of C, N and Pt originate from the bamboo shaped carbon nanotube and Pt nanoparticles respectively. The Pt metal wt% of the final composite giving by EDS is around 24.84%. This value is a little bit higher than theoretical value (23 wt%, assuming 100% reduction of Pt salt), which is due to that EDS is a semi quantitative technique. Thus this value only can be used as a reference. The density functional theory calculations of Pt/CNT systems will be discussed below.

3.3.4 Modeling of CNTs

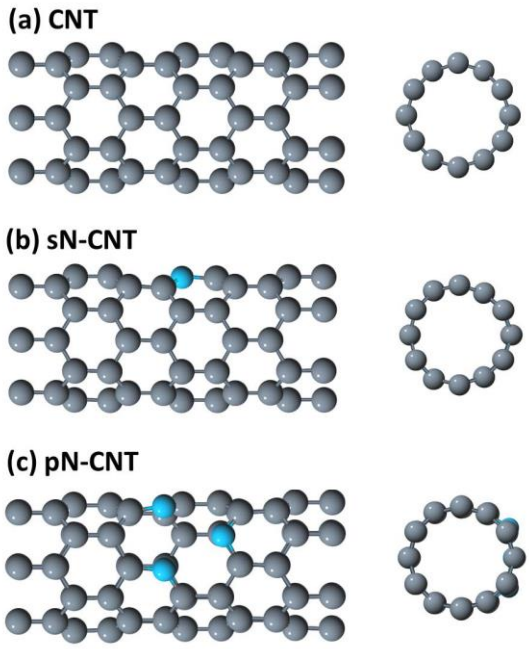

Figure 3.4 Models of (a) undoped, (b) substitutional nitrogen doped (sN–doped), and (c) pyridine liked nitrogen doped (pN–doped) CNTs. C and N atoms are represented by dark gray and blue spheres.

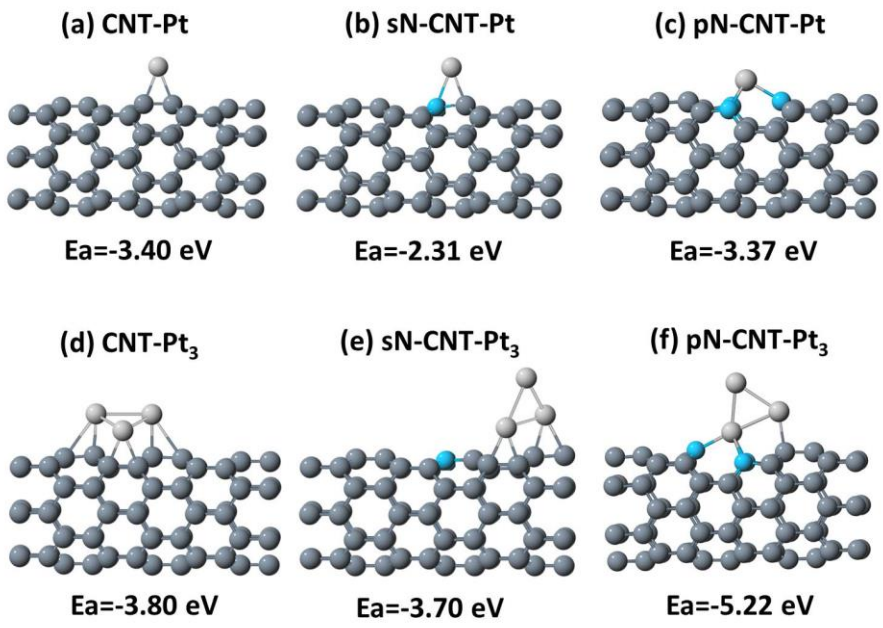

Figure 3.5 Models of (a) CNT with 1–Pt, (b) sN–doped CNT with 1–Pt, (c) pN–doped CNT with 1–Pt, (d) CNT with 3–Pt, and (e) sN–doped CNT with 3–Pt and (f) pN–doped CNT with 3–Pt. C , N and Pt atoms are represented by dark gray, blue and light gray spheres, respectively. Energies shown are adsorption energies for the Pt in eV.

Generally, there are three typical kinds of nitrogen found in nitrogen doped CNTs: pyridinic nitrogen, pyrrolic nitrogen and substitutional nitrogen [47, 48]. Previous work [49] indicates pyridine–like structures to be especially present in N–doped CNTs. According to the XPS results, two main types of nitrogen species, substitutional N and pyridinic N, will be discussed for our DFT modeling. Models of CNT, substitutional (sN–doped) and pyridine–like nitrogen doped (pN–doped) CNTs are presented in Fig. 3.4. These models are consistent with our own experimental results. Fig. 3.5 shows models of Pt atoms and Pt trimers over the different types of CNT. Such Pt atoms do not fully represent large Pt particles, but do provide insight on how Pt may behave on the CNTs. It can be seen that single Pt atom strongly bind both onto CNTs and nitrogen doped–CNTs. The Pt trimers however bind much stronger to pN–CNT than the other CNTs, which

indicates that pN–doped CNT may inhibit the diffusion and subsequent sintering of deposited Pt particles. Pt trimers do not appear to bind exactly over sN sites. Several adsorption configurations have been tried and the most stable one had the Pt trimer interacting with the carbon atoms, rather than the nitrogen atoms.

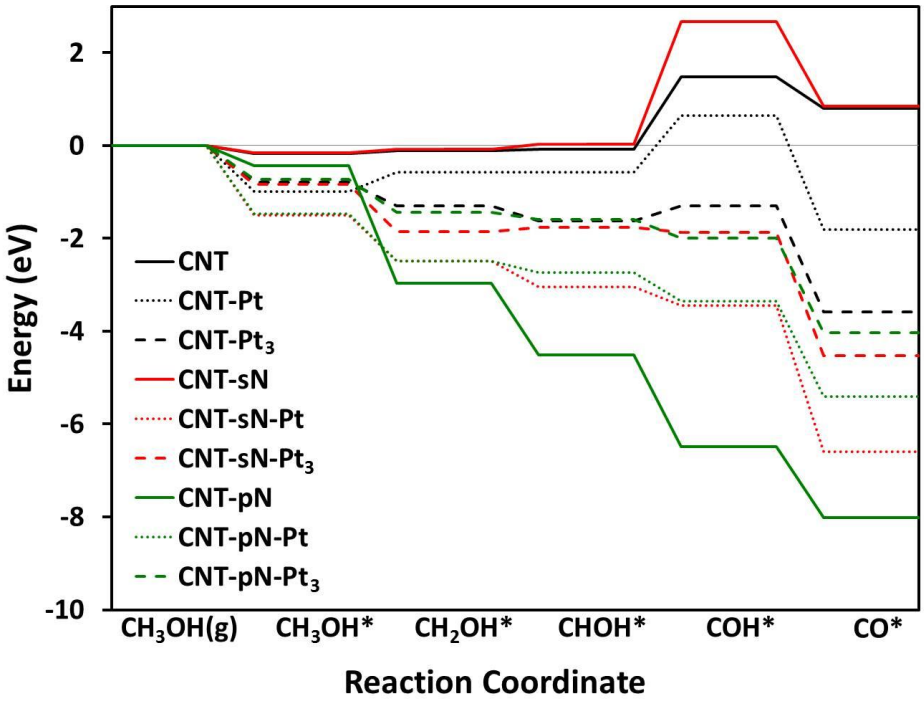

Figure 3.6 DFT results for methanol decomposition over different CNTs. The zero energy is taken as methanol in gas–phase. In each step an H atom is removed and adsorbed in its most stable configuration. E.g. $CH_3OH^* \rightarrow CH_2OH^* + H^*$.

The methanol decomposition reaction, a simplified representation of the full oxidation, was also modeled. Similar to previous studies, a dehydrogenation mechanism where H atoms were removed in step from the methanol molecule was studied [50, 51]. The adsorption of different possible intermediates (CH_3OH, CH_2OH, CHOH, COH, CO, H) on different CNTs was considered in order to calculate the reaction energies for the methanol decomposition reaction. Environmental

(aqueous phase) and electrochemical (electrical fields) effects were ignored for these simplified simulations of methanol interacting with the CNTs (see Supporting Information, Fig. S 3.4–3.12 for detailed images of all the modeled reaction steps). Fig. 3.6 shows results for the calculated pathway over various CNTs, which involved H extraction from the C atom until the last step, which removed H from the O atom. The reaction pathways in terms of energetic favorability follow the order of: pN-CNT > Pt-sN-CNT > Pt-pN-CNT > Pt_3-sN-CNT. Reaction energies are much more exothermic over the N–doped CNTs compared to pure CNTs for methanol decomposition. Overall, the DFT results indicate that the addition of nitrogen can efficiently improve the catalytic performance of carbon nanotubes toward methanol electrooxidation. Similar arguments have been made previously [52].

3.3.5 Electrochemistry studies

Fig. 3.7 compares the hydrogen electrosorption voltammograms of two electrodes in 1.0 M H_2SO_4 at a scan rate of 50 mV s^{-1} between −0.2 and 1.0 V. The peaks between −0.2 V and 0.15 V are attributed to the hydrogen adsorption/desorption on the Pt surface. The oxygen electrosorption and oxide formation potential range extends from 0.3 V to 1.0 V. The double layer region is between hydrogen and oxygen characteristic regions. The electrochemical surface area (ECSA) of Pt nanoparticles is a crucial parameter to determine the catalytic activity of an electrocatalyst for methanol oxidation, and it can be calculated using the following equation: $ECSA = Q/q^0 \times M_{Pt}$. Here Q is the integrated area of the hydrogen desorption (μC) after the double layer correction, q^0 = 210 μC cm^{-2} is the charge of adsorption of a hydrogen monolayer on Pt [53], and M_{Pt} is the Pt loading on the electrode. Calculation results indicate that Pt/BCNTs have a higher ECSA around 81.2 m^2 g^{-1} than Pt/MWNTs (63.4 m^2 g^{-1}). The result further indicates that BCNTs have the

potential to be a better support material than MWNTs for methanol electrooxidation on Pt nanoparticles.

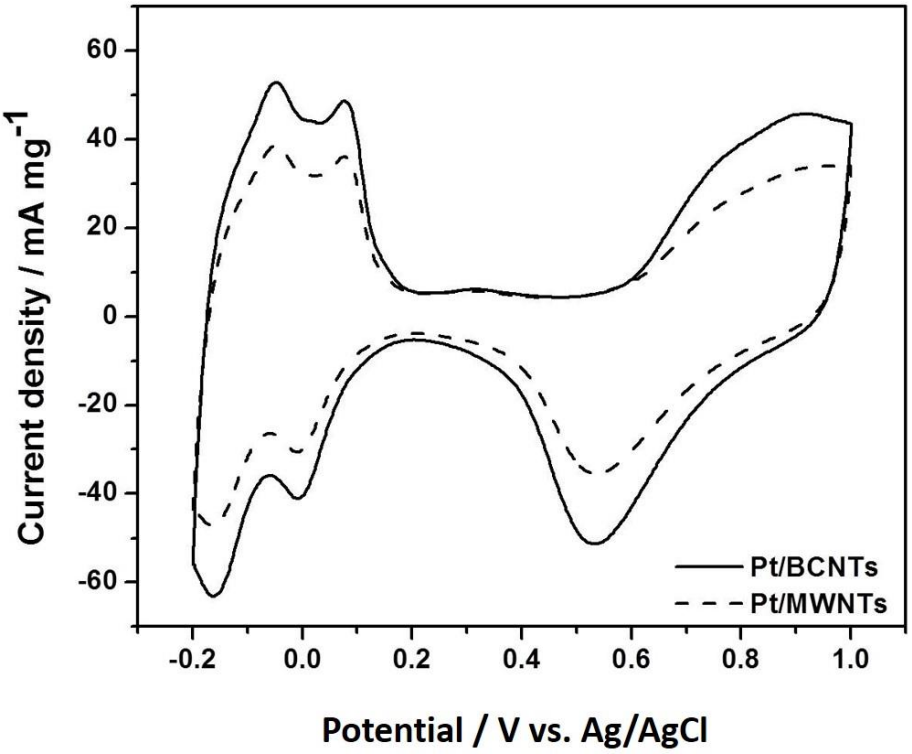

Figure 3.7 Cyclic voltammetry curves of Pt/ BCNTs (solid) and Pt/MWNTs (dash) in 1.0 M H_2SO_4 solution. Scan rate: 50 mV s^{-1}.

Fig. 3.8 illustrates the CV curves of methanol oxidation on Pt/BCNTs and Pt/MWNTs electrocatalysts in 1.0 M H_2SO_4 + 1.0 M CH_3OH solution. The current densities were normalized to the ECSA. Two irreversible current peaks for methanol oxidation can be observed at all the electrodes. The forward scan peak (peak 1) at around 0.75 V is attributed to the methanol electrooxidation and the back scan peak (peak 2) at about 0.48 V corresponds to the removal of the adsorbed carbonaceous species (COad) [54]. The current density of methanol oxidation on the

Pt/BCNT electrocatalysts in the forward scan is ~0.31 mA cm^{-2}_{Pt} and in the backward scan is ~0.22 mA cm^{-2}_{Pt}, much higher than those on the Pt/MWNTs electrocatalysts. The higher current density demonstrates that Pt/BCNTs have more electrocatalyst sites for methanol electrooxidation than Pt/MWNT, thus have better electrocatalytic activity. This may attributed to the highly dispersed Pt nanoparticles with small size on BCNTs surface. These results further confirmed that more electrocatalyst sites are accessible for methanol electrooxidation because of the formation of bamboo structure in the carbon nanotubes. Meanwhile, using ultrasound, Pt nanoparticles can be grown under a uniform environment and tend to be well dispersed on BCNTs [26]. The experimental results are consistent with the density function calculation (part 3.3).

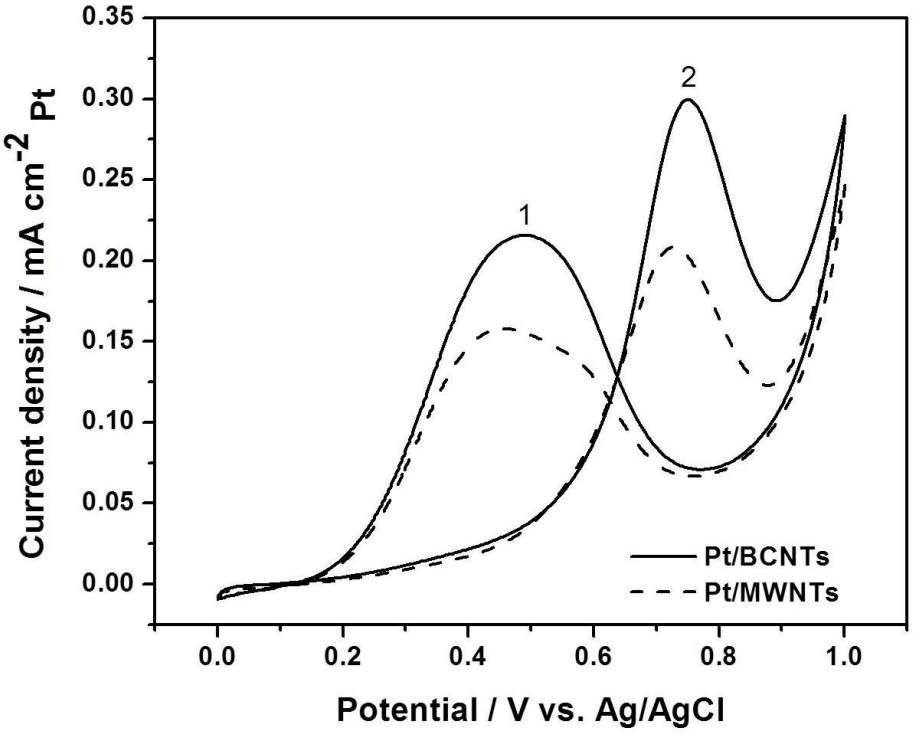

Figure 3.8 Cyclic voltammograms (a) Pt/BCNT electrocatalysts (solid) and (b) Pt/MWNT electrocatalysts (dash) in 1.0 M H_2SO_4 + 1.0 M CH_3OH solution at a scan rate of 50 mVs^{-1}. The current densities are normalized to the ECSA.

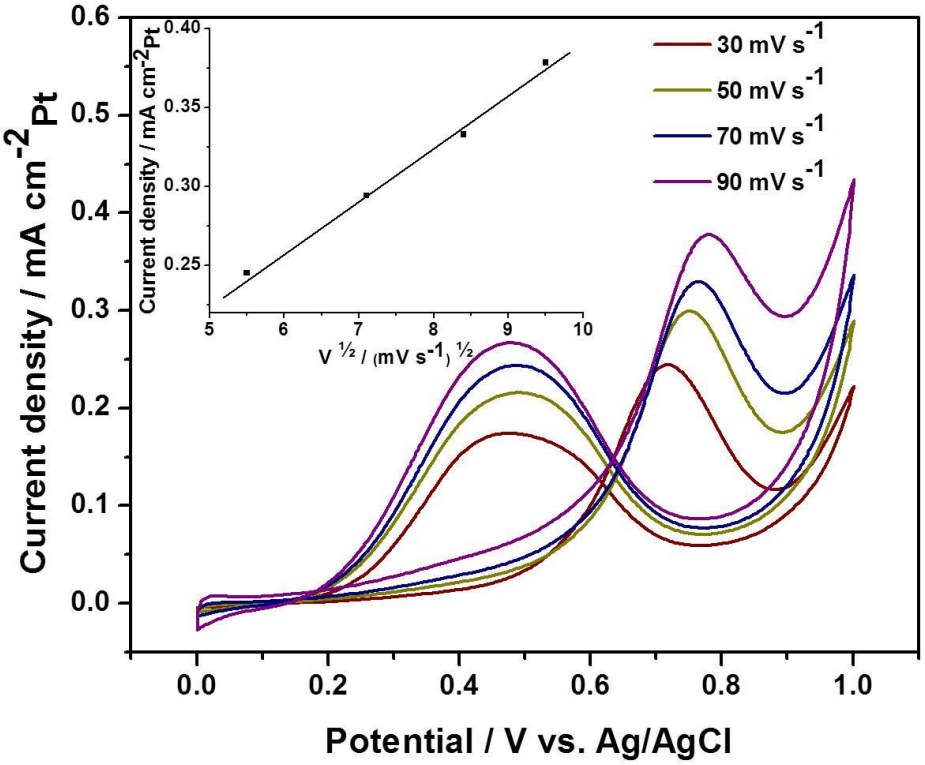

Figure 3.9 Cyclic voltammograms of 1.0 M H_2SO_4 + 1.0 M CH_3OH solution at Pt/BCNT electrocatalysts prepared with ultrasonic treatment for 10min at different scan rates. Inset: the plot of peak current density (forward scan) vs. square root of sweep rates. The current densities are normalized to the ECSA.

Fig. 3.9 shows a comparison of the CV curves of Pt/BCNTs at different scan rate in the in 1.0 M H_2SO_4 + 1.0 M CH_3OH aqueous solutions. Each curve shows the similar shape but the current density increases with the increasing scan rate. The cyclic voltammogram will take a longer time to record as the scan rate decreases, which means that the diffusion layer will grow further from the electrode surface under a slow scan rate compared to a fast one. Therefore, the flux to the electrode surface is smaller at slow scan rates than it is at faster rates. As the current is proportional

to the flux towards the electrode, the current will be lower at slow scan rates and higher at high rates. Meanwhile, it's worth noting that the peak current densities (forward scan) are linearly proportional to the square root of scan rate ($v^{1/2}$), as shown in the inset, suggesting that the electrocatalytic oxidation of methanol on Pt/BCNTs electrocatalyst could be diffusion controlled process [55]. On the other hand, with increasing scan rate, another observation is that there's a shift in the forward anodic peak along the potential axis. This could be attributed to the quasi-reversible behavior on the electrode surface. In quasi-reversible electron transfer reactions, the electron transfer is too slow for equilibrium to be maintained. The rate of change of potential is faster than the rate of adjustment of current. Thus current takes more time to response to the applied voltage than that in the reversible reaction. The more time is needed at relative high scan rate than at slow scan rate [56].

Chronoamperometry studies of Pt/BCNTs and Pt/MWNTs toward methanol oxidation reaction were recorded at 0.75 V in solution containing 1.0 M H_2SO_4 + 1.0 M CH_3OH. Chronoamperograms can be used to check if there is a rapid electrocatalyst poisoning upon methanol oxidation. As it can be observed in Fig. 3.10, current density decreased rapidly within 300 s and then decayed slightly for a long duration (2200 s). For electrocatalysts, the sharp decrease at initial stage might be attributed to the double-layer charging and the formation of intermediate species such as COads on Pt NPs which can block the methanol oxidation reaction to some degree. At long reaction time, the rate of current decay is small and a pseudo-steady state current is achieved [57-59]. It can be found that the steady state current density of Pt/BCNTs is higher than that of Pt/MWNTs. On the other hand, current decay for the reaction on Pt/BCNT electrocatalyst was slower than on Pt/MWNT electrocatalyst. These observations further confirm that Pt/BCNT electrocatalysts can lead to higher catalytic activity for methanol oxidation than Pt/MWNT

electrocatalysts and imply the effect of the BCNTs as support in increasing the electrochemical activity of the electrocatalyst.

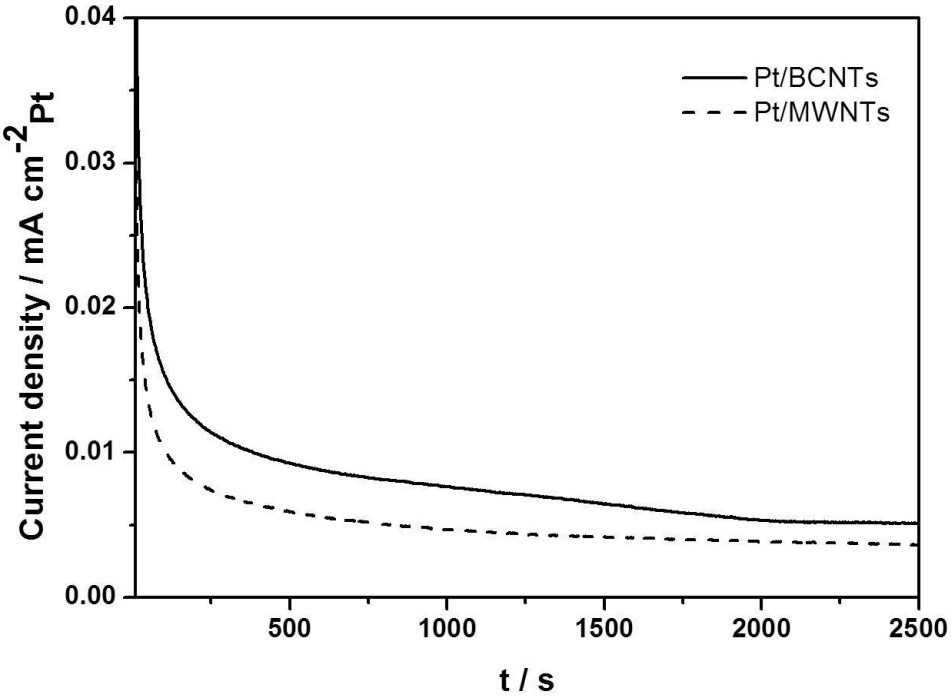

Figure 3.10 Chronoamperometry of Pt/BCNT electrocatalysts (solid) and Pt/MWNT electrocatalysts (dash) at 0.75 V, measured in 1.0 M H_2SO_4 + 1.0 M CH_3OH solution. The current densities are normalized to the ECSA.

Based on the above results, it is concluded that Pt/BCNT electrocatalysts with larger ECSA will offer more electrochemical reaction sites than Pt/MWNTs. It is believed that the compartmentalized bamboo–like structure of N–doped CNTs have large numbers of defective sites and active sites on the surface, which can greatly enhance the nucleation of nanocrystalline metals onto CNTs. Table 3.1 shows the comparison of bamboo shaped carbon nanotube supported catalyst synthesized with different methods for methanol electrooxidization. It can be found that our method processes the shortest catalyst synthesis time compared to others listed in the table. This

may be because the high power ultrasonic field possessing high energy which could accelerate the mass transport and the reactant diffusion speed, resulting in a high–reacting speed.

Table 3.1 Comparison of bamboo shaped carbon nanotube supported catalyst for methanol electro oxidation.

Catalyst	Size(nm)	Nitrogen content (%)	Catalyst synthesis time	Activity	Reference
PtRu	2-3	N/A	More than 10 h	~180 A g^{-1} at 0.7 V vs. NHE	[14]
Pt	2-3	N/A	4.5h	~0.12 mA cm^{-2}_{Pt} at 0.6 V vs. NHE	[22]
Pt	3.14	2	3.5h	~75 A g^{-1} at 0.58 V vs. SHE	[60]
Pt	2-4	3	Less than 1 h	~0.31 mA cm^{-2}_{Pt} at 0.75 V vs. Ag/AgCl	This work

3.4 Conclusions

In summary, BNCTs with high defect density and reactivity have been synthesized and used as the electrocatalyst support materials in DMFCs. The Pt nanoparticles were uniformly dispersed on BCNTs by using high power ultrasound. From the density functional theory calculations of different Pt/CNT systems, we found that the addition of nitrogen facilitates Pt binding to the CNTs and improve methanol reactivity. And the electrochemical studies showed that the as–prepared Pt/BCNT electrocatalysts indeed exhibited a remarkable enhancement in catalytic activity for methanol oxidation compared to that of the Pt/MWNT electrocatalysts. We believe that this synthetic strategy could be useful for the synthesis of other metal/carbon electrocatalysts. Intensive investigation is under progress in our laboratory.

Acknowledgement

This work was supported by National Science Foundation (CMMI–1030289). The authors would like to thank Dr. Kathleen Wang for her help in using high–intensity ultrasonic probe in Professor Terri Camesano's lab in WPI, Jack Hirsch for his help in analyzing XPS in Umass Amherst and Sia Najafi for his help in using WPI's computer clusters.

References

[1] S.Ghosh, C.R. Raj, J. Phys. Chem. C 114 (2010) 10843-10849.

[2] W. Xiong, F. Du, Y. Liu, P. Abert, M. Supp, T.S. Ramakrishnan, L. M. Dai, et al., J. Am. Chem. Soc. 132 (2010) 15839-15841.

[3] A. Halder, S. Sharma, M.S. Hegde, N. Ravishankar ,J. Phys. Chem. C 113 (2009) 1466-1473.

[4] K. Shimizu, J.S Wang., C.M. Wai, J. Phys. Chem. A 114 (2010) 3956-3961.

[5] S. Sharma, B.G. Pollet, J. Power Sources 208 (2012) 96-119.

[6] Y. Lin, X. Cui, C. Yen, C.M. Wai, J. Phys. Chem. B: Conden. Phase 109 (2005) 14410-14415.

[7] J. Kua, W.A. Goddard III, J. Am. Chem. Soc. 121 (1999) 10928-10941.

[8] J. Chen, M. Wang, B. Liu, Z. Fan, K. Cui, Y. Kuang, J. Phys. Chem. B 110 (2006) 11775-11779.

[9] S.J. Jiang, L. Zhu, Y.W. Ma, X.Z. Wang, J.G. Liu, J.M. Zhu, Y. N. Fan, et al., J. Power Sources 195 (2010) 7578-7582.

[10] Y.T. Kim, K. Ohshima, K. Higashimine, T. Uruga, M. Takata, H. Suematsu, T. Mitani, Angew. Chem., Int. Ed. 45 (2006) 407-411.

[11] N. Mackiewicz, G. Surendran, H. Remita, B. Keita, G. Zhang, L. Nadjo, A. Hagège, et al., J.

Am. Chem. Soc. 130 (2008) 8110-8111.

[12] C.H. Hsu, P.L. Kuo, J. Power Sources 198 (2012) 83-89.

[13] L. Gan, R. Lv, H.D. Du, B.H. Li, F.Y. Kang, Electrochem. Commun. 11 (2009) 355-358.

[14] M.S. Saha, R.Y. Li, X.L. Sun, S.Y. Ye, Electrochem. Commun. 11 (2009) 438-444.

[15] K.P. Gong, F. Du, Z.H. Xia, M. Durstock, L.M. Dai, Science 323 (2009) 760-764.

[16] Y.F. Tang, B.L. Allen, D.R. Kauffman, A. Star, J. Am. Chem. Soc. 131 (2009) 13200-13201.

[17] B.G. Sumpter, V. Meunier, J.M. Romo-Herrera, E. Cruz-Silva, D.A. Cullen, H. Terrones, D.J. Smith, et al., ACS Nano, 1 (2007) 369-375.

[18] S.J. Jiang, Y.W. Ma, G.Q. Jian, H.S. Tao, X.Z. Wang, Y.N. Fan, Y.N. Lu, et al., Adv. Mater. 21 (2009) 4953-4956.

[19] Z. Yang, H.G. Nie, X.A Chen, X.H. Chen, S.M. Huang, J. Power Sources 236 (2013) 238-249.

[20] Y.Y. Shao, J.H. Sui, G.P. Yin, Y.Z. Gao, Appl. Catal. B. 79 (2008) 89-99.

[21] L. Gan, R. Lv, H.D. Du, B.H. Li, F.Y. Kang, Carbon 47 (2009) 1833-1840.

[22] L. Shi, R.P. Liang, J.D. Qiu, J. Mater. Chem. 22 (2012) 17196-17203.

[23] C. Wang , M. Waje, X. Wang, J.M. Tang, R.C. Haddon, Y.S. Yan, Nano Lett. 4 (2004) 345-348.

[24] J.P. Qian, W. Wei, X.B. Huang, Y.M. Tao, K.Y. Chen, X.Z. Tang, J. Power Sources 210 (2012) 345-349.

[25] C.A. Angelucci, S.M. D'Villa, F.C. Nart, Electrochimi. Acta. 52 (2007) 7293-7299.

[26] G.P. Bruno, Int. J. Hydrogen Energy 35 (2010) 11986-12004.

[27] D. Thompsett, Catalysts for the Proton exchange membrane fuel cell, In: Hoogers G, editor,

Fuel cell technology handbook, CRC Press, 2003, p. 6.20.

[28] W. Kim, D.Y. Choi, S.B. Kim, Mater. Tran. 51 (2010) 1694-1698.

[29] Z.Z. Zhu, J.L. Wang, A. Munir, H.S. Zhou, Electrochim. Acta. 55 (2010) 8517-8520.

[30] C.N. He, N.Q. Zhao, C.S. Shi, X.W. Du, J.J. Li, J. Alloy. Compd. 433 (201) 79-83.

[31] J. VandeVondele, M. Krack, F. Mohamed, M. Parrinello, T. Chassaing, J. Hutter, Comput. Phys. Commun. 16 (2005) 103-128.

[32] G. Lippert, J. Hutter, M. Parrinello, Mol. Phys. 92 (1997) 477-488.

[33] J. VandeVondele, J. Hutter, J. Chem. Phys. 11(2007) 114105-114113.

[34] S. Goedecker, M. Teter, J. Hutter, Phys. Rev. B. 54 (1996) 1703-1710.

[35] M.T. Krack, Chem. Accounts 114 (2005) 145-152.

[36] J.P. Perdew, K. Burke, M. Ernzerhof, Phys. Rev. Lett. 77 (1996) 3865-3868.

[37] G.M. An, P. Yu, L.Q. Mao, Z.Y. Sun, Z.M. Liu, S.D. Miao, Z.J. Miao, et al., Carbon 45 (2007) 536-542.

[38] P. Ayala, R. Arenal, M. Rummeli, A. Rubio, T. Pichler, Carbon 48 (2010) 575-586.

[39] I. Florea, O. Ersen, R. Arenal, D. Ihiawakrim, C. Messaoudi, K. Chizari, I. Janowska, et al. J Am. Chem. Soc. 134 (2012) 9672-9680.

[40] C.H. Hsu, H.M. Wu, P.L. Kuo, Chem. Commun. 46 (2010) 7628-7630.

[41] J.W. Jang, C.E. Lee, C.I. Oh, C.J. Lee, J. Appl. Phys. 98 (2005) 74316-74319.

[42] C.E. Banks, R.G. Compton, Analyst 131 (2006) 15–21.

[43] C.J. Lee, J.H. Park. Appl. Phys. Lett. 77 (2000) 3397–3399.

[44] H. Terrones, R. Lv, M. Terrones, M.S. Dresselhaus, Rep. Prog. Phys. 75 (2012) 62501-62530.

[45] S. Stafström, Appl. Phys. Lett. 77 (2000) 3941-3943.

[46] E. Raymundo–Pinero, D. Cazorla–Amoros, A. Linares–Solano, J. Find, U. Wild, R. Schlogl, Carbon 40 (2002) 597-608.

[47] J.R. Pels, F. Kapteijn, J.A. Moulijn, Q. Zhu, K.M. Thomas, Carbon 33 (1995) 1641-1653.

[48] R. Czerw, M. Terrones, J.C. Charlier, X. Blase, B. Foley, R. Kamalakaran, N. Grobert, et al., Nano Lett. 1 (2001) 457-460.

[49] D. Cao, G.Q. Lu, A. Wieckowski, S.A. Wasileski, M.J. Neurock, J. Phys. Chem. B 109 (2005) 11622-11633.

[50] W. Zhong, Y. Liu, D. Zhang, J. Mol. Model. 18 (2012) 3051-3060.

[51] Y. Zhou, K. Neyerlin, T.S. Olson, S. Pylypenko, J. Bult, H.N. Dinh, R. O'Hayre, Energy Environ. Sci. 3 (2010) 1437-1446.

[52] M. Freemantle, Chem. Eng. News 74 (1995) 62-64.

[53] L. Wei, Y.J. Fan, J.H. Ma, L.H. Tao, R.X. Wang, J.P. Zhong, H. Wang, J. Power Sources V 238 (2013) 157-164.

[54] K. Honda, M. Yoshimura, T.N. Rao, D.A. Tryk, A. Fujishima, J. Electroanal. Chem. 514 (2001) 35-50.

[55] S. Roy, H. Vedala, W. Choi, Nanotechnology 17 (2006) S14-S18.

[56] H.Y. Lee, W. Vogel, P.P. Chu, ECS Trans. 19 (2009) 127-142.

[57] J.W. Guo, T.S. Zhao, J. Prabhuram, R. Chen, C.W. Wang, Electrochim. Acta. 51 (2005) 754-763.

[58] A. Kabbabi, R. Faure, R. Durand,B. Beden, F. Hahn, J.M. Leger, C Lamy, J. Electroanal. Chem. 444 (1998) 41–53.

[59] W.C. Fang, Nanoscale Res. Lett. 5 (2010) 68-73.

Supplementary information

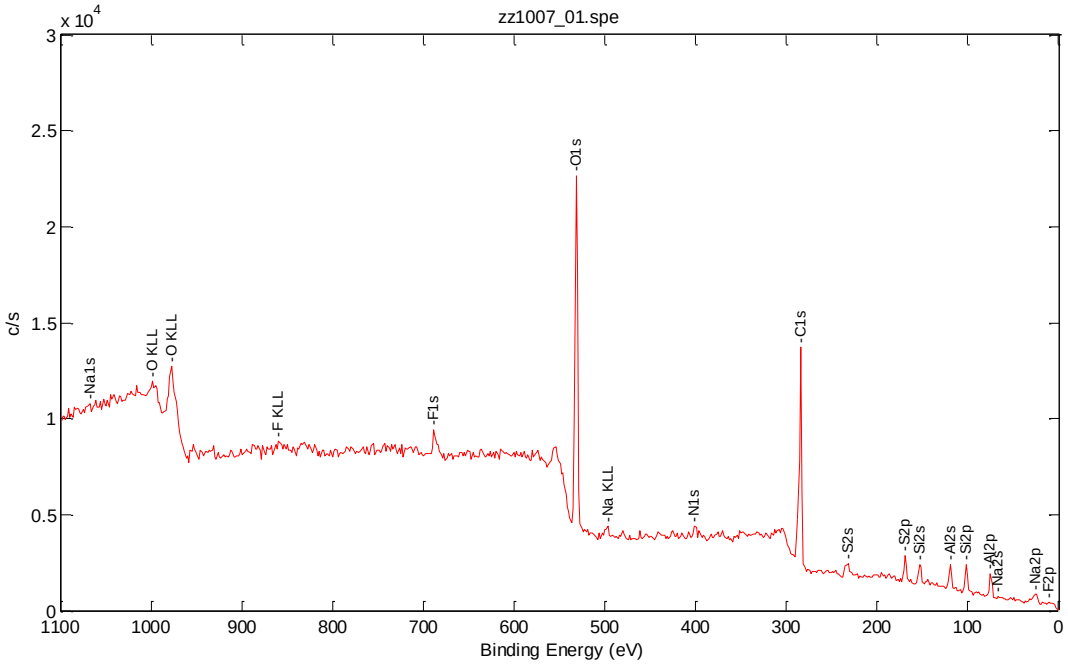

Figure S3.1 XPS of MWNTs.

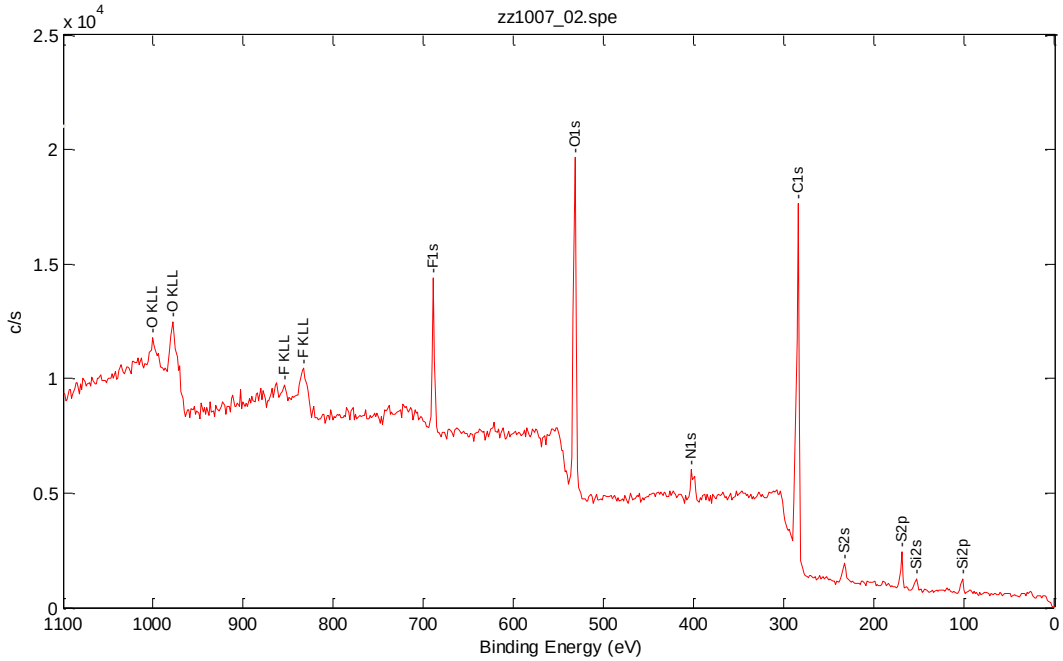

Figure S3.2 XPS of BCNTs.

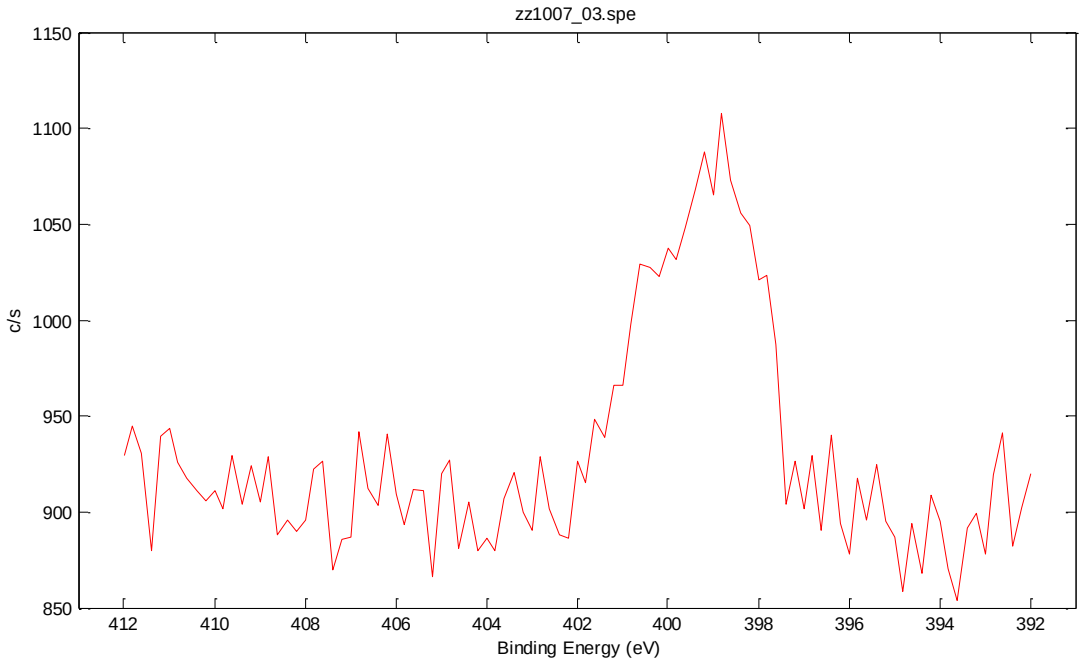

Figure S3.3 Deconvolution of the XPS spectra in the N 1s region for MWNTs.

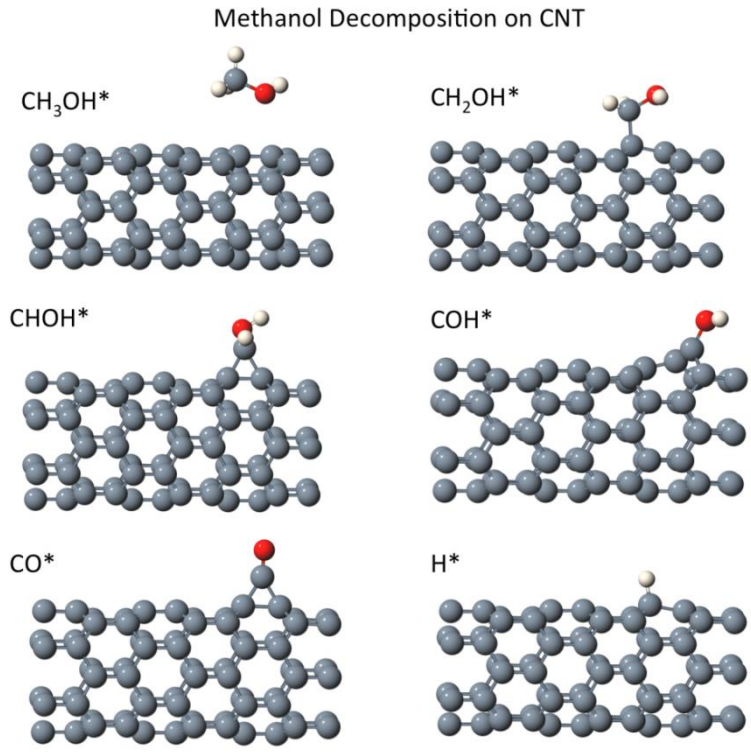

Figure S3.4 Adsorbed intermediates for methanol decomposition over a CNT.

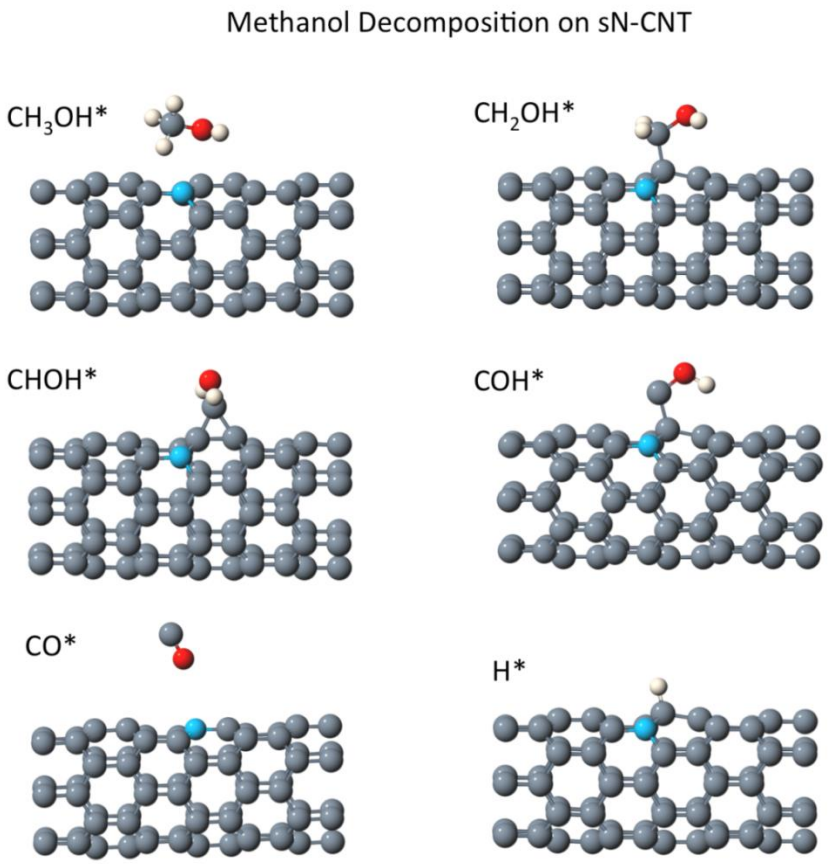

Figure S3.5 Adsorbed intermediates for methanol decomposition over a sN-CNT.

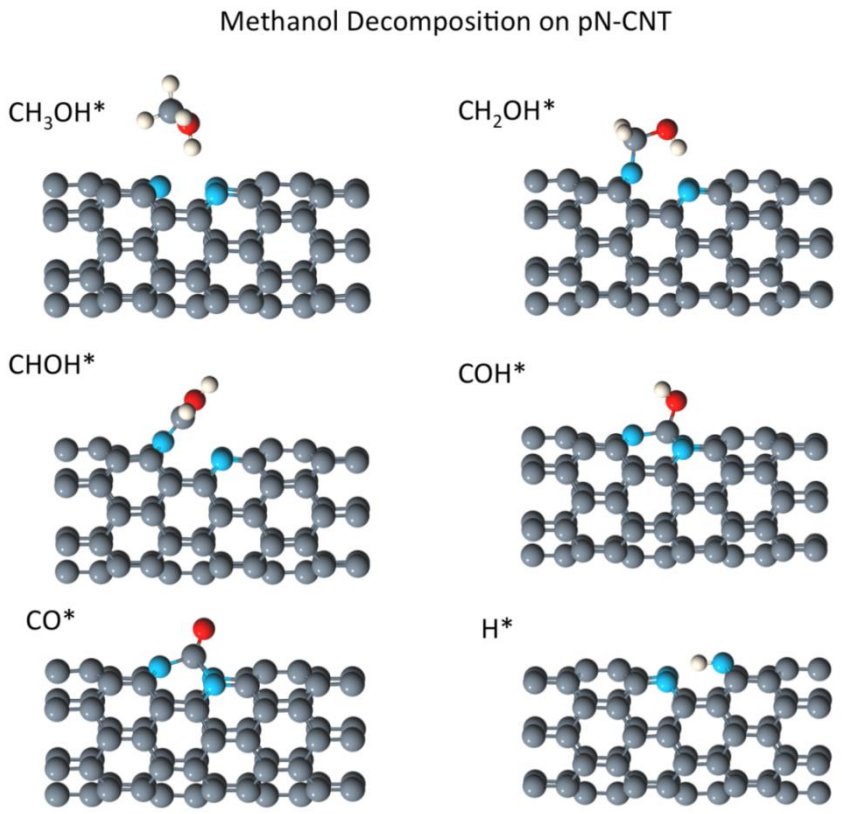

Figure S3.6 Adsorbed intermediates for methanol decomposition over a pN-CNT.

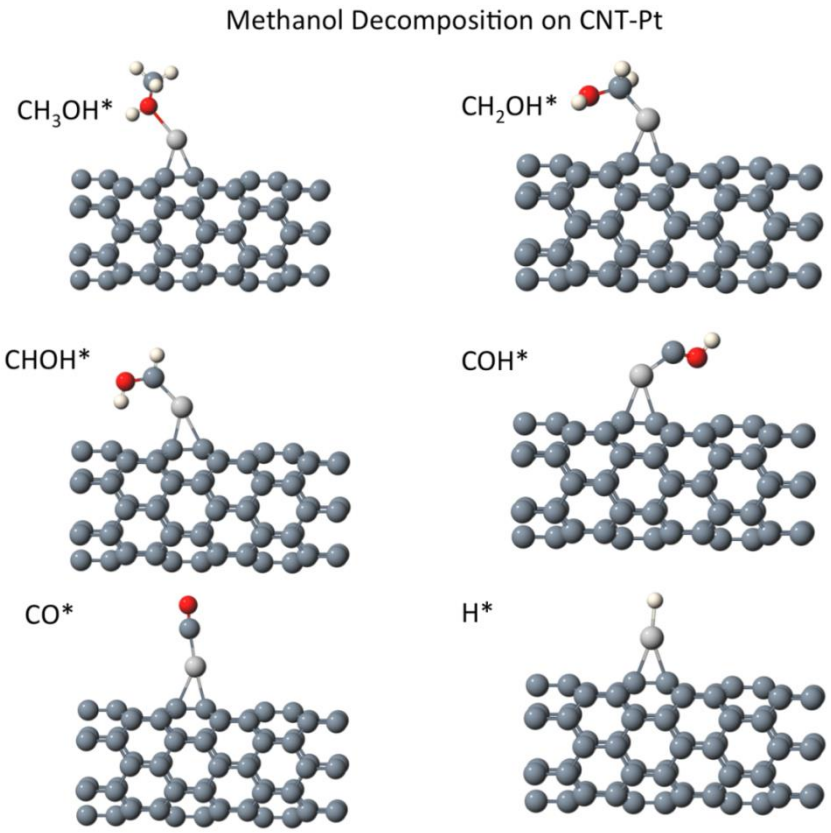

Figure S3.7 Adsorbed intermediates for methanol decomposition over a Pt-CNT.

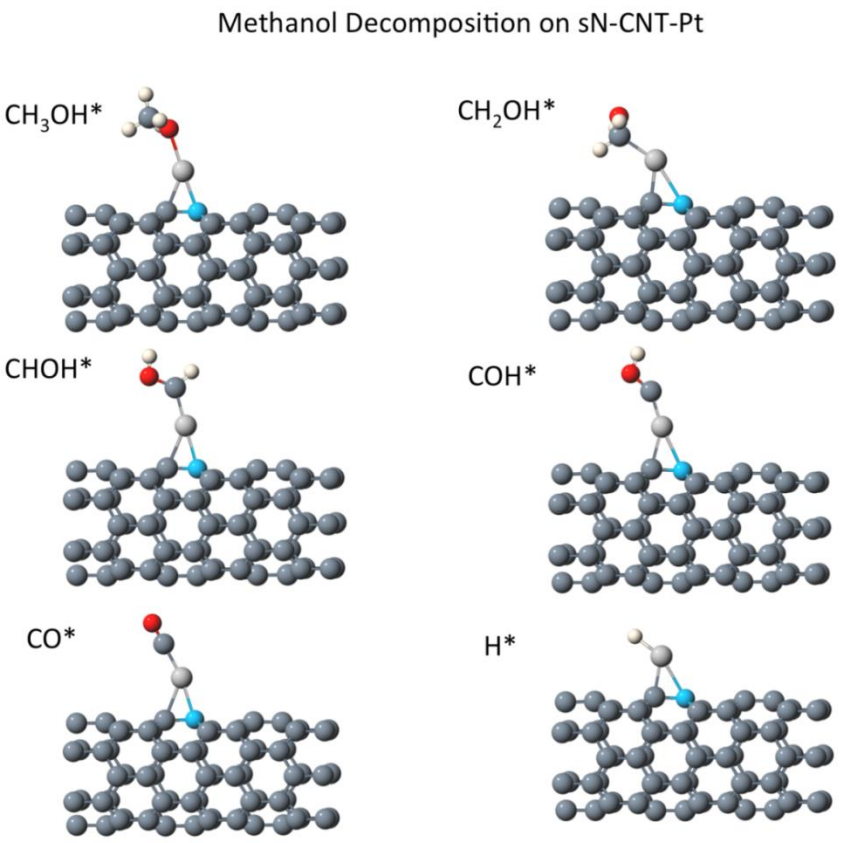

Figure S3.8 Adsorbed intermediates for methanol decomposition over a Pt-sN-CNT.

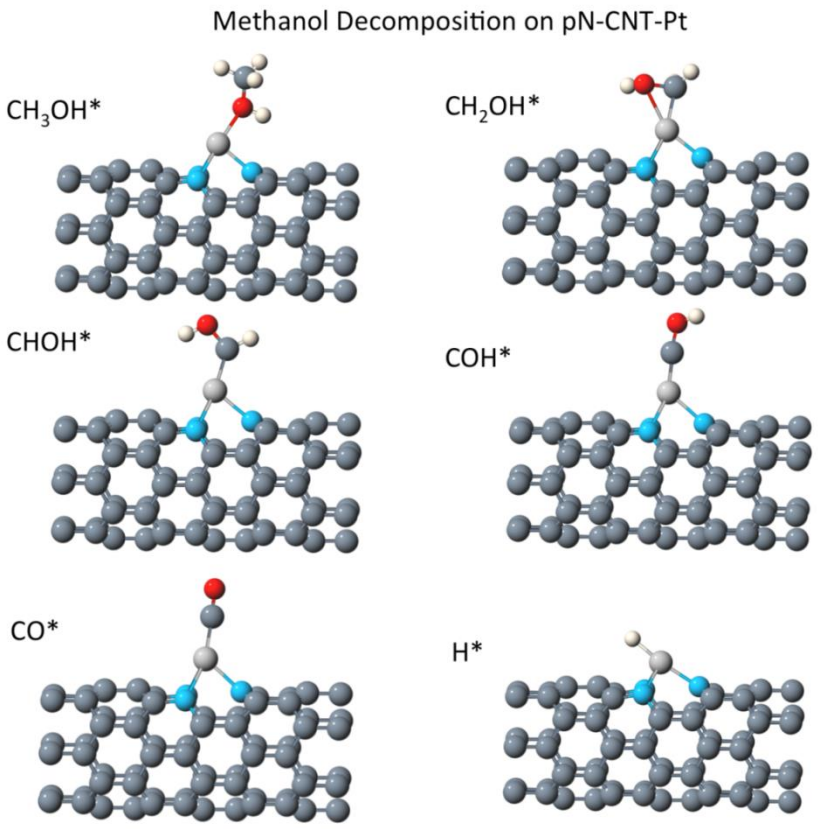

Figure S3.9 Adsorbed intermediates for methanol decomposition over a Pt-pN-CNT.

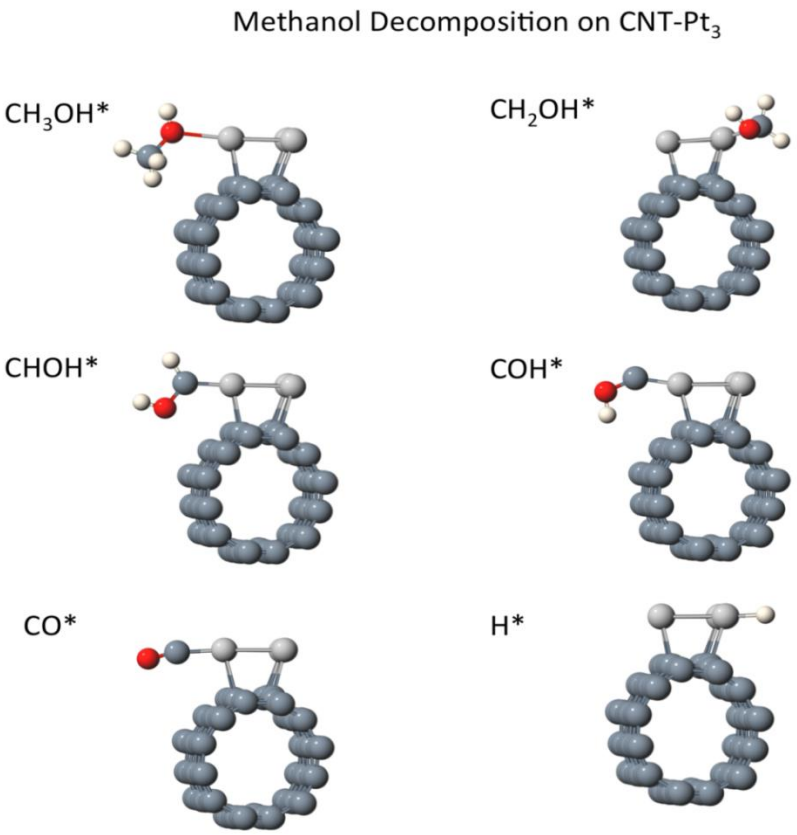

Figure S3.10 Adsorbed intermediates for methanol decomposition over a Pt_3-CNT.

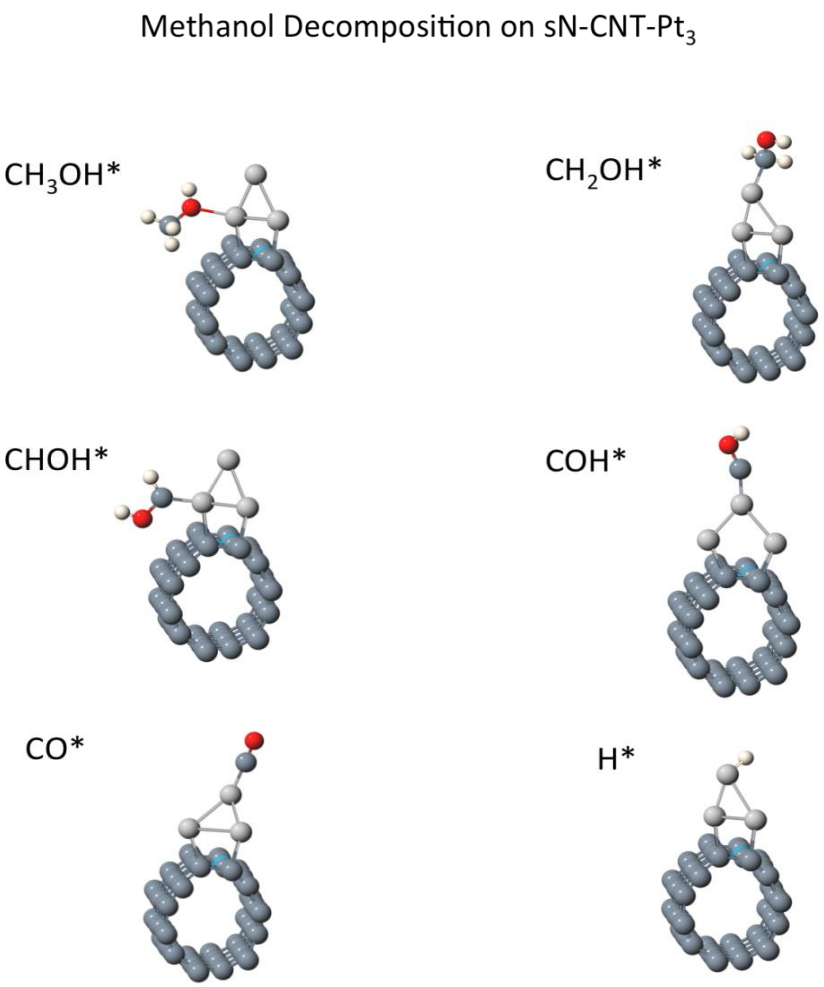

Figure S3.11 Adsorbed intermediates for methanol decomposition over a Pt_3-sN-CNT.

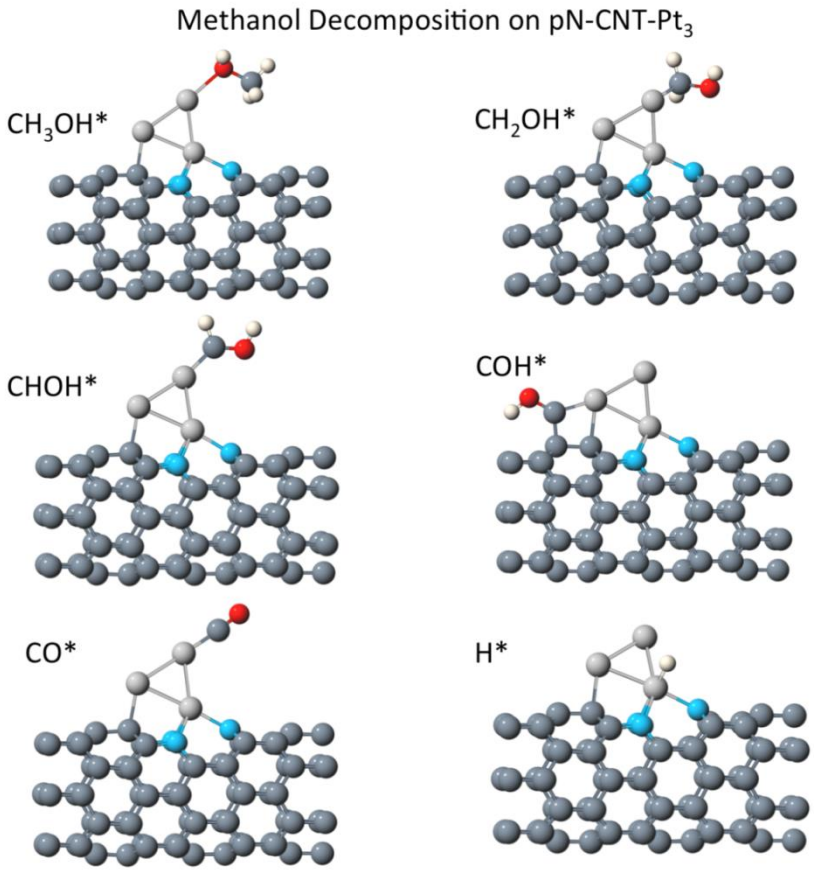

Figure S3.12 Adsorbed intermediates for methanol decomposition over a Pt_3-pN-CNT.

Chapter 4 Direct electrochemistry and electrocatalysis of horseradish peroxidase immobilized on bamboo shaped carbon nanotube/chitosan matrix

Abstract

The novel nitrogen doped bamboo shaped carbon nanotubes (BCNTs) have received increased attention in recent years because of its unique bamboo shaped structure associated properties. In this work, a nanocomposite film of bamboo shaped carbon nanotubes/chitosan (Chi) is used for the immobilization of horseradish peroxidase (HRP). The structure of BCNTs is observed by transmission electron microscopy (TEM). The composite films are characterized by scanning electron microscopy (SEM). Direct electrochemistry and electrocatalysis of HRP incorporated into bamboo shaped carbon nanotubes/chitosan matrix is also investigated in this work. The immobilized HRP onto the BCNTs/Chi film exhibits its bioelectrocatalytic activity to hydrogen peroxide. The results indicate that doping N atom introduces defective sites and active sites on the surface of carbon nanotubes, thereby facilitating the direct electron transfer on their surface.

This work has been published in Colloids and Surfaces A: Physicochemical and Engineering Aspects 385 (2011) 91-94.

4.1 Introduction

The direct electron transfer (DET) between the redox proteins/enzymes and the electrode surface plays an important role for understanding the kinetics and thermodynamics of biological redox process [1-3], and provides foundation for fabricating wide array of protein based biosensor, biomedical devices, and enzymatic reactors [4-6]. However, it's difficult to study the direct electrochemistry of enzyme with an unmodified electrode because the redox centers are embedded deeply into the structure of the enzyme and are far away from the electrode surface. Moreover, the electron transfer rates around the redox center are slow because of the low electronic conductivity of the surrounding amino acid chains [7-9]. To overcome these drawbacks, extensive research has been done focusing on new materials and suitable methods to immobilize enzyme on electrodes in order to obtain their direct electrochemical reactions and retain their bioactivities [10-12].

Recently, nanomaterials have been widely used for the modification of electrode on the molecular scale [13, 14]. Carbon nanotubes (CNTs), as an important class of promising nanomatrials, have attracted a great deal of attention both in fundamental research and practical application [15-20]. Their outstanding physical, mechanical and multifunctional properties allow a wide range of potential applications such as nanocomposite materials, biomedical engineering, nanoelectronics, energy storage, devices, etc [21-23]. In recent years，CNTs have been widely used to study the DET of proteins or enzymes because of their high surface-to-volume ratios and fast electron transfer kinetics [24, 25]. It is well known that the major problem in using CNTs for biological systems is their poor dispersability in solvents because of their strong intertube van der Waals interactions [26]. For biological applications, surface functionalization is required in order to solubilize CNTs and to render biocompatibility. Although various reactions have been developed to change the surface structure of CNTs to achieve a high enzymes/proteins loading, most of them

require strict reaction conditions together with highly complicated procedure. Doping of some foreign atoms was recently demonstrated to be a simpler and more effective way to control the structural and electronic properties of nanotubes [27-29]. It has been demonstrated in various literature that the bamboo-shaped structures are formed as long as the reaction gases containing nitrogenous gas or the nitrogenous precursors are employed during preparation of CNTs [30-33]. A large number of defective sites and active sites were introduced onto the surface of CNTs during their synthesis in order to obtain such nitrogen-doped bamboo shaped carbon nanotubes (BCNTs)[34]. BCNTs developed with this procedure are able to keep one-dimensional graphite nanostructure, possess higher chemical activity [35, 36], and also have proved to be advantageous for the immobilization of heme protein to facilitate its direct electron transfer [37, 38].

Herein, BCNTs were successfully synthesized through chemical vapor deposition (CVD) by using acetonitrile as nitrogenous precursors. The resulted BCNTs were used to directly immobilize horseradish peroxidase (HRP), one of the most commonly studied enzymes, in the presence of chitosan (Chi) (Scheme 4.1). The use of Chi would offer a quick and effective method to disperse BCNTs. As an important natural biocompatible material, Chi not only solubilizes CNTs in aqueous solution, but also facilitates the immobilization of enzymes [39, 40]. In this work, a hybrid organic-inorganic nanocomposite film of BCNTs/Chi was constructed to immobilize HRP. Neither rigorous reaction conditions nor complicated procedure were needed in the whole process. Physical immobilization of HRP on BCNTs/Chi was investigated using SEM, direct electrochemical behavior of HRP towards H_2O_2 has been studied in detail in this work.

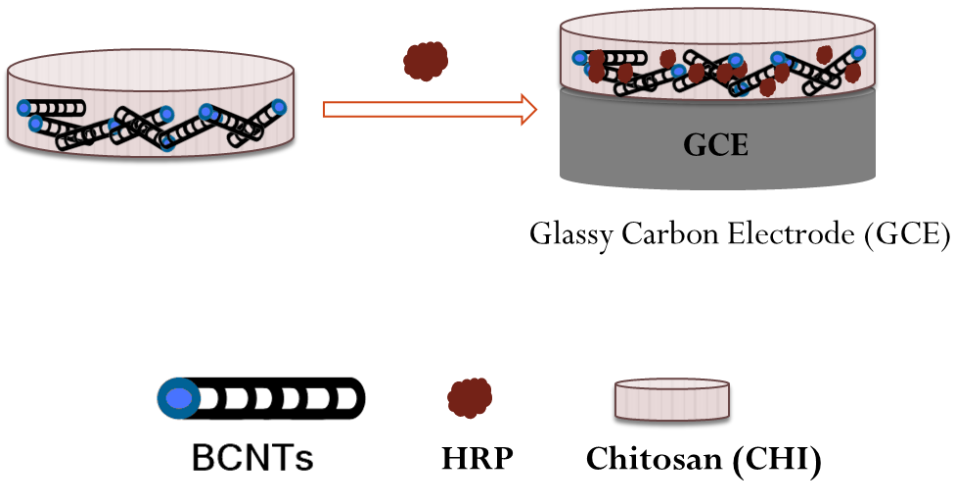

Scheme 4.1 Schematic representation of the immobilization of HRP on BCNT/chitosan matrix.

4.2 Experimental

4.2.1 Preparation of BCNTs

Nitrogen-doped bamboo shaped carbon nanotubes (BCNTs) used in this work were synthesized via CVD by using acetylene (C_2H_2) and acetonitrile (CH_3CN) as the carbon and nitrogen source. Here, catalyst of Fe/Mg with the weight ratio of 1/9 was put into a ceramic boat and set in the CVD reaction tube. The furnace was heated up to 800 °C. Then CH_3CN and C_2H_2 with the volume ratio of 7/1 were introduced into the tube for 15 mins. After the furnace was cooled to room temperature, the black products were collected, and then purified by HCl solution to remove the residual catalyst. The whole process was protected by N_2. The details are similar to those described in Ref [41]. For comparison, undoped multi-walled carbon nanotubes (MWNTs) were prepared using C_2H_2 as carbon source while other conditions unchanged.

4.2.2 Preparation of HRP/BCNTs/Chi electrode

In order to investigate the electrochemical property by Cyclic voltammogram (CV), glassy carbon (GC) working electrodes, 3 mm in diameter, was polished with 1.0 and 0.3 μm alumina slurry sequentially and then washed ultrasonically in water and ethanol for a few minutes, respectively. 1% chitosan solution was prepared by dissolving Chi in 2% acetic acid solution with magnetic stirring for 2 h. 2 mg BCNTs and 1mL of 1% Chi solution were mixed together using ultrasonic bath. Then, 10mg HRP was dissolved in 1mL of PBS solution (pH=7.0). 0.8 mL of viscous and black BCNT-Chi suspension was mixed thoroughly with 0.2 mL of HRP solution. A measured volume (5 μL) of the HRP/BCNTs/Chi mixture was spread evenly by a micropipette onto the GC electrode surface, and the electrode was covered with a small bottle and allowed to dry for over 24 h at 4 ◦C. Then an adherent and robust film electrode containing HRP/BCNTs/Chi was obtained.

4.2.3 Measurements

The morphology of BCNTs was observed on a Hitachi 600 transmission electron microscopy (TEM). The samples were prepared by dipping BCNTs ethanol solution on the Cu grids and observed at 100 kV. Scanning electron microscopy (SEM, JEOL, JSM-7000F) operating at 5kV was applied to characterize the composite films. All electrochemical measurements were carried out using an Autolab PGSTA12 electrochemical workstation. A conventional cell with a three-electrode configuration was used throughout this work. The working electrode was modified glassy carbon electrode. Platinum wire and Ag/AgCl (saturated KCl) were used as the counter electrode and the reference electrode, respectively. All the electrolytes were deaerated by bubbling nitrogen (N_2) at least 30 min before the experimental procedure. All the experiments were carried out at room temperature.

4.3 Results and discussion

4.3.1 Morphology characterizations

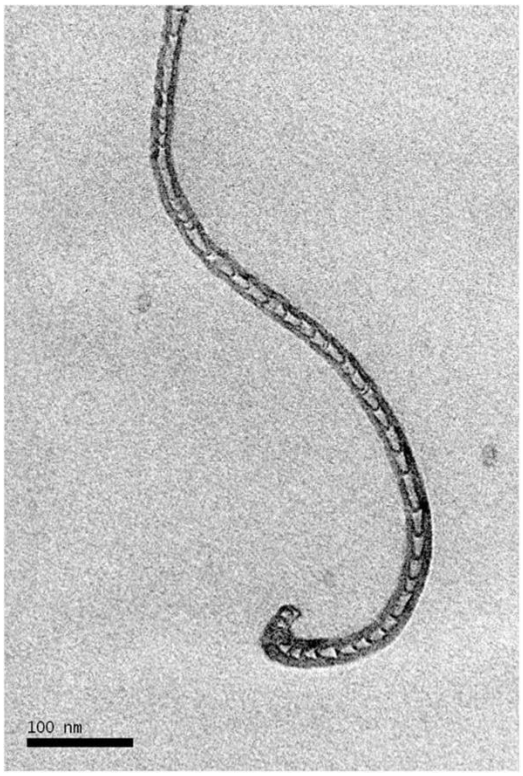

Figure 4.1 TEM image of bamboo shaped carbon nanotubes.

Fig. 4.1 presents a typical TEM image of the BCNTs, showing a very clean bamboo-shaped structure with diameter of 20-25 nm, wall thickness of 7-10 nm and the bamboo segment distance of 15-20 nm. The bamboo shape observed in nanotubes is characterized by segmented compartments, and the curvature of the compartment layers are all directed to the tube tip. From SEM images, it can be seen that chitosan film was porous with an open framework (Fig. 4.2a), and BCNTs were well dispersed into the chitosan film (Fig. 4.2b). It is because Chi facilitates the dispersion of carbon nanotubes, on the other hand, the introduction of BCNTs into the chitosan increases the electron transfer property and porosity of nanocomposite film, which leads to fast

diffusion of the analytes [42]. The surface structure of HRP/BCNTs/Chi film was shown in Fig. 4.2(c) and Fig. 4.2(d) with higher magnification. It can be seen that HRP was entrapped into the BCNTs/Chi film. And also, HRP do not agglomerate even when they are present in high density, this is because a large amount of defective and active sites are introduced on the carbon nanotube surface due to the N doping which is beneficial for loading the enzymes.

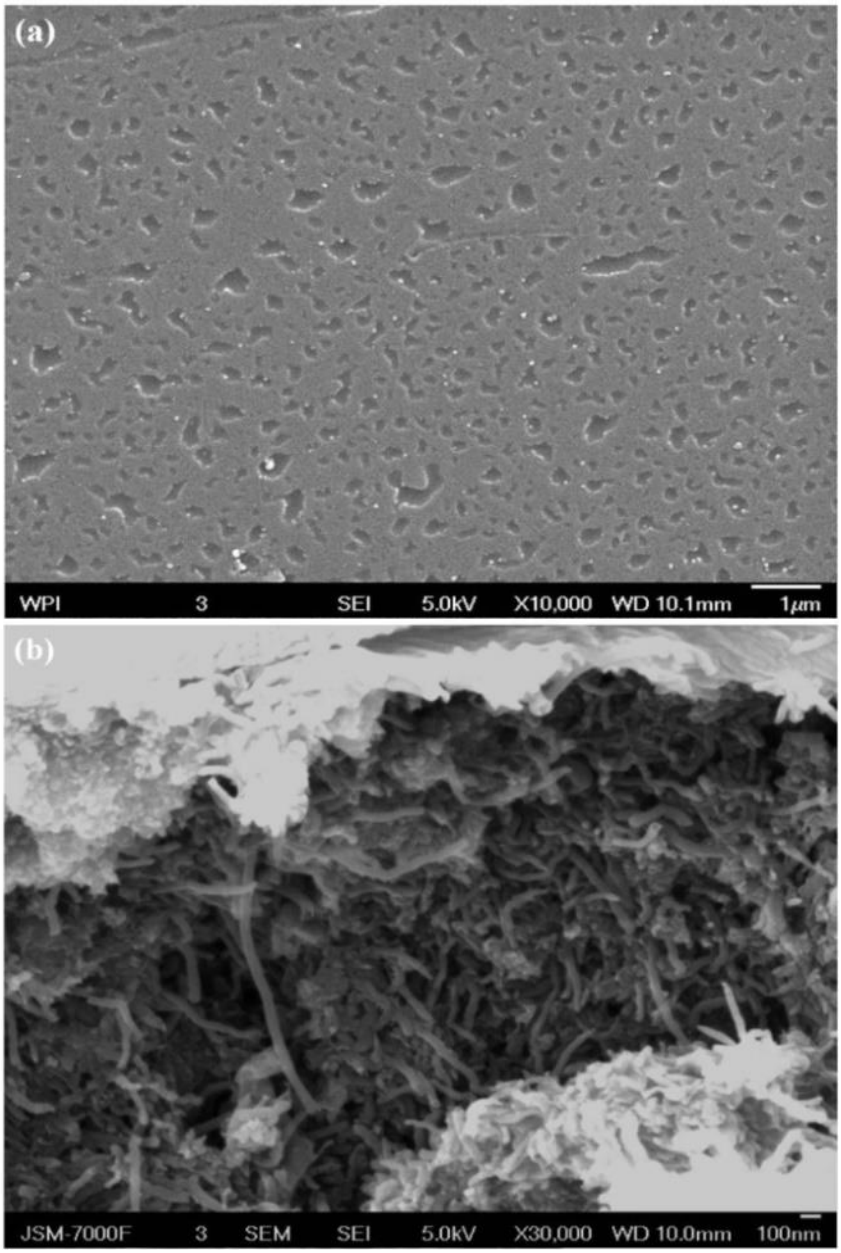

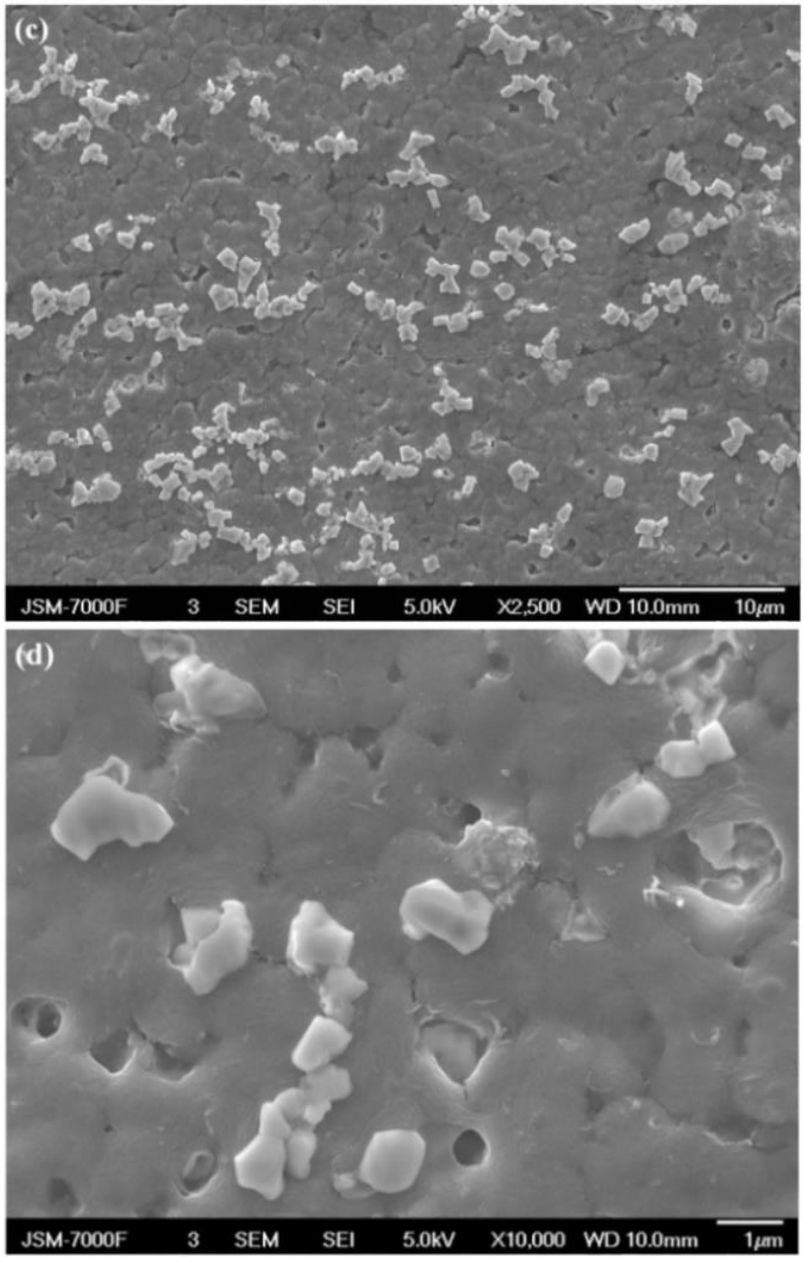

Figure 4.2 SEM images of the chitosan film(a), BCNTs/Chi film(b), HRP/BCNTs/Chi film with magnification of 2500 (c), and HRP/BCNTs/Chi film with magnification of 10000 (d), concentration of HRP: 2 mg/mL.

4.3.2 Direct electrochemical properties of HRP/BCNTs/Chi film

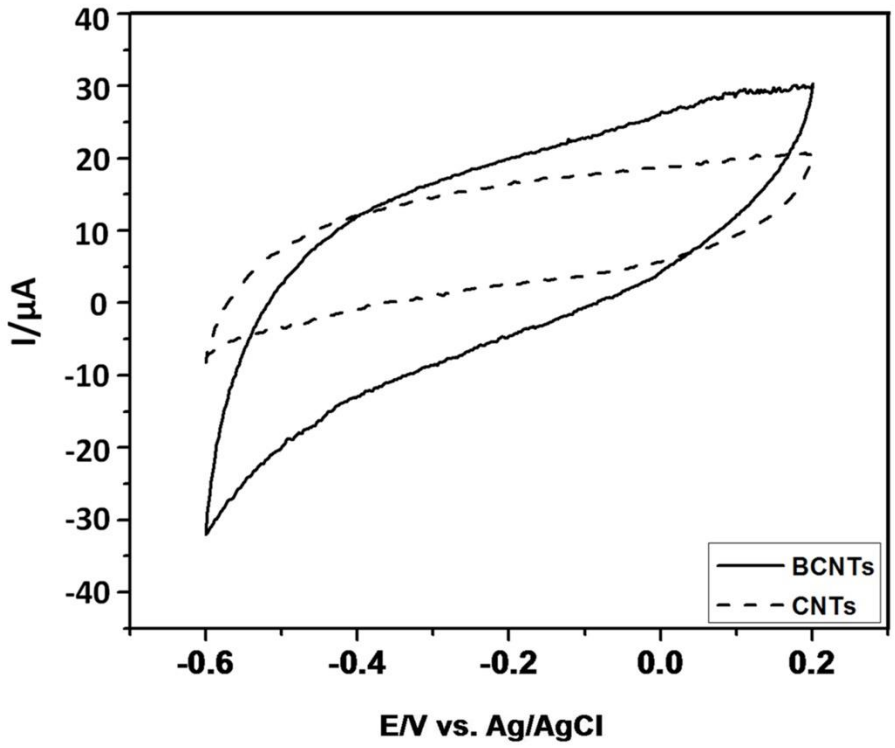

Figure 4.3 Cyclic voltammetry curves of BCNTs (solid) and CNTs (dash) in 0.1 M PBS solution (pH=7.0). Scan rate: 0.1 Vs^{-1}.

The CV curves of the GCE modified by BCNTs and MWNTs in 0.1 M pH=7.0 phosphate buffer solution (PBS) at a scan rate of 0.1 Vs^{-1} between -0.6 and +0.2 V are reported in Fig.4.3. The BCNTs/GCE (solid curve) displays a larger background current compared to MWNTs/GCE (dash curve), which means that BCNTs possess higher electrochemical active surface area, which may be owed to more defective and active sites on the BCNTs surface.

As we know, the redox center of large enzyme like HRP is deeply seated in protein shells and thus it's not easily accessible for the conduction of electrons to the electrode surface [25]. Here, we presented the CV curves of HRP absorbed on the BCNTs/Chi modified electrode in 0.1 M PBS

solution in Fig. 4.4. A pair of CV peaks can be observed in each curve, which corresponds to the conversion between HRP-Fe (III) and HRP-Fe (II) [42]. We also can find that both anodic and cathodic peak current increase linearly with the scan rate from 0.1 to 0.9 Vs^{-1} (from inner to outer), indicating a surface-controlled process [43-45]. BCNTs have the unique ability to facilitate the direct electron transfer between HRP and the electrode surface, which may be attributed to a large number of active and defective sites at the BCNTs surfaces introduced by nitrogen doping.

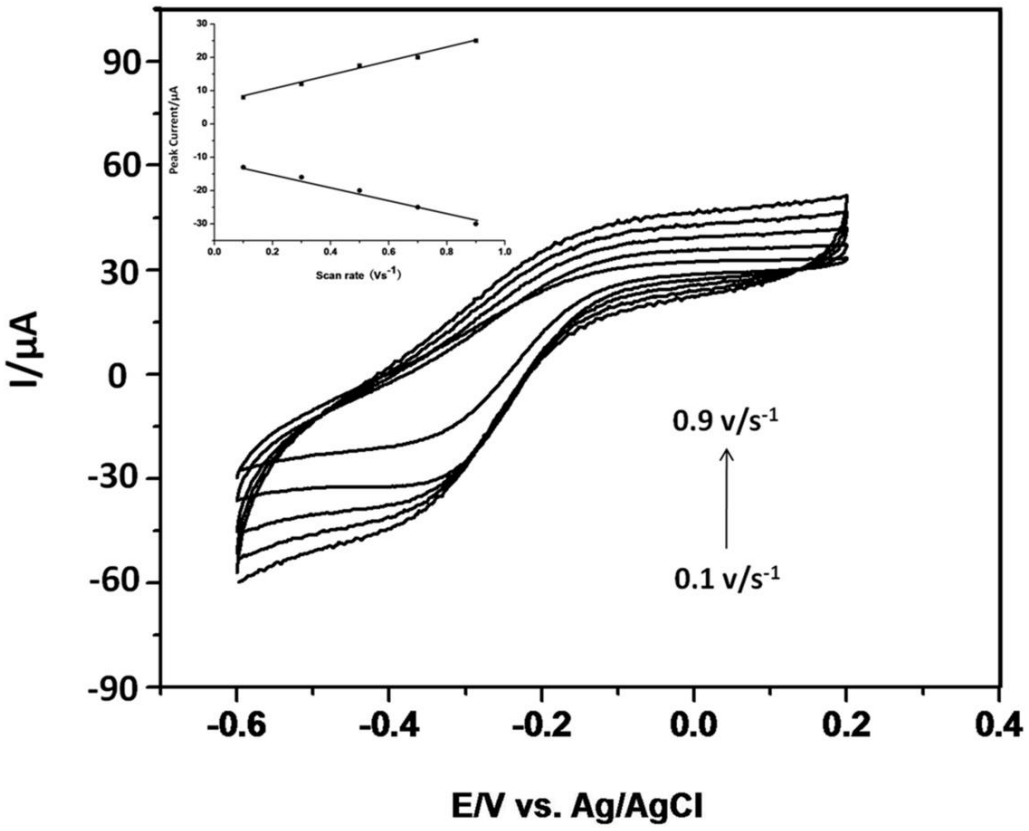

Fig. 4.4 Cyclic voltammograms of the modified GCE with HRP/BCNTs/Chi film in 0.1 M PBS (pH=7.0) at different scan rates: 0.1, 0.3, 0.5, 0.7, 0.9 Vs^{-1} (from inner to outer). Insert: the plot of peak current vs. sweep rates.

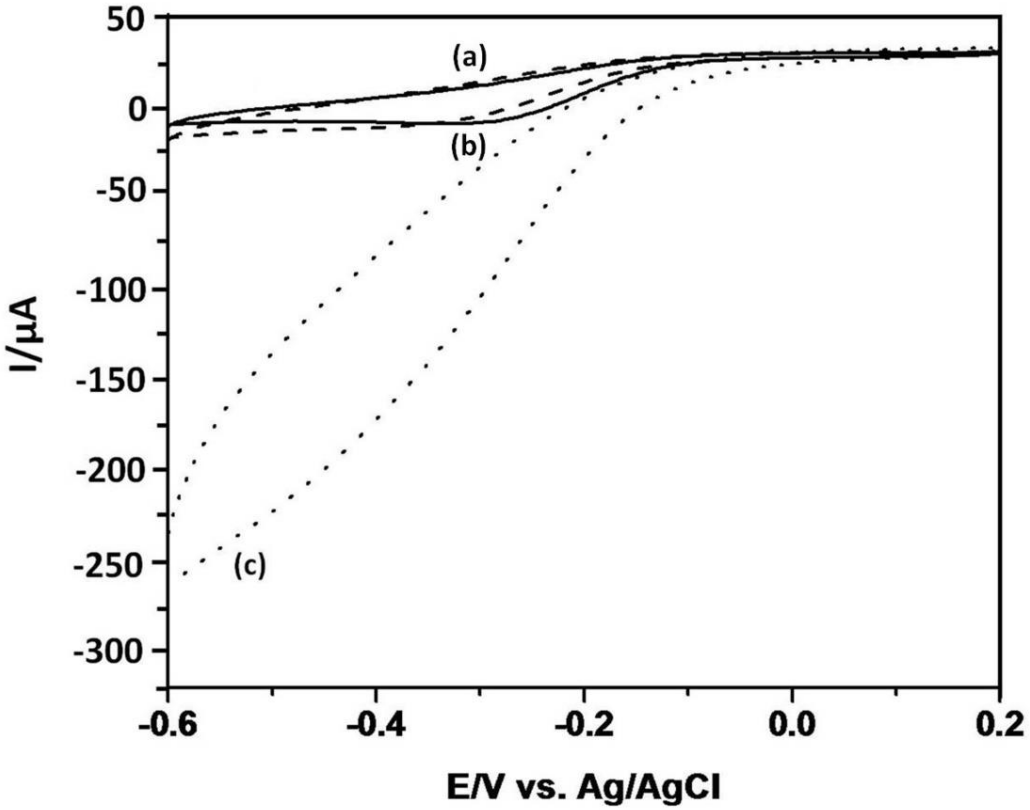

Figure 4.5 Cyclic voltammograms of HRP/BCNTs/Chi composite film in 0.1 M PBS (pH=7.0) at $0.1 Vs^{-1}$ with different amount of H_2O_2 (a) without H_2O_2 (dash), (b) 0.2 mM (solid), and (c) 1.0 mM (dot).

Cyclic voltammetry was used to study the electrocatalytic behavior of HRP/BCNTs/Chi composite film toward hydrogen peroxide (H_2O_2). Fig. 4.5 shows the CV of the HRP/BCNTs/Chi modified electrode in the absence and presence of hydrogen peroxide in 0.1M N_2-saturated PBS (pH 7.0) at a scan rate of 0.1 Vs^{-1}. It can be seen that upon addition of H_2O_2, the cathodic response was remarkably enhanced. With amount of H_2O_2 increasing, the reduction peak currents increased and

peak potential shifted negatively (curves b and c), indicating a typical electrocatalytic reduction process of H_2O_2, and that HRP/BCNTs/Chi nanocomposite film kept its bioelectrocatalytic activity. The electrocatalytic reduction mechanism of HRP towards H_2O_2 can be presented as follows [46]:

$$\text{HRP-Fe (III)} + H_2O_2 \rightarrow \text{Compound I} + H_2O \quad (1)$$

$$\text{Compound I} + e^- \rightarrow \text{Compound II} \quad (2)$$

$$\text{Compound II} + e^- \rightarrow \text{HRP-Fe (III)} \quad (3)$$

HRP reacts with H_2O_2 to form the first intermediate (Compound I), which contains a ferryl iron weakly spin-coupled to a porphyrin π-cation radical. Compound I obtained one electron from the electrode and was reduced to the second intermediate (Compound II), which was reduced to the HRP by accepting another electron from electrode. Therefore, the reduction current increases with increasing concentration of H_2O_2. The above results indicate that electrocatalytic reduction of H_2O_2 was performed on the sensor and was achieved by HRP immobilized in the BCNTs/Chi composite film [24]. The BCNTs/Chi film not only facilitated the direct electron transfer between enzyme and electrode but also provided a favorable microenvironment around enzyme to keep its good electrocatalytic bioactivity. This may be mostly attributed due to the presence of many defective and active sites on the BCNTs surface.

4.4 Conclusions

The bamboo shaped carbon nanotube/chitosan film was prepared and used for the immobilization of HRP and its bioelectrochemical studies. The direct electrochemistry and electrocatalysis of HRP on the film have been investigated. The results indicated that the immobilized HRP onto the film retains its good bioelectrocatalytic activity to H_2O_2. The defective sites and active sites on the BCNTs surface induced by nitrogen doping could help to promote the direct electron transfer

between enzyme and electrode. Therefore, it provides a vast array of new opportunities to use BCNTs as building units for bioelectrochemical and biomedical applications.

Acknowledgement

The authors greatly acknowledge the support from National Science Foundation (EEC-0823974 and CMMI-1030289).

References

[1] M. EI Kaoutit, I. Naranjo-Rodriguez, K.R. Temsamani, M. Domínguez, J.L.H. Cisneros, Talanta 75 (2008) 1348-1355.

[2] Z.J. Wang, M.Y. Li, P.P. Su, Y.J. Zhang, Y.F. Shen, D.X. Han, A. Ivaska, et al., Electrochem.Commun. 10 (2008) 306-310.

[3] Y.D. Zhao,W.D. Zhang, H. Chen, Q.M. Luo, S. Fong Yau Li, Sens. Actuators B 87 (2002) 168-172

[4] J.J. Gooding, R. Wibowo, J.Q. Liu,W.R. Yang, D. Losic, S. Orbons, F.J. Mearns, et al., J. Am. Chem. Soc. 125 (2003) 9006-9007.

[5] E.E. Ferapontova, Electroanalysis 16 (2004) 1101-1112.

[6] H.J. Chen, S.J. Dong, Biosens. Bioelectron. 22 (2007) 1811-1815.

[7] S.F.Wang, F. Xie, G.D. Liu, Talanta 77 (2009) 1343-1350.

[8] W.Y. Cai, Q. Xu, X.N. Zhao, J.J. Zhu, H.Y. Chen, Chem. Mater. 18 (2006) 279-284.

[9] R. Andreu, E.E. Ferapontova, L. Gorton, J.J. Calvente, J. Phys. Chem. B 111 (2007) 469-477

[10] F.A. Armstrong, J. Chem. Soc. J. Chem. Soc., Dalton Trans., 2002, 661-671.

[11] J.F. Rusling, Acc. Chem. Res. 31 (1998) 363-369;

[12] W.J. Zhang, Y.X. Huang, H. Dai, X.Y. Wang, C.H. Fan, G.X. Li, Anal. Biochem. 329

(2004) 85-90.

[13] C.J. Zhong, J. Luo, B. Fang, B. Wanjala, P. Njoki, R. Loukrakpam, J. Yin, Nanotechnology 21 (2010) 062001.

[14] J. Lu, I. Do, L. T. Drzal, R. M. Worden, I. Lee, ACS Nano. 2 (2008) 1825-1832.

[15] Z. Wang, Z.Z. Zhu, J. Shi, H. L. Li, Appl. Surf. Sci. 253 (2007) 8811-8817

[16] Z.Z. Zhu, Z.Wang, H.L. Li, J. Power Sources 186 (2009) 339-343.

[17] S. W. Hong, T. Banks, J. A. Rogers, Adv. Mater. 22 (2010) 1-5.

[18] Z. Chen, D. Higgins, Z. W. Chen, Electrochimi. Acta. 55 (2010) 4799-4804.

[19] M. T. Pettes, L. Shi, Adv. Funct. Mater. 19 (2009) 3918-3925.

[20] N. Alexeyeva, J. Kozlova, V. Sammelselg, P. Ritslaid, H. Mandar, K. Tammeveski, Appl. Surf. Sci. 256 (2010) 3040-3046.

[21] B P. Grady, Macromol. Rapid Commun. 31 (2010) 247-257.

[22] L.F. Dong, Nanotechnology 20 (2009) 465602-465607.

[23] X.H, Zhong, Y.L. Li, Y.K. Liu, X.H. Qiao, Y. Feng, J. Liang, J. Jin, et al., Adv. Mater. 22 (2010) 692-696.

[24] J.L. Huang, Y.C. Tsai, Sens Actuators B Chem. 140 (2009) 267-272.

[25] J.P. Lei, H.X. Ju, WIREs: Nanomed. Nanobiotechnol. 2 (2010) 496-509.

[26] Z. Liu, S. Tabakman, K. Welsher, H.J. Dai, Nano Res. 2 (2009) 85-120.

[27] Y.F. Tang, B.L. Allen, D.R. Kauffman, A. Star, J. Am. Chem. Soc. 131 (2009) 13200-13201.

[28] K.P. Gong, F. Du, Z.H. Xia, M. Durstock, L.M. Dai, Science 323 (2009) 760-764.

[29] J.P. Dong, X.M. Qu, L.J. Wang, C.J. Zhao, J.Q. Xu, Electroanalysis 20 (2008) 1981-1986.

[30] Z.Z. Zhu, J.L. Wang, A. Munir, H.S. Zhou, Electrochimi. Acta. 55 (2010) 8517-8520.

[31] R.M. Yadav, P.S. Dobal, T. Shripathi, R.S. Katiyar, O.N. Srivastava, Nanoscale Res. Lett. 4 (2009) 197-203.

[32] Z.Y. Juang, J.F. Lai, C.H. Weng, J.H. Lee, H.J. Laic, T.S. Lai, C.H. Tsai, Diam. Relat. Mater. 13 (2004) 2140-2146.

[33] X. Xu, S.J. Jiang, Z. Hu, S. Q. Liu, ACS Nano 4 (2010) 4292-4298.

[34] Q.H. Yang, P.X. Hou, M. Unno, S. Yamauchi, R. Saito, T. Kyotani, Nano Lett. 5 (2005) 2465-2469.

[35] Y. Okamoto, Chem. Phys. Lett. 420 (2006) 382-386.

[36] L. Gan, R. Lv, H.D. Du, B.H. Li , F.Y. Kang, Carbon 47 (2009) 1833-1840.

[37] N.Q. Jia, L.J. Wang, L. Liu, Q. Zhou, Z.Y. Jiang, Electrochem.Commun. 7 (2005) 349-354.

[38] N.Q. Jia, L. Liu, Q. Zhou, L.J. Wang, M.M. Yan, Z.Y. Jiang, Electrochimi. Acta. 51 (2005) 611-618.

[39] M. Zhang, A. Smith, W. Gorski, Anal. Chem. 76 (2004) 5045-5050.

[40]Y. Liu, X.H. Qu, H.W. Guo, H.J. Chen, B.F. Liu, S.J. Dong. Biosens. Bioelectron. 21 (2006) 2195-2201.

[41] C.N. He, N.Q. Zhao, C.S. Shi, X.W. Du, J.J. Li, J. Alloy. Compd. 433 (2007) 79-83.

[42] X.H. Kang, J. Wang, Z. W. Tang, H. Wu, Y.H. Lin, Talanta, 78 (2009) 120-125.

[43] K. Honda, M. Yoshimura, T.N. Rao, D.A. Tryk, A. Fujishima, J. Electroanal. Chem. 514 (2001) 35-50.

[44] E. Laviron, J. Electroanal. Chem. 101 (1979) 19-28.

[45] Y.D. Zhao, W.D. Zhang, H. Chen, Q.M. Luo, S. Fong, Y. Li, Sens. Actuators B 87 (2002) 168-172.

[46] L. Qian, X.R. Yang, Talanta 68 (2006) 721-727.

Chapter 5 A novel non-enzymatic glucose biosensor based on CuO nanoparticle decorated TiO_2 nanotube arrays

Abstract

A simple, inexpensive and well performing non-enzymatic electrochemical glucose biosensor by using CuO nanoparticle decorated TiO_2 nanotube array electrode was developed. The proposed electrode produced a high sensitivity of 239.9 μA mM^{-1} cm^{-2} and a low detection limit of 0.78 μM (S/N=3). Besides these attractive analytical features, the fabricated sensor presented long-term stability, good reproducibility and excellent selectivity.

5.1 Introduction

Glucose biosensors have raised considerable interest in past few decades due to the importance of glucose monitoring in blood diagnosis, food industries, bio-processing and biofuel cells [1]. The majorities of the current glucose biosensors are electrochemical enzymetic glucose biosensors, which based on glucose oxidase (GOx) bound to electrode transducers, have been intensively studied and are the most common devices commercially available as well [2, 3]. The enzymetic glucose biosensors exhibit high sensitivity and excellent selectivity but their performance is impacted by the intrinsic nature of enzymes [4]. Environmental conditions such as pH, temperature, chemicals, humidity can easily influence the activity of the enzyme. In order to deal with these disadvantageous limitations, non-enzymatic glucose biosensors have been proposed by many researchers [1]. However, most of non-enzymatic glucose biosensors show poor selectivity, therefore, tremendous efforts have been devoted to the development of electrocatalysts with high sensitivity and selectivity. Different transition metals (Pt [5], Au [6], Ag [7], Ni [8], Cu [9]) and metal oxides (NiO [10], CuO [11], CoO [12]) have been explored as electrocatalysts for glucose oxidation. Among them, copper oxide (CuO) is one of the most extensively studied catalysts for non-enzymatic biosensors due to its properties of low cost, non-toxic, outstanding redox behavior and easy to produce, different nanostructures of CuO have been utilized for the detection of glucose [13]. The most accepted mechanism for the oxidation of glucose on the CuO nanomaterial modified electrode in an alkaline medium is as follows. During the electrochemical measurement, Cu (II) on the CuO modified electrode was first oxidized to Cu (III). The produced oxidative Cu (III) catalyzed glucose to generate gluconolactone and then gluconolactone is further oxidized to glucose acid [14].

On the other hand, titanium dioxide (TiO_2), known as titania, is the most extensively studied

transition-metal oxides in material science. TiO_2 nanotubes are vertically aligned on the underlying Ti substrate and have been explored as a promising nano sized electrode candidate for electrochemical biosensors. Besides large surface area, highly ordered one dimensional, one-end open tubular structure and good biocompatibility, TiO_2 nanotubes offers following additional benefits: 1) Structure and morphology control of the tubes during the synthesis provides possibilities for the different designs of electrode; 2) Vertically aligned nanotube arrays facilitate more rapid electron transfer compared to randomly distributed nanotubes due to the directly transfer of electrons along the vertical direction of the tubes; 3) Strong adhesions between TiO_2 nanotubes and Ti substrate avoid the loss in electrochemical activity in the long term practical operations; 4) The structure of TiO_2 nanotube/Ti forms an n-type semiconductor/metal Schotty-type contact, which would enhance the rapid transport of surface reaction electrons to the metal surface [15, 16]. Herein, we proposed a non-enzymatic glucose biosensor based on CuO nanoparticle (CuO NP) coated TiO_2 nanotube (CuO/TiO_2 nanotube) electrode. As presented in Scheme 5.1, well-aligned and highly ordered TiO_2 nanotube arrays on a Ti substrate were fabricated by electrochemical anodization. Then, CuO nanoparticles were deposited onto TiO_2 nanotube arrays through a two-step electro-deposition method. Further, the applicability of CuO NPs as active electrocatalysts towards the oxidation of glucose was demonstrated. The proposed CuO/TiO_2 nanotube electrode exhibited a low detection limit with an ideal selectivity and stability, which indicated that the proposed electrode could serve as a promising probe for enhancing nonenzymatic glucose sensing.

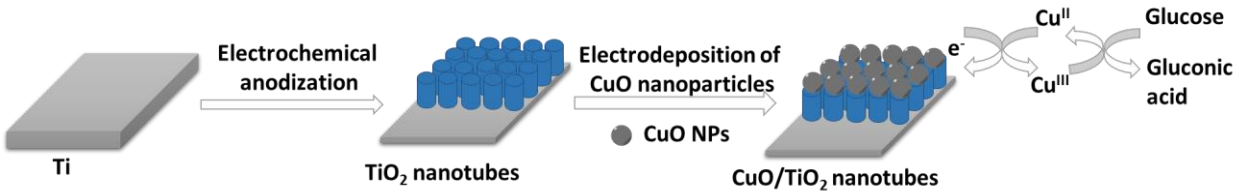

Scheme 5.1 Schematic representation of the non-enzymatic glucose biosensor based on CuO nanoparticle decorated TiO_2 nanotube arrays and its sensing mechanism.

5.2 Experimental

5.2.1 Preparation of the TiO_2 nanotube array

A sheet of titanium (99.7% trace metals basis, Aldrich) was cut into several small foils with the size of 2.5 cm by 2 cm. Then foils were polished manually with sandpaper (220-400-800 assorted grit, 3M Wetordry) for 30 minutes and cleaned sequentially with methanol, acetone, ethanol, and deionized water (DI water) using an ultrasonic cleaner for 15 minutes each. After that, 5 mL of DI water, 15 mL of 70% HNO_3 acid and 5 mL of 50% HF acid was mixed to make 25 mL of HF/HNO_3 mixed acid (1:3:1 ratio in volume). The cleaned titanium foils were then immersed into the mixed acid for 15 seconds and rinsed by DI water.

3.351 g of NH_4F solid was dissolved in 270 mL of ethylene glycol and 30 mL of DI water (1 wt% NH_4F in ethylene glycol electrolyte containing 10 vol% of water) to make the electrolyte solution for anodization. A piece of cleaned Ti foil and a platinum mesh (1.5cm × 2cm) were carefully immersed in parallel into the electrolyte to form a two electrodes electrochemical cell and connected to a direct current (DC) power supply station (DCS80-13E, Sorensen). Ti foil was anodized under different pairs of voltages and times under stirring (reaction area: 1.5cm × 1.5cm). The attempted voltage range was between 20 V and 30 V, and anodizing time varied from 20 to

100 minutes. The anodized foils were rinsed with DI water. Finally, the final foils were annealed at 350 ºC for 1.5 hours and then cooled naturally to room temperature.

5.2.2 Preparation of the CuO/TiO_2 nanotube electrode

CuO NPs were deposited onto the TiO_2 nanotube array electrode through a two-step electrodeposition method [17]. A constant potential of -0.4 V was first applied to the TiO_2 nanotube in a solution of 0.5 M $CuSO_4$ + 0.5 M H_2SO_4 for 100 s to deposit Cu first. Then, the electrode was scanned in 0.1 M NaOH with cyclic voltammetry (CV) under the potential range of -0.5 to 0.3 V at 100 mV s^{-1} for 10 cycles to allow the oxidization of Cu to CuO nanoparticles.

5.2.3 Measurements

Scanning electron microscopy (SEM, JEOL, JSM-7000F) operating at 10 kV was applied to characterize the morphology of the prepared sampleas. Energy dispersive spectroscopy (EDS) spectrum analysis was carried out on the same SEM. Structural analysis of the as-prepared TiO_2 nanotube arrays and CuO/TiO_2 nanotube arrays was investigated by X–ray diffraction (XRD, Bruker-AXS D8 focus, 40 kV, 40 mM, Cu Ka radiation). All electrochemical measurements were carried out using an Autolab PGSTAT12 electrochemical workstation (Metrohm, USA Inc.). A conventional cell with a three-electrode configuration will be used throughout this work. The working electrode is as prepared TiO_2 nanotube array. A platinum mesh and an Ag/AgCl (saturated KCl) were used as the counter electrode and the reference electrode, respectively. All the electrolytes were deaerated by bubbling nitrogen gas for 30 min before the experimental procedure. All the experiments were carried out at room temperature.

5.3 Results and discussion

5.3.1 Characterization of the TiO_2 nanotube array and CuO/TiO_2 nanotube array

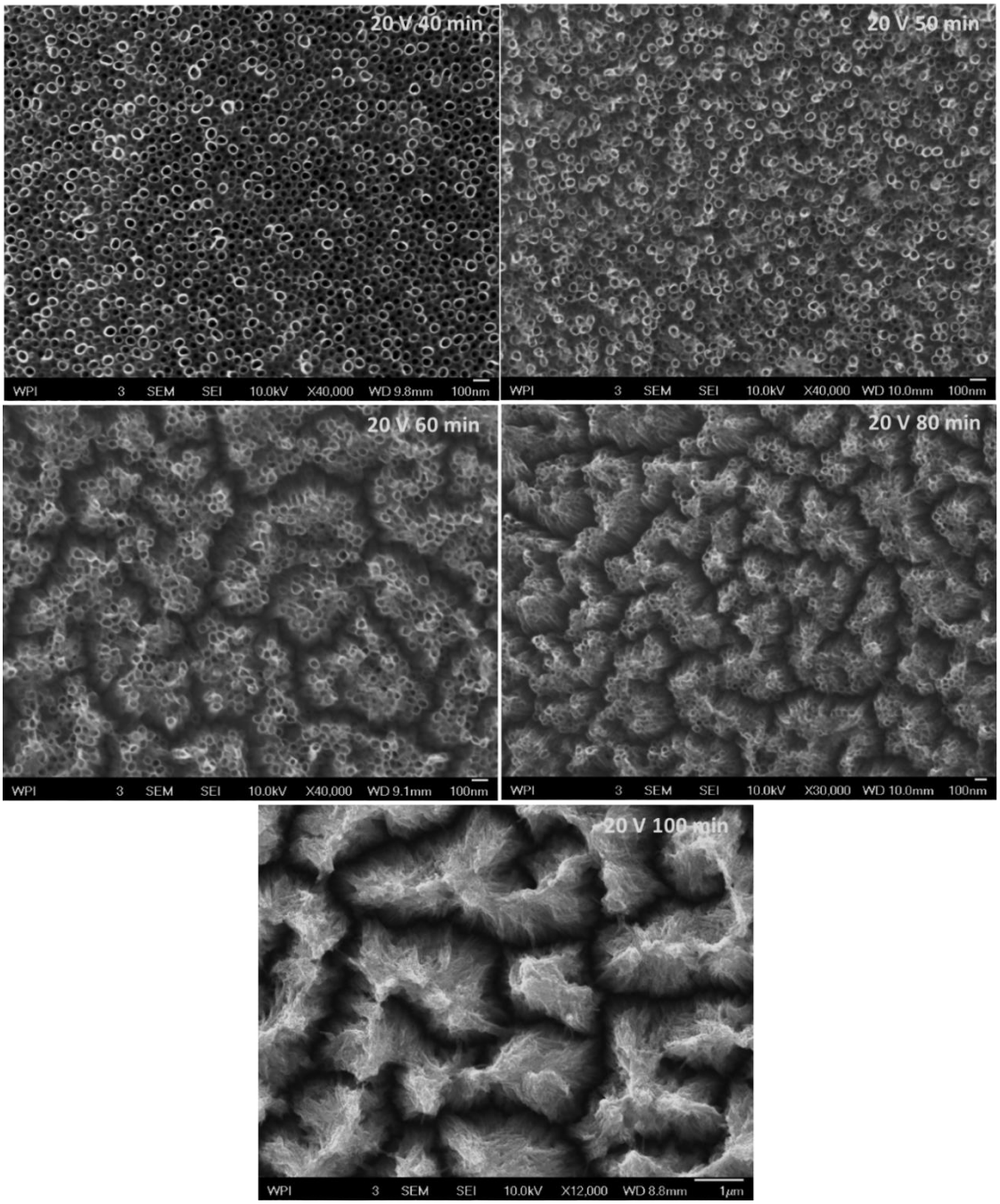

Figure 5.1 SEM images of TiO_2 nanotube synthesized at 20 V with anodizing time from 40 min to 100 min.

The morphology of TiO_2 nanotubes synthsized at 20 V with different anodizing time was characterized with SEM and shown in Fig. 5.1. It can be observed that the nanotubes prepared for 40 min are uniform and highly ordered with a diameter of ~60 nm. When the anodizing time increased to 50 min, the nanotubes started to form bundling at their tips. Along with increasing anodizing time to 100 min, the formation of needle-like morphologies was observed on the tips of nanotubes. This phenomenon can be explained based on the mechanism of the synthesis of TiO_2 nanotubes by electrochemical anodization. As we mentioned, there are two competitive reactions during the growth of the nanotubes: the formation the oxide layer and the dissolution of the nanotube layer. In long duration anodization process, the dissolution of the nanotube layer leads to the thinning of the tube walls. When the walls become too thin to support the vertical growth of nanotubes, bundling or collapsing will occur at the tube tips.

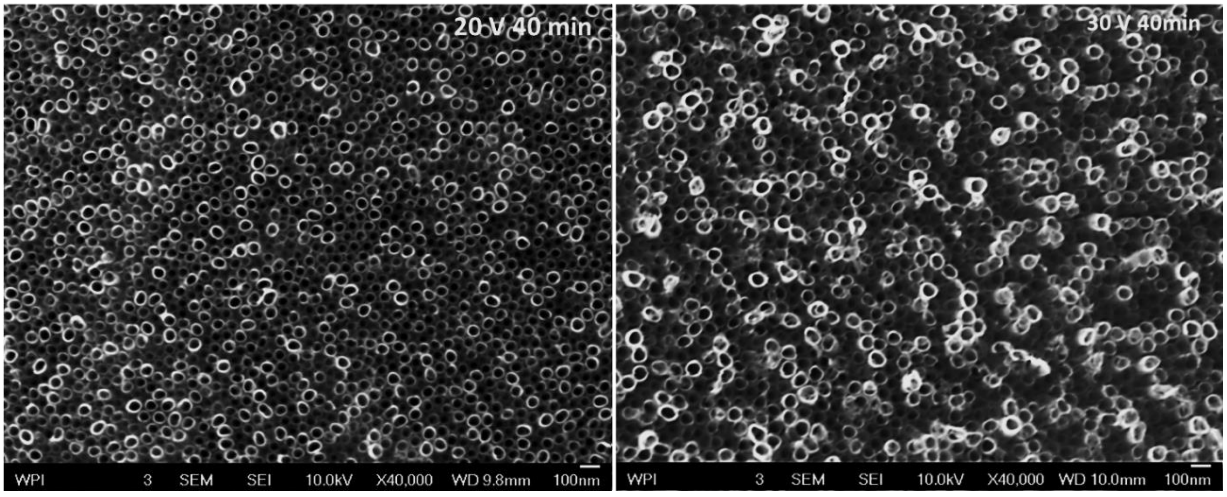

Figure 5.2 SEM images of TiO_2 nanotube synthesized at 20 V and 30 V for 40 min.

The comparison of TiO_2 nanotubes prepared under different voltages was demonstrated in Fig. 5.2. Relative larger diameter was found for the nanotubes synthesized at 30 V compared to at 20 V, which may due to the bigger initial pits formed at higher voltage.

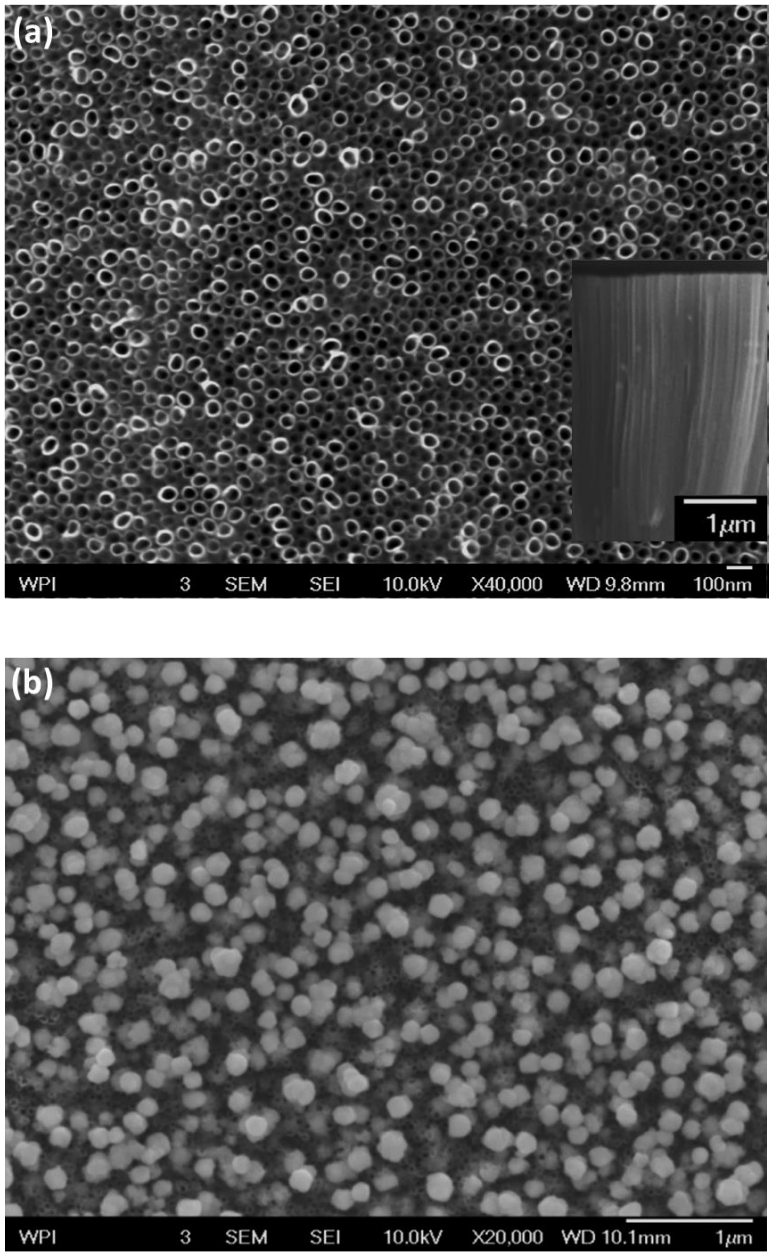

Figure 5.3 SEM images of (a) TiO_2 nanotube and (b) CuO nanoparticle coated TiO_2 nanotubes, inset is the cross sectional view of the nanotubes.

The morphology of TiO_2 nanotubes synthesized at 20 V and CuO/TiO_2 nanotubes was characterized with SEM and presented in Fig. 5.3a and b. The cross sectional view of the nanotubes

reveled that prepared nanotubes showed a length of ~3.5 µm (Fig. 5.3a). The SEM image of CuO/TiO_2 nanotubes clearly illustrated that CuO nanoparticles with an average diameter of ~ 120 nm were well dispersed on the nanotubes (Fig.5.3b). The presence of Ti, O and Cu is confirmed with EDS as shown in Fig. 5.4.

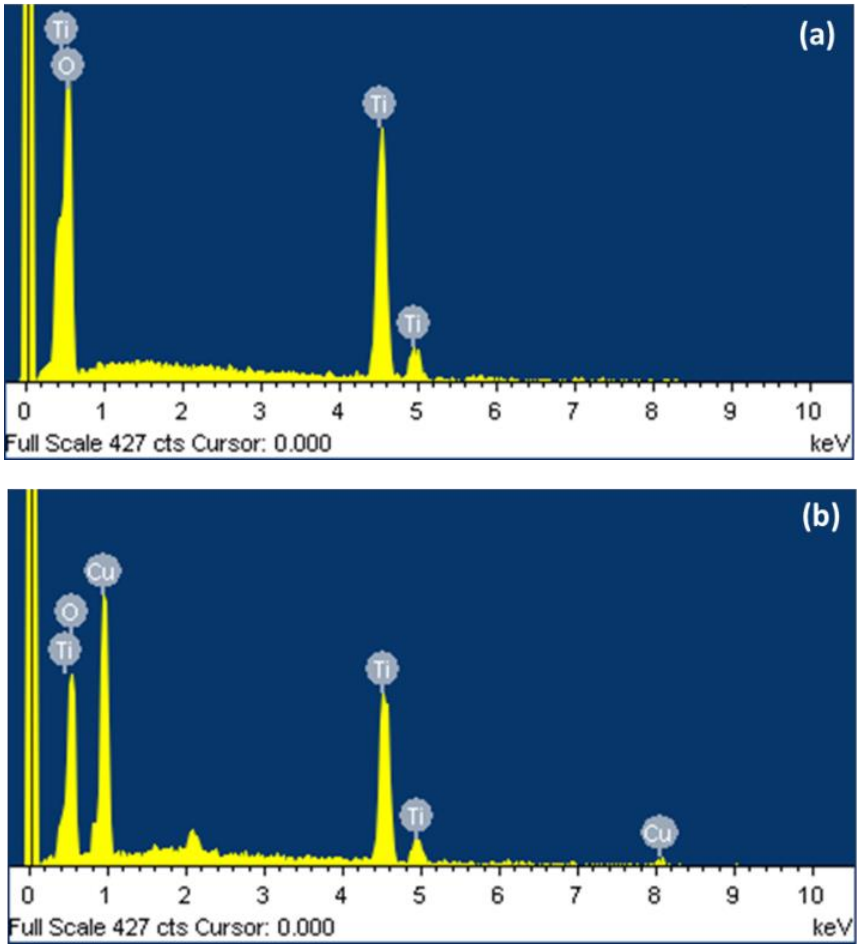

Figure 5.4 EDS of (a) TiO_2 nanotubes and (b) CuO nanoparticle coated TiO_2 nanotubes.

The as prepared TiO_2 nanotubes and CuO/TiO_2 nanotubes were analyzed by XRD in this work (Fig. 5.5). The diffraction peaks marked A at 25.4° were observed in both TiO_2 nanotubes and CuO/TiO_2 nanotubes, which corresponded to the anatase phase of TiO_2 [18]. The XRD patterns of CuO/TiO_2 nanotubes provided further insight to the analysis of crystal structure of CuO

nanoparticles. All the peaks of CuO can be assignd to monoclinic CuO [19, 20], indicating the formation of a pure phase CuO.

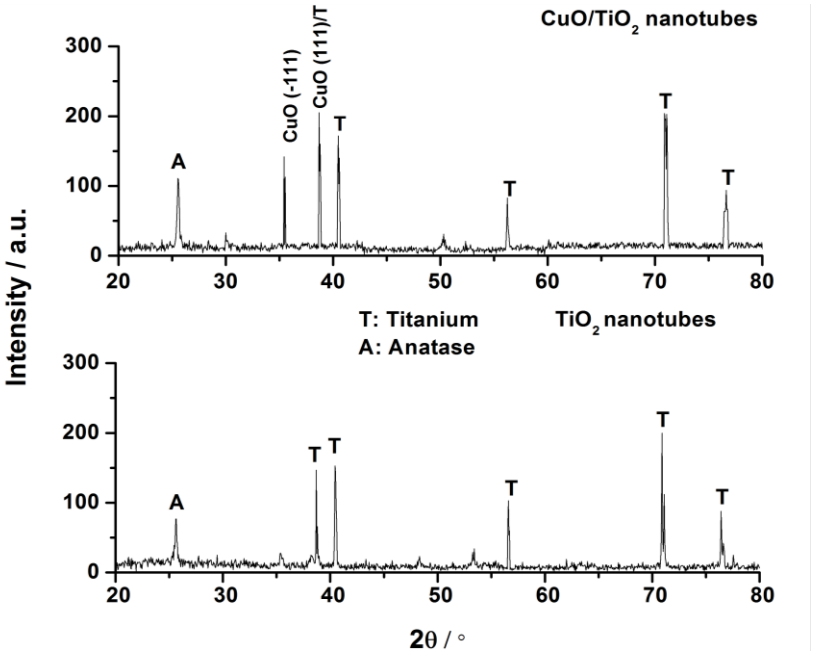

Figure 5.5 XRD of TiO_2 nanotubes and CuO nanoparticle coated TiO_2 nanotubes.

5.3.2 Nonenzymatic glucose behavior at the CuO/TiO_2 nanotube electrode

In order to investigate the electrocatalytic activity of the prepared electrode towards the oxidation of glucose, CV results of the TiO_2 nanotube arrays and CuO/TiO_2 nanotube arrays in the absence and presence of 1.0 mM glucose in 0.1 M NaOH at 100 mV s^{-1} was shown in Fig. 5.6. A broad reduction peak with a peak potential of about +0.68 V was observed at the CuO/TiO_2 nanotube electrode before the injection of glucose (curve c), which corresponded to a Cu(II)/Cu(III) redox couple [21]. After the addition of glucose, an oxidative peak at about +0.55 V appeared for the CuO/TiO_2 nanotube electrode (curve d). In this process, electrons transferred from glucose to the electrode surface because Cu(III) acted as an electron transfer mediator, which leaded to the irreversible oxidation of glucose [21]. The whole reaction process can be written as [22]:

$$CuO + OH^- \rightarrow CuOOH + e^-$$

$$2CuOOH + glucose \rightarrow 2CuO + gluconolactone + H_2O$$

$$gluconolactone \rightarrow gluconic\ acid\ (hydrolysis)$$

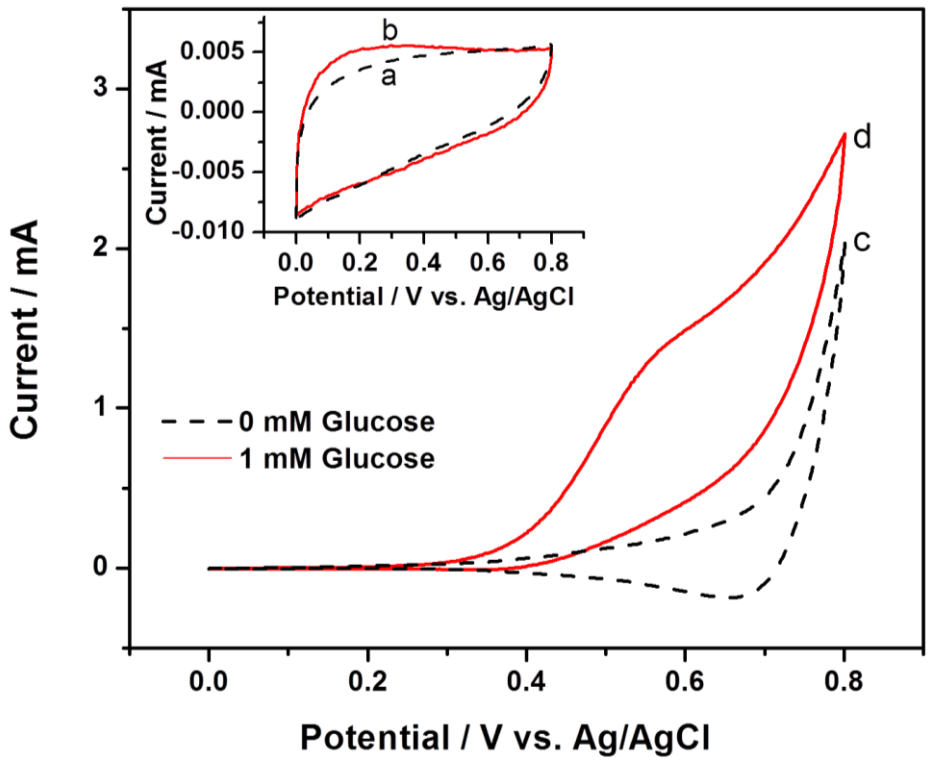

Figure 5.6 CVs of CuO/TiO_2 nanotube arrays in the absence (black dash) and presence (red solid) of 1.0 mM glucose in 0.1 M NaOH at 100 mV s^{-1}, inset is the CVs of bare TiO_2 nanotube in the absence (black dash) and presence (red solid) of 1.0 mM glucose in 0.1 M NaOH at 100 mV s^{-1}.

The effect of the TiO_2 nanotube electrode in the electrocatalytic process of glucose was studied as well (Fig. 5.6, inset). From the CV results, a slight increase in current was observed for the electrode in the present of glucose (curve b) compared to in the absence of glucose (curve a), which might because of the glucose degradation at the TiO_2 nanotube surface [23].

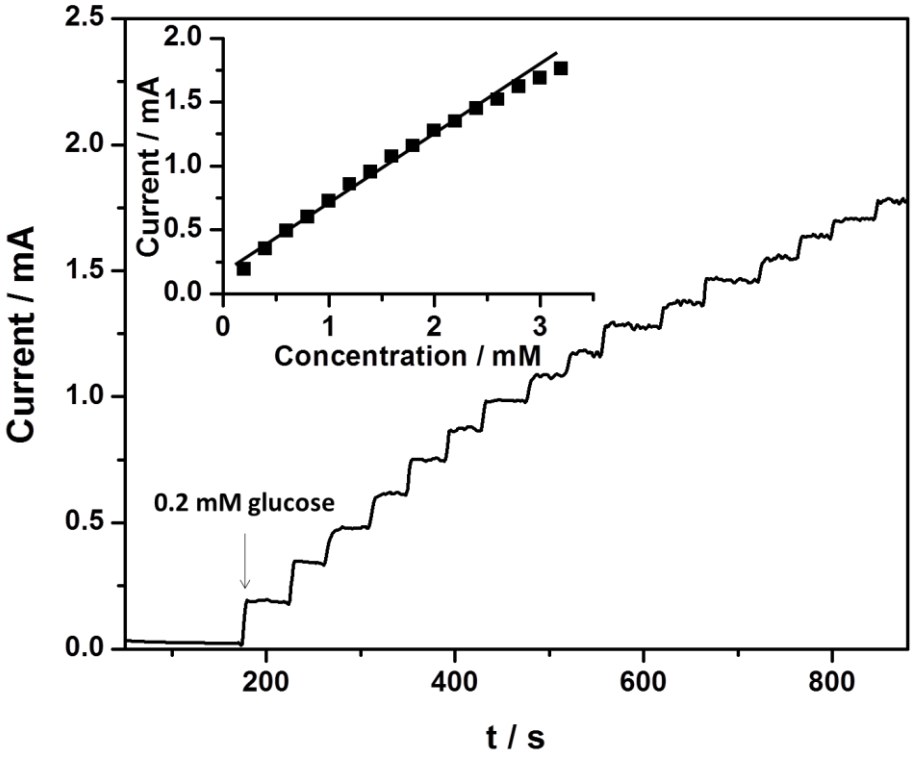

Figure 5.7 Amperometric response at CuO/TiO_2 nanotube electrode with successive addition of 0.2 mM glucose in 0.1 M NaOH at +0.55 V (vs. Ag/AgCl). Inset: The calibration curves of current versus glucose concentration.

The amperometric response of the as-prepared CuO nanoparticle decorated TiO_2 nanotube electrode to glucose was performed to evaluate the sensitivity of the proposed biosensor. The current changes of the electrode with successive addition of 0.2 mM glucose in 0.1 M NaOH solution at +0.55 V (vs. Ag/AgCl) was recorded and demonstrated in Fig. 5.7. When the glucose was injected into the electrolyte, the current markedly increased to reach steady-state within a few seconds. The corresponding calibration curve of the proposed glucose sensor based on the amperometric results was plotted and presented as inset in Fig. 5.7. The current on the proposed electrode showed a linear response to glucose concentrations up to 3.2 mM with a linear regression equation of I (mM) = 0.1620 + 0.5398 C (mA) (correlation coefficient r^2= 0.99196). According to IUPAC (International Union of Pure and Applied Chemistry) definitions, the limit of detection

(LOD) is calculated as: LOD = 3σ/S, where 3 is the noise to signal ratio (S/N), σ is the standard deviation of ten blank signals, and S is the slope of the calibration curve [24]. Thus, a high sensitivity of 239.9 μA mM^{-1} cm^{-2} and a low LOD of 0.78 μM was achieved for the proposed the CuO/ TiO_2 nanotube array electrode respectively.

Table 5.1 Comparison of analytical performance of the prepared CuO/TiO_2 nanotube biosensor with other published glucose biosensors.

Electrode	Potential	Sensitivity (μM mM^{-1} cm^{-2})	Detection limit	Linear range	Reference
GOx/TiO_2 NT array	-0.35 V (vs. Ag/AgCl)	56.7	5 μM	0.4-3.6 mM	25
CuO nanofiber/ TiO_2 NT array	0.50 V(vs. SCE)	79.79	1 μM	Up to 2 mM	26
CuO nanoplate/ TiO_2 NT/FTO glass	0.7 V (vs. Ag/AgCl)	1321	0.39 μM	10 μM-2 mM	27
CuO nanoparticle/GCE	+0.6 V (vs. Ag/AgCl)	404.53	1 μM	Up to 2.55 mM	28
CuO nanoparticle/ TiO_2 NT array	+0.55 V (vs. Ag/AgCl)	239.9	0.78 μM	Up to 3.2 mM	This work

NT: nantoube; FTO: fluorine-doped tin oxide; SCE: saturated calomel electrode; GCE: glassy carbon electrode.

Compared with other CuO nanostructures and GOx based electrochemical sensors for glucose detection (Table 5.1), the sensitivity of the prepared biosensor is higher than that of GOx [25] and CuO nanofiber [26] modified TiO_2 nanotube array, but lower than that of CuO nanoplate/TiO_2 NT/FTO glass [27] and CuO nanoparticle/GCE [28]. The linear range and detection limit are superior to most of them. The high sensitivity and low detection limit of the proposed biosensor mainly due to two aspects: the well-dispersed CuO nanoparticles and structural features of TiO_2 nanotube array as electrode. Furthermore, this sensor has the potential to be used for the detection of glucose in other biological fluids (urine, saliva, and tear) where glucose level is much lower than in blood [29].

Stability and reproducibility of biosensors are key factors in practical applications. The prepared electrode was stored at room temperature in air for four weeks. The amperometric response showed the prepared electrode could retain around 95% of its initial response, indicating good stability. The relative standard deviation (RSD) was found to be 2.76%, confirming a good reproducibility.

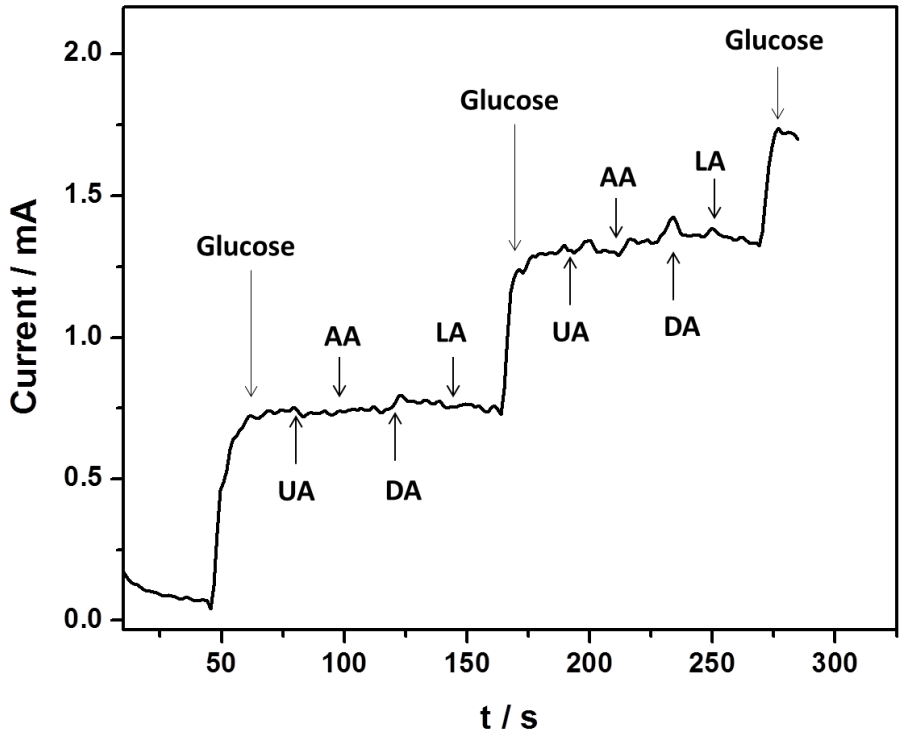

Figure 5.8 Continuous amperometric response at CuO/TiO_2 nanotube electrode with successive injection of 1.0 mM glucose, 0.1 mM UA, AA, DA and 1.0 mM LA into 0.1 M NaOH at +0.55 V (vs. Ag/AgCl).

The selectivity of the proposed glucose biosensor was studied and the results were shown in Fig. 5.8. Several possible interfering biomolecules, such as uric acid (UA), ascorbic acid (AA), dopamine (DA) and lactate (LA) usually co-exist with glucose in human fluids (e.g. urine, serum and blood) were examined. Considering that the concentration of glucose is at least 30 times of

UA, AA, DA [22] and 2-3 times of LA [30], the interference experiment was carried out by successive injection of 1.0 mM glucose, 0.1 mM UA, AA, DA and 1.0 mM LA into 0.1 M NaOH solution. The results indicated the interferents did not cause significant current changes, which means that the CuO/TiO_2 nanotube electrode exhibited excellent selectivity towards glucose determination.

5.4 Conclusions

In summary, we have successfully synthesized well-aligned TiO_2 nanotube arrays on a Ti substrate by electrochemical anodization. Highly uniform CuO nanoparticles were electrodeposited onto TiO_2 nanotube arrays through a two-step method. As-prepared CuO/TiO_2 nanotube arrays were utilized to fabricate a new nonenzymatic glucose biosensor. The results demonstrate that this sensor showed a low detection limit of 0.78 μM with high sensitivity, good stability, reproducibility, selectivity and fast response time, suggesting its potential to be developed as a low-cost nano-biosensor for glucose measurements in human fluids.

Acknowledgment

This work was supported by National Science Foundation (CMMI-1030289).

References

[1] K.E. Toghill, R.G. Compton, Int. J. Electrochem. Sci. 5 (2010) 1246-1301.

[2] L.C. Clark, C. Lyons, Ann. N. Y. Acad. Sci. 102 (1962) 29-45.

[3] J. Wang, Chem. Rev. 108 (2008) 814-825.

[4] N.J. Ronkainen, H.B. Halsall, W.R. Heineman, Chem. Soc. Rev. 39 (2010) 1747-1763.

[5] S. Badhulika, R.K. Paul, R.T. Terse, A. Mulchandani, Electroanalysis 1 (2014) 103-108.

[6] S. Cherevko, C.H. Chung, Sens. Actuator B Chem. 142 (2009) 216-223.

[7] Y.Z. Liu, S. Liu, R.S. Chen, W.T. Zhan, H.W. Ni, F. Liang, Electroanalysis DOI: 10.1002/elan.201400568.

[8] R.M. Abdel Hameed, Biosens. Bioelectron. 47 (2013) 248-257.

[9] A.A. Ensafi, M.M. Abarghoui, B. Rezaei, Electrochim. Acta. 123 (2014) 219-226.

[10] P. Yang, X.L. Tong, G.Z. Wang, Z. Gao, X.Y. Guo, Y. Qin, ACS Appl. Mater. Interfaces 7 (2015) 4772-4777.

[11] R. Ahmad, M. Vaseem, N. Tripathy, Y.B. Hahn, Anal. Chem. 85 (2013) 10448-10454.

[12] C.W. Kung, C.Y. Lin, Y.H. Lai, R. Vittal, K.C. Ho, Biosens. Bioelectron. 27 (2011) 125-131.

[13] P. Si, Y.J. Huang, T.H. Wang, J.M. Ma, RSC Adv. 3 (2013) 3487-3502.

[14] S.D. Sun, X.Z. Zhang, Y.X. Sun, S.C. Yang, X.P. Song, Z.M. Yang, Phys. Chem. Chem. Phys. 15 (2013) 10904-10913.

[15] K. Lee, A. Mazare, and P. Schmuki, Chem. Rev. 114 (2014) 9385-9454.

[16] Q. Zhang, B. Zhou, J. Bai, L. Li, Z. Jin, J. Zhang, J. Li, et al., Adv. Mater. 20 (2008) 1044-1049.

[17] P.V. Suneesh, K. Chandhini, T. Ramachandran, B.G. Nair, T.G. Satheesh Babu, Biosens. Bioelectron. 50 (2013) 472-477.

[18] Y.K. Lai, Z.Q. Lin, J.Y. Huang, L. Sun, Z. Chen, C.J. Lin, New J. Chem. 34 (2010) 44-51.

[19] H.S. Xia, G.S. Yan, J. Mater. Chem. 22 (2012) 18664-18670.

[20] M.U. Anu Prathap, S.N. Sun, C. Wei, Z.C.J. Xu, Chem. Commun. 51 (2015) 4376-4379.

[21] S.T. Farrell, C.B. Breslin, Electrochim. Acta. 49 (2004) 4497-4503.

[22] L.Q. Luo, L.M. Zhu, Z.X. Wang, Bioelectrochemistry 88 (2012) 156-163.

[23] S.J. Yu, X. Peng, G.Z. Cao, M. Zhou, L. Qiao, J.Y. Yao, H.C. He, Electrochim. Acta 76 (2012) 512-517.

[24] J. Mocak, A.M. Bond, S. Mitchell, G. Scollary, Pure Appl. Chem. 69 (1997) 297-328.

[25] L.L. Zhang, L. Han, P. Hu, L. Wang, S.J. Dong, Chem. Commun. 49 (2013) 10480-10482.

[26] S. Luo, F. Su, C. Liu, J. Li, R. Liu, Y. Xiao, Y. Li, et al., Talanta 86 (2011) 157-163.

[27] J.S. Chen, L. Xu, R.A. Xing, J. Song, H.W. Song, D.L. Liu, J. Zhou, Electrochem. Commun. 20 (2012) 75-78.

[28] E. Reitz, W.Z. Jia, M. Gentile, Y. Wang, Y. Lei, Electroanalysis 20 (2008) 2482-2486.

[29] J. Zhang, W. Hodge, C. Hutnick, X.B. Wang, J. Diabetes Sci. Technol. 5 (2011) 166-172.

[30] B. Phypers, J.M. Tom Pierce, Contin. Educ. Anaesth. Crit. Care Pain 6 (2006) 128-132.

Chapter 6 Single domain antibody coated gold nanoparticles as enhancer for Clostridium difficile toxin detection by electrochemical impedance immunosensors*

Abstract

This work presents a sandwich-type electrochemical impedance immunosensor for detecting *Clostridium difficile* toxin A (TcdA) and toxin B (TcdB). Single domain antibody conjugated gold nanoparticles were applied to amplify the detection signal. Gold nanoparticles (Au NPs) were characterized by transmission electron microscopy and UV-vis spectra. The electron transfer resistance (Ret) of the working electrode surface was used as parameter in the measurement of the biosensor. With the increase of the concentration of toxins from 1pg/mL to 100 pg/mL, a linear relationship was observed between the relative electron transfer resistance and toxin concentration. In addition, the detection signal was enhanced due to the amplification effect. The limit of detection for TcdA and TcdB was found to be 0.61 pg/mL and 0.60 pg/mL respectively at a signal-to-noise ratio of 3 (S/N=3). This method is simple, quick turnaround, and ultrasensitive, thus possesses a great potential for clinical applications in the future.

This work has been published in Bioelectrochemistry 101 (2015) 153-158.

* This work is cooperated with Prof. Hanping Feng in Department of Microbial Pathogenesis in University of Maryland Dental School. All biological materials are obtained from his lab.

6.1 Introduction

Clostridium difficile is a spore-forming, gram-positive and anaerobic bacterium. It is the major cause of antibiotic-associated diarrhea and almost all cases of pseudomembranous colitis [1]. During the infection, two exotoxins with similar structure and function were released by most pathogenic strains of *C. difficile*: toxin A (TcdA) and toxin B (TcdB). Both TcdA and TcdB are cytotoxic, pro-inflammatory, and enterotoxic in human intestine [2]. They are primarily responsible for the diseases associated with the infection [3]. The incident of *C. difficile* infection (CDI) is increasing dramatically during the past few years, early diagnosis is essential for better control and management of CDI, therefore, much research has been focus on the rapid diagnosis and treatment of CDI in hospital settings [4-6]. The diagnosis of CDI is mainly based on clinical features and laboratory detection of *C. difficile* organisms and toxins [7]. Methods currently in use for the organism identification include stool culture, the detection of glutamate dehydrogenase (GDH), and polymerase chain reaction (PCR) [8]. The *C. difficile* toxin A&B detection assays are to detect the two toxins produced by *C. difficile* bacteria in a stool sample. There are two main assays: tissue culture assay [9, 10] and enzyme immunoassay (EIA) [11, 12]. A rapid and simple test with high sensitivity and specificity for detecting *C. difficile* toxins is still challenging but highly desirable.

In recent years, electrochemical biosensors have attracted considerable interest because of their intrinsic advantages such as high sensitivity, fast response, easy operation, favorable portability, and low cost [13]. Much effort has been made to design electrochemical biosensors with different technologies such as cyclic voltammetry (CV), chronoamperometry, chronopotentiomery, electrochemical impedance spectroscopy (EIS), and field-effect transistor (FET) [14]. Among these electrochemical methods, EIS is a rapid and non-destructive method with the ability to study

the interfacial behavior of a wide range of materials in electrochemical system [15, 16]. The electrode accessibility to the solution-based redox probe will be reduced due to the attachment of electrically insulated molecules, thus this technology is very useful to study the biorecognition event through capacitance, reactance and/or resistance changes at the electrode surface [17, 18]. The electrochemical impedance immunosensors combining EIS and immunoassay have attracted extensive interest in many areas, including food industry, environmental pollution, diagnosis, biotechnology, pharmaceutical chemistry, and clinical diagnostics [19-21]. Meanwhile, researchers found that analytical signals of electrochemical impedance biosensor can be amplified by various strategies including the use of biotin-avidin/streptavidin system [16, 22] and the generation of biocatalytic precipitation on the electrode surface [23].

On the other hand, it is worthy to note that with the increased understanding of nanomaterials, considerable efforts have been directed toward the design of different nanomaterial-based amplification paths aimed at achieving ultrahigh sensitivity [24-26]. For example, the application of semiconductor quantum dots (CdS) as oligonucleotide labeling tags for the detection of the target DNA by using EIS [27], which allows EIS signal be amplified by space resistance and negative charges provided by the nanoconjugates. As one of the most widely used nanomaterials in biomedical research and clinical imaging [28], gold nanoparticles (Au NPs) have been addressed as a promising nanomaterial for the signal amplification in EIS analysis because of their good biocompatibility and ease of self-assembly through a thiol group [29, 30]. It has been reported that the use of antibody modified gold nanoparticles are favorable to immobilize more antibody onto the electrode [31]. The sterical hindrance, as well as the increased amount of antibody generated by the presence of the antibody-gold conjugates can be used to enhance the sensitivity of

electrochemical impedance immunosensors [32, 33]. So far, there is no report on the application of electrochemical impedance immunosensors for detecting TcdA and TcdB.

Herein, we designed a simple sandwich-type electrochemical impedance immunosensor with antitoxin heavy-chain-only V_H (V_HH) antibodies [34] labeled gold nanoparticles as the amplifying probe for detecting both TcdA and TcdB. Heavy chain only antibody or single domain antibody (sdAb) was used in this work against both TcdA and TcdB. A primary single domain antibody ($sdAb_1$) was used to bond toxin onto the electrode and a secondary single domain antibody ($sdAb_2$) was applied to coat Au NPs to form the enhancer. Antibody coated gold nanoparticles can bring a large amount of antibody into the immunosensor system and results in an enhancement of electrochemical impedance signal. Thus this ultrasensitive EIS assay possesses a great potential for clinical applications in the future.

6.2 Experimental

6.2.1 Reagents

Gold (III) chloride trihydrate ($HAuCl_4 \cdot 3H_2O$) and Bovine serum albumin (BSA) were purchased from Sigma-Aldrich. Cystamine dihydrochloride ($C_4H_{12}N_2S_2$) was from Fluka. Sodium citrate dehydrate ($Na_3C_6H_5O_7 \cdot 2H_2O$) was obtained from Alfa Aesar. 1-ethyl-aminopropylcarbodiimide (EDC) and Nhydroxysuccinimide (NHS) were from Thermo Scientific. Recombinant TcdA and TcdB were purified from *Bacillus megaterium* as described previously [35]. Single domain V_HH antibodies (sdAbs) against TcdA and TcdB and their fusions specific to both toxins are described by us recently [34]. All other chemicals were of analytical grade and the water used in the experiment is deionized water. 0.1M PBS solution was prepared by mixing the stock solution of KH_2PO_4 and K_2HPO_4. All working solutions of toxin and antibody were prepared by dilution in the prepared PBS.

6.2.2 Determination of optimal $sdAb_2$ concentration for coating gold nanoparticles

Gold nanoparticles were synthesized by the classic citrate reduction method [36]. 100 mL of 1mM HAuCl4 solution were heated to boiling and refluxed while being constantly stirred. 10 mL of 38.8 mM sodium citrate solutions were added quickly under constant stirring. The color changed from yellow to clear, dark blue and then wine red in a few minutes, which indicating the formation of the Au NPs (Scheme 6.1). The solutions were refluxed for an additional 15 min, and cooled to room temperature. The final products were incubated at 4◦C for future use.

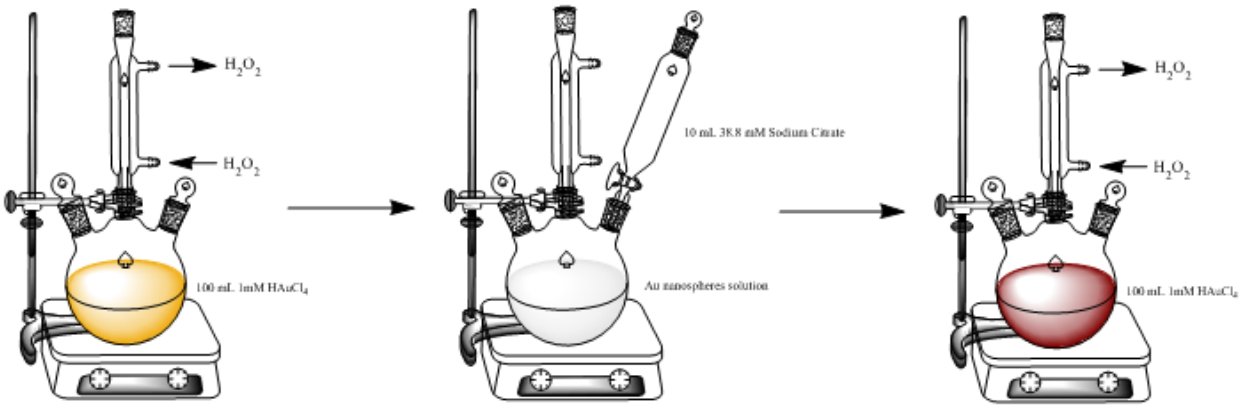

Scheme 6.1 Synthesis of Synthesis of citrate-capped gold nanoparticles

Conjugation of $sdAb_2$ to gold nanoparticles followed the method described by Slot & Geuze [37]. Briefly, 10 mL of Au NPs solutions were diluted with 70 mL water to give a total volume of 80mL as a stock liquid. To prepare an antibody-conjugated Au NPs, 10-50 µL $sdAb_2$ (0.07 µg/µL), in a total volume of 50 µL PBS buffer (pH =7.4), was added in 500 µL gold nanoparticles solution and incubated for 30 min at room temperature. Then 100 µL 10% NaCl solution was added, the color changed from red to purple can be observed for some of solutions. The minimum amount of $sdAb_2$ that did not have a color change was determined as the optimal amount for conjugation.

6.2.3 Preparation of $sdAb_2$-coated gold nanoparticles ($sdAb_2$-Au NPs)

The $sdAb_2$-Au NPs were prepared according to a documented method [38, 39] with some modifications. The optimal amount of $sdAb_2$ was mixed into 1 mL of Au NPs solution for 30 min at room temperature. Bovine serum albumin (BSA, 100 µL of 1%) was added to the mixture to block the remaining nonspecific adsorption-reactive sites. The suspension was then rinsed with a PBS solution (pH=7.4) containing 1% BSA by centrifugation for 3 times. The final precipitation was diluted to 1mL in PBS solution (pH=7.4) containing 1% BSA and kept at 4°C for further use.

6.2.4 Gold electrode cleaning

The gold electrode was polished with wet alumina power (0.1 and 0.03 µm respectively) and rinsed thoroughly with DI water. Then the polished electrode was successively cleaned ultrasonically in ethanol and DI water, followed by immersing in a piranha solution (3:1 concentrated sulfuric acid to 30% hydrogen peroxide) for 5 min and rinsed with DI water. After that, the electrode was electrochemically cleaned by performing cyclic voltammograms in 0.5 M H_2SO_4 between -0.3V and 1.5 V until the curve is stable.

6.2.5 Immunoassay procedure

A sandwich electrochemical impedance immunosensor was designed for the detection of TcdA and TcdB as shown in Scheme 6.2. The cleaned gold electrode was first placed into a 30mM cystamine dihydrochloride solution overnight and then rinsed with PBS solution to remove physically adsorbed dithiols. Subsequently, the cystamine self-assembled monolayers modified electrode was immersed into the $sdAb_1$ solution (0.045 µg/µL, EDC/NHS-activated) and allowed to react at 4°C for 2h. After sufficiently rinsing with PBS, the electrode was dipped in a 1% BSA solution for 30 min to block the remaining adsorption reactive sites.

After immobilized with primary antibody, the electrode was incubated in different concentration of TcdA/B solutions at 4°C for 3 hours and thoroughly rinsed with PBS. Then, the electrode was placed in the $sdAb_2$-Au NP solutions to amplify the response signal of impedance spectroscopy.

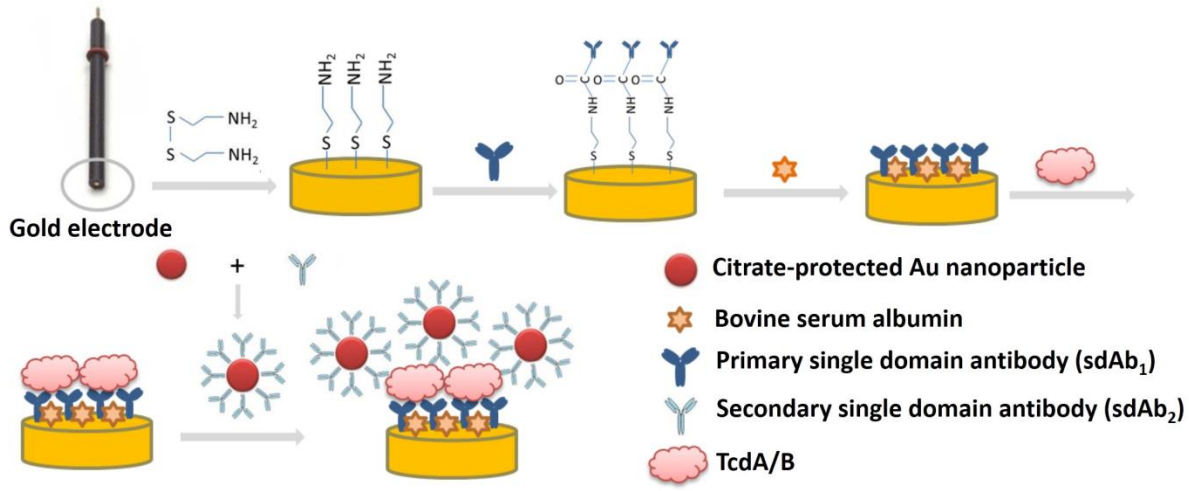

Scheme 6.2 Illustration of the immobilization process of the sandwich-type electrochemical impedance immunosensor.

6.2.6 Measurements

Transmission electron microscopy (TEM, JEOL 100CX-II) operating at 100 kV was applied to characterize the morphology and particle size. An Evolution 300 UV-Vis spectrophotometer was used for UV-Vis spectroscopic study. All electrochemical measurements were carried out using an Autolab PGSTAT12 electrochemical workstation (Metrohm, USA Inc.). A conventional cell with a three-electrode configuration was used throughout this work. The working electrode was modified gold electrode (1.6 mm dia., BASi). Platinum wire and Ag/AgCl (saturated KCl) were used as the counter electrode and the reference electrode, respectively. Cyclic voltammetry and electrochemical impedance spectroscopy were performed in the presence of 10 mM $K_3[Fe(CN)_6]/K_4[Fe(CN)_6]$ as a redox probe in 10mM PBS (containing 0.1 M KCl, pH=7.4). The EIS were recorded within the frequency range of 0.1 kHz to 10 kHz at 0.17 V (vs Ag/AgCl). All

the electrolytes were deaerated by bubbling nitrogen (N_2) for 20 min before the experimental procedure. All the experiments were carried out at room temperature.

6.3 Results and discussion

6.3.1 Characterization of Au NPs and sdAb$_2$-Au NPs

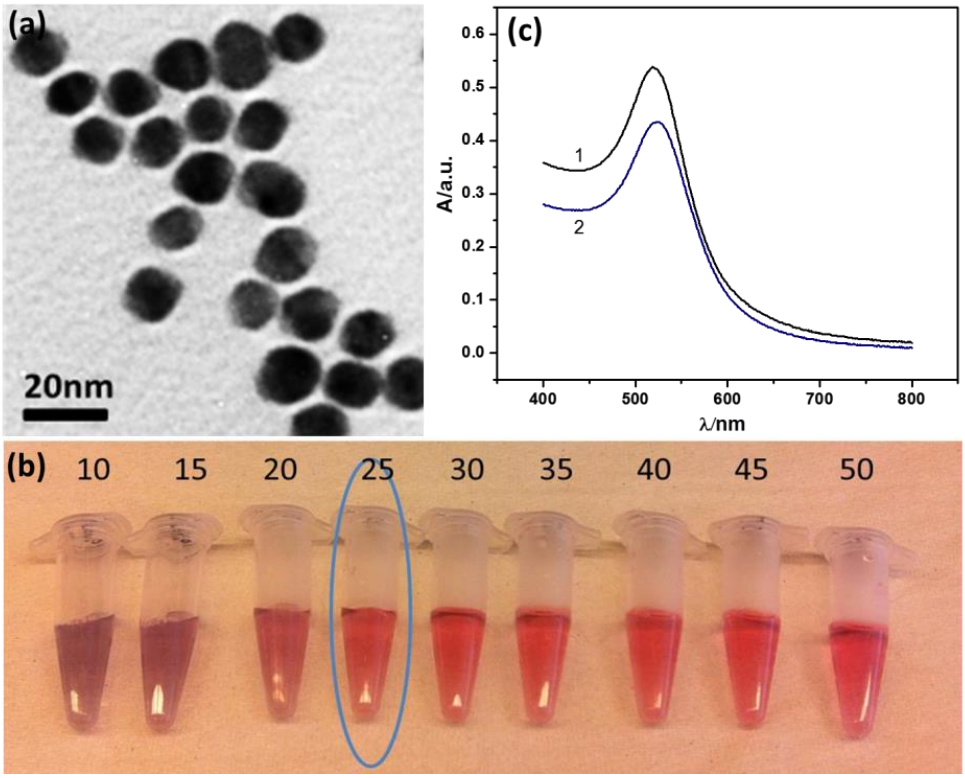

Figure 6.1 (a) TEM image of Au NPs; (b) Photograph of AuNPs suspension with different amount of sdAb$_2$; (c) UV-vis spectra of Au NPs (1: black curve) and sdAb$_2$-Au NPs (2: blue curve).

TEM image (Fig. 6.1a) shows a good monodispersity of as prepared Au NPs with an average spherical diameter of 13-15 nm. Fig 1b illustrates the color change of Au NPs suspension containing sdAb$_2$ coated Au NPs with different ratios in the present of NaCl. Nine aliquots of different amount (10-50 µL) of sdAb$_2$ (0.07 µg/µL) was diluted with PBS buffer in a total volume of 50 µL, and added separately into 500 µL Au NPs solution. The color of suspension with a low

amount (lower than 25 µL) changed from red to purple after addition of NaCl to induce precipitation. Therefore, 50 µL 0.035 µg/µL $sdAb_2$ per 500 µL Au NPs solution was determined as the optimal ratio for the antibody coating. UV-vis spectra of Au NPs (black curve) and $sdAb_2$ coated Au NPs (blue curve) were found in Fig. 6.1c. A characteristic surface plasmon resonance peak of AuNPs was observed at 519 nm. According to Lambert–Beer law, the concentration of Au NPs solution was calculated to be 1.96 nM form the peak intensity and known extinction coefficients [40]. The adsorption peak of blue curve shifts towards the red wavelengths for several nanometers, while the adsorption intensity drastically decreased. This fact further confirmed the conjugation of $sdAb_2$ and Au NPs.

6.3.2 Electrochemical characterization of the immunosensor

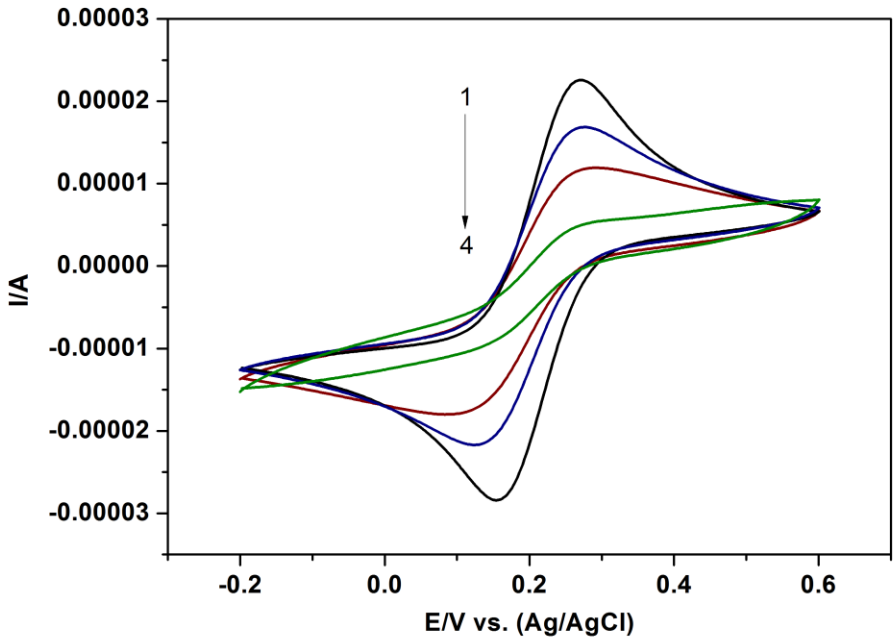

Figure 6.2 CVs of (1) Bare gold electrode; (2) $sdAb_1$/gold electrode; (3) BSA/$sdAb_1$/gold electrode; (4) TcdA/$sdAb_1$/gold electrode in 10 mM PBS containing 10 mM $K_3[Fe(CN)_6]/K_4[Fe(CN)_6]$ (pH=7.4).

The cyclic voltammogram of a fairly reversible redox couple ($Fe(CN)_6^{3-/4-}$) in PBS solution (pH=7.4) was studied from −0.2 V to 0.6 V at a scan rate of 50 mV s^{-1} to characterize each immobilization step on gold electrode. As can be seen in Fig. 6.2, $Fe(CN)_6^{3-/4-}$ showed a quasi-reversible one electron redox behavior at bare gold electrode. After $sdAb_1$ was immobilized onto the electrode surface, the current value remarkably decreased and the peak-to-peak separation (ΔEp) increased at the same time. It's probably because of an effective barrier to the electronic communication from $Fe(CN)_6^{3-/4-}$ to the electrode provided by the immobilized proteins. Similarly, the current further decreased and ΔEp increased when TcdA were absorbed on the electrode.

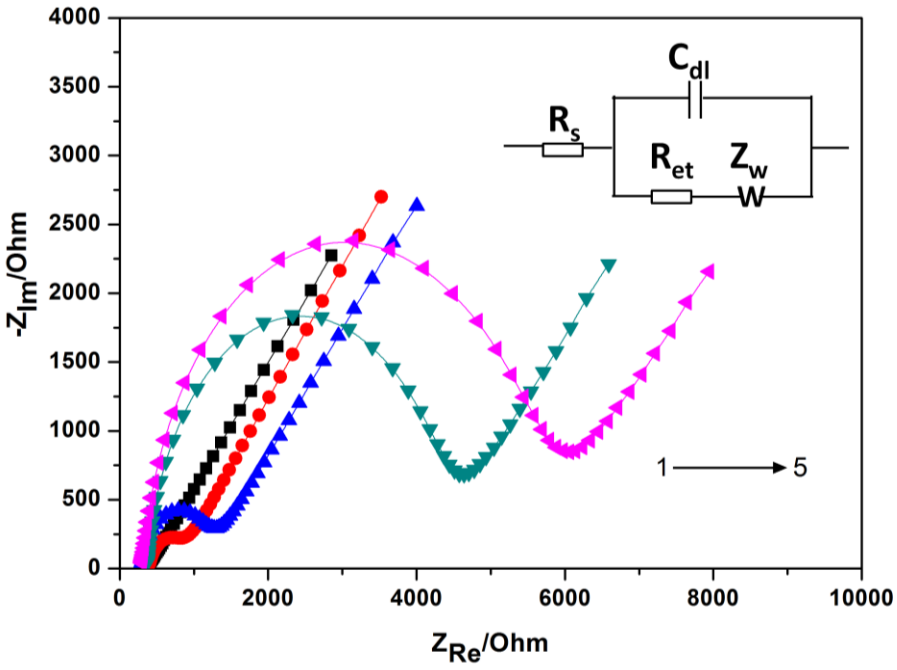

Figure 6.3 Nyquist plots of (1) Bare gold electrode; (2) $sdAb_1$/gold electrode; (3) BSA/$sdAb_1$/gold electrode; (4) TcdA/$sdAb_1$/gold electrode (50 pg/mL^{-1}); (5) $sdAb_2$-Au NPs/TcdA/$sdAb_1$/gold electrode in 10 mM PBS containing 10 mM $K_3[Fe(CN)_6]/K_4[Fe(CN)_6]$ (pH=7.4). Inset: the Randles model equivalent circuit for the electrochemical impedance data.

Fig. 6.3 gives the Nyquist plots of electrochemical impedance spectra of gold electrode layer by layer in 10 mM PBS solution containing 10 mM $K_3[Fe(CN)_6]/K_4[Fe(CN)_6]$ (pH=7.4), showing the real part of impedance (Z_{Re}) versus the negative of the imaginary part ($-Z_{Im}$). Inset is the Randles model equivalent circuit for the electrochemical impedance data [18], which includes the electrolyte resistance between working and reference electrodes (Rs), the double layer capacitance of electrode/electrolyte interface (C), Warburg impedance (Zw) causing by the diffusion of ions from the electrolyte to the interface and electron transfer resistance (Ret). The electrochemical impedance spectra often consist of a semicircle part at high frequencies and a linear part at lower frequencies. The linear part represents the diffusion limited process. The semicircle part corresponds to the electron transfer limited process, which shows the blocking behavior of electrode for the $Fe(CN)_6^{3-/4-}$ redox couple. When proteins were attached onto the electrode surface, they would form an inert electron transfer blocking layer and hence increase electron transfer resistance. The diameter of semicircle exhibits the R_{et} of electrode surface, which is an important parameter in the measurement of electrochemical impedance immunosensor. The impedance spectrum of gold electrode (curve 1) exhibits an almost straight line which is characteristic of diffusion limited process. The immobilization of $sdAb_1$ onto the electrode introduces a barrier to the interfacial electron transfer, thus curve 2 exhibits a small semicircle domain at high frequencies. Then, the use of BSA to block nonspecific binding sites results in a higher electron transfer resistance and enlarges the diameter of semicircle (curve 3). After the recognition reaction of BSA/$sdAb_1$/gold electrode with TcdA solution, the semicircle diameter markedly increased (curve 4). This increase is due to the generation of toxins onto the electrode surface through antibody-antigen interaction that further blocks the electron transfer. Finally, the impedance spectrum is amplified by using $sdAb_2$-Au NPs as an enhancement element to carry out

a sandwich format on the electrode surface. The formation of sandwich-type immune complex generates a lot of $sdAb_2$ on the electrode surface and has been proved to be helpful to amply the analytical signal (curve 5). The above results indicate that the designed sandwich immunoassay using electrochemical impedance spectroscopy technique can be employed to detect *C. difficile* toxins.

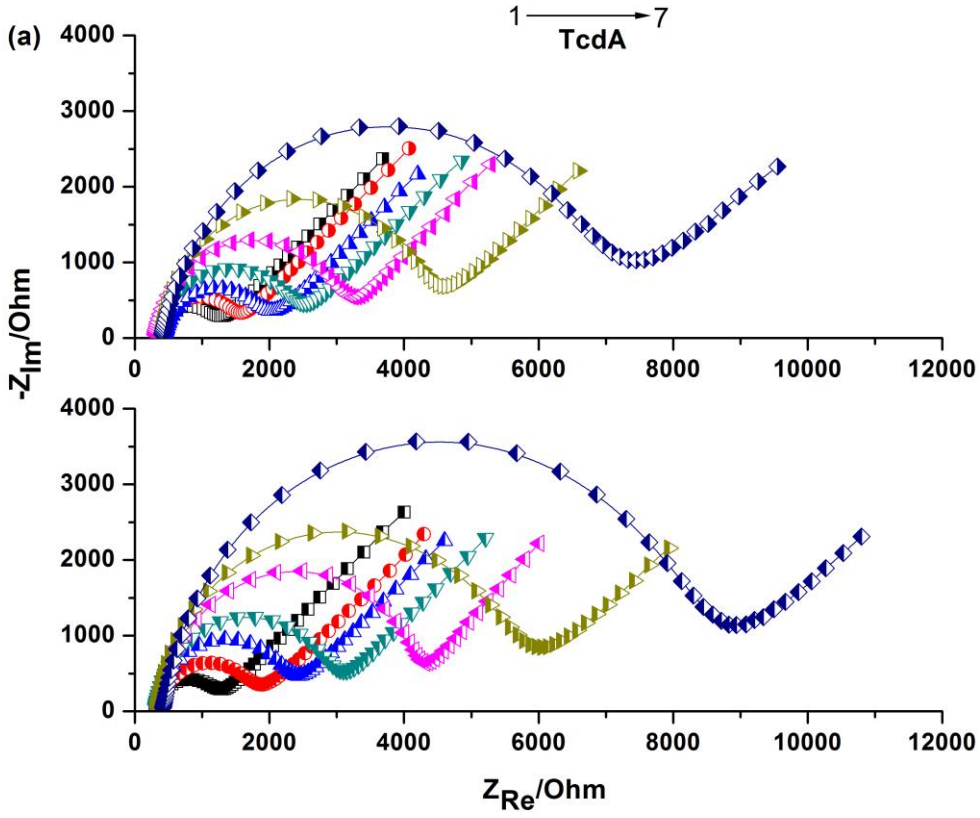

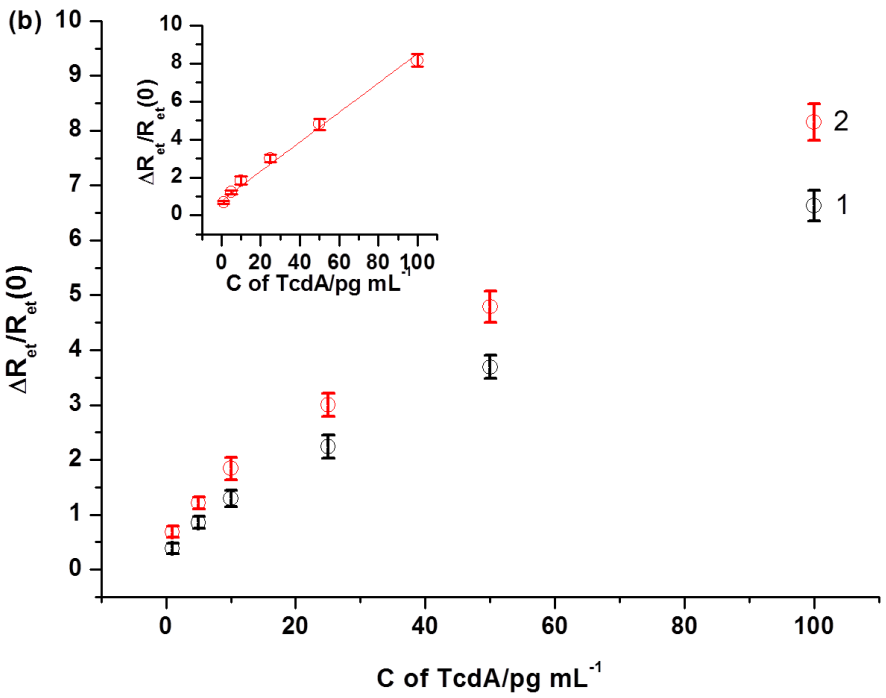

Figure 6.4 (a) Nyquist plots of BSA/sdAb$_1$/gold electrode (top) without and (bottom) with amplification of sdAb$_2$-Au NPs correspond to different concentration of TcdA (1: 0 pg/mL; 2: 1 pg/mL; 3: 5 pg/mL; 4: 10 pg/mL; 5: 25 pg/mL; 6: 50 pg/mL; 7: 100 pg/mL) in 10 mM PBS containing 10 mM $K_3[Fe(CN)_6]/K_4[Fe(CN)_6]$ (pH=7.4); (b) The relative resistance $\Delta R_{et}/R_{et}$ (0) of the BSA/sdAb$_1$/gold electrode without (1: black dot) and with (2: red dot) amplification. R_{et} (0): the R_{et} value of BSA/sdAb$_1$/gold electrode. Inset: The calibration curves of relative resistance $\Delta R_{et}/R_{et}$ (0) versus TcdA concentration with amplification of sdAb$_2$-Au NPs. The regression equation: y= 0.074 x + 0.933(r^2 = 0.99227).

In order to investigate the sensitivity of the impedance immunosensor, the change of R_{et} after incubating the sdAb$_1$ modified electrode in different concentrations of toxin solutions was measured. Fig. 6.4a shows the Nyquist plots of BSA/sdAb$_1$/gold electrode in various concentrations of TcdA solutions without (top) with (bottom) amplification of sdAb$_2$-Au NPs. The electron transfer resistance increases regularly with increasing TcdA concentrations from 1 pg/mL to 100 pg/mL. The binding of toxins onto the electrode would reduce electrode surface area and

increase electron transfer resistance. The constructed impedimetric immunosensor can detect the concentration of TcdA as low as 1pg/mL. The effect of amplification was examined and it turns out that the impedance signal was amplified by the immobilization of $sdAb_2$-Au NPs. It's known that the relative resistance is often used as a more valuable parameter than absolute resistance for impedance sensing applications [41]. The impedance increment is defined as $\Delta R_{et} = R_{et}(i) - R_{et}(0)$, where $R_{et}(0)$ is the R_{et} value of BSA/$sdAb_1$/gold electrode (step 3 of Scheme 1), and $R_{et}(i)$ is the value of R_{et} after toxins attach to BSA/$sdAb_1$/gold electrode (step 4 of Scheme 1). In the case of with amplification, $R_{et}(i)$ is the value of the impedance after the binding of $sdAb_2$-Au NPs onto TcdA/BSA/$sdAb_1$/gold electrode (step 5 of Scheme 1). Herein, the relative resistance $\Delta R_{et}/R_{et}(0)$ of BSA/$sdAb_1$/gold electrode without and with amplification at the same TcdA concentration was compared in Fig. 6.4b. It can be observed that there's an increment in $\Delta R_{et}/R_{et}(0)$ for the electrode with amplified operation compared to the one without amplified operation. The calibration curves of relative resistance versus TcdA concentration with amplification of $sdAb_2$-Au NPs were shown in the inset of Fig. 4b. A linear relationship between the relative resistance and TcdA concentration was obtained in the range of 1 pg/mL–100 pg/mL. The linear equation is $y = 0.074x + 0.933$, with a correlation coefficient r^2 of 0.99227, where y is the relative resistance and x is the TcdA concentration (unit of x: pg/mL). The limit of detection was calculated to be 0.61 pg/mL(S/N=3).

The detection of TcdB shows similar results in Fig. 6.5a, the electron transfer resistance increases regularly with increasing TcdB concentrations from 1 pg/mL to 100 pg/mL, and the relative resistance of the electrode with amplification (top) is bigger than the one without amplification (bottom). The regression equation is $y=0.076x+1.041$ ($r^2 = 0.99034$) for the calibration curves of $\Delta R_{et}/R_{et}(0)$ versus TcdB concentration with amplification of $sdAb_2$-Au NPs, and the LOD was 0.60 pg/mL (S/N=3) (Fig. 6.5b). It's clear that the detection signal enhanced due to the

amplification effect of $sdAb_2$-Au NPs for both TcdA and TcdB detection. Due to the sterical hindrance and the increased amount of antibody, very low detection limit (0.61 pg/mL for TcdA, 0.60 pg/mL for TcdB) was achieved.

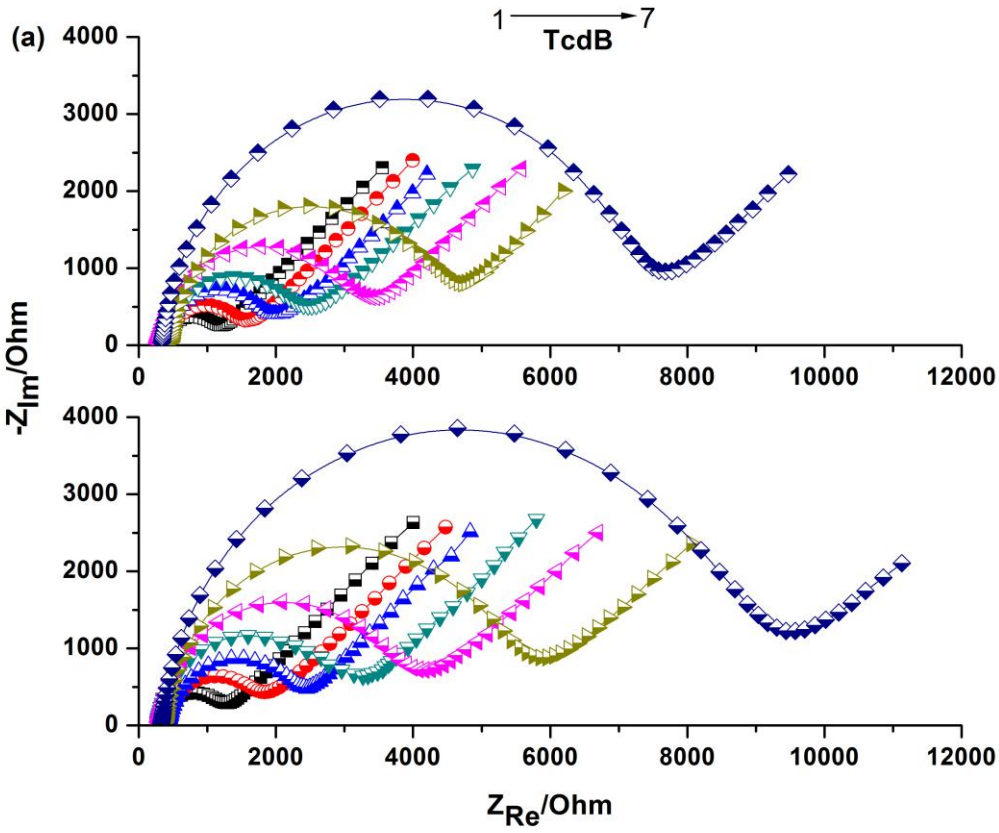

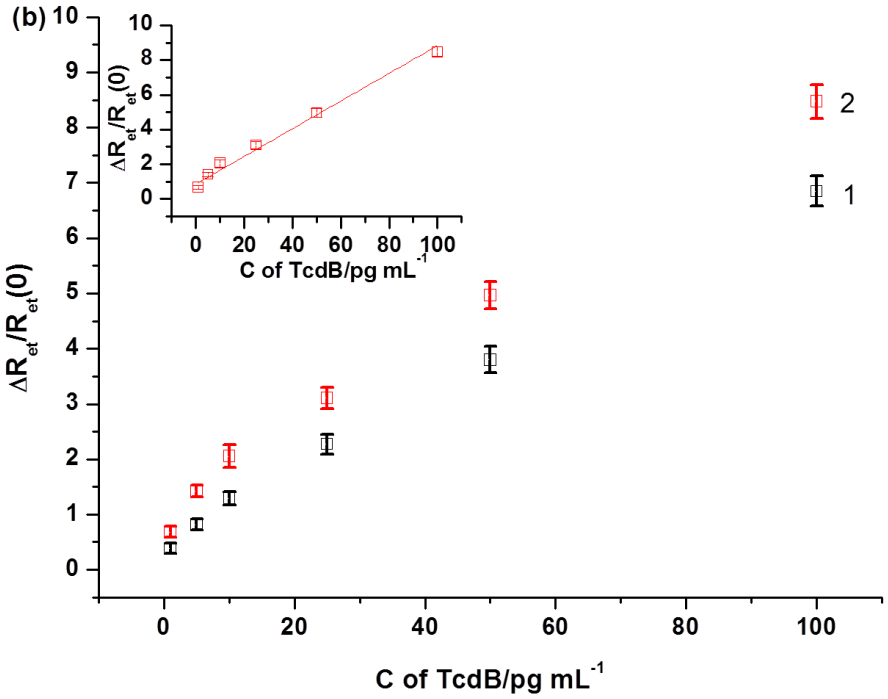

Figure 6.5 (a) Nyquist plots of BSA/sdAb$_1$/gold electrode (top) without and (bottom) with amplification of sdAb$_2$-Au NPs correspond to different concentration of TcdB (1: 0 pg/mL; 2: 1 pg/mL; 3: 5 pg/mL; 4: 10 pg/mL; 5: 25 pg/mL; 6: 50 pg/mL; 7: 100 pg/mL) in 10 mM PBS containing 10 mM $K_3[Fe(CN)_6]/K_4[Fe(CN)_6]$ (pH=7.4); (b) The relative resistance $\Delta R_{et}/R_{et}$ (0) of BSA/sdAb$_1$/gold electrode without (1: black square) and with (2: red square) amplification. R_{et} (0): the R_{et} value of BSA/sdAb$_1$/gold electrode. Inset: The calibration curves of relative resistance $\Delta R_{et}/R_{et}$ (0) versus TcdB concentration with amplification of sdAb$_2$-Au NPs. The regression equation: y=0.076 x+1.041 (r^2 = 0.99034).

Stability of the proposed impedance immunosensor is a key factor in practical applications. The prepared electrode was stored at 4 ºC for three weeks. The impedance results show the immunosensor could retain around 90 % of its initial response, indicating good stability.

6.3.3 Stool sample analysis

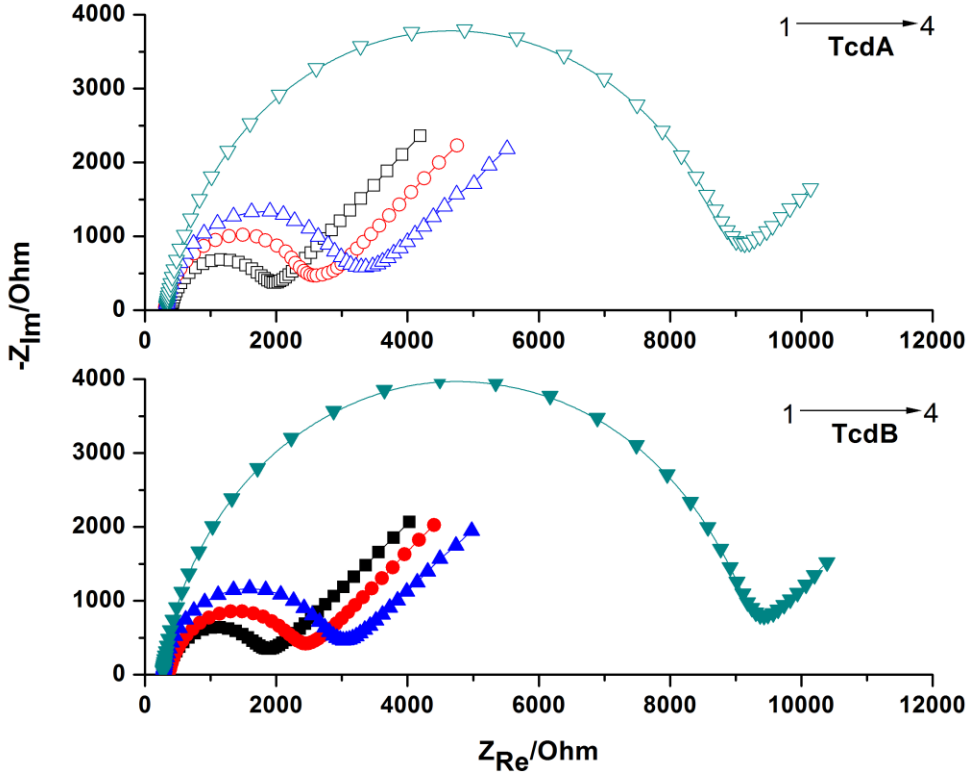

Figure 6.6 Nyquist plots of BSA/sdAb$_1$/gold electrode with amplification of sdAb$_2$-Au NPs correspond to different concentration of TcdA (top) and TcdB (bottom) in spiked negative stool sample (1: 1 pg/mL; 2: 5 pg/mL; 3: 10 pg/mL; 4: 100 pg/mL).

In order to investigate the performance of the designed immunosensor with stool sample, the BSA/sdAb$_1$/gold electrode was immersed in 1:5 diluted negative stool solution spiked with different concentration of TcdA and TcdB for 2 hours at 4 °C and then rinsed with PBS, respectively. After that, the electrode was transferred into sdAb$_2$-Au NP solutions to amplify the response signal. The comparison of blank single of the BSA/sdAb$_1$/gold electrode incubated in PBS and negative stool solution has been shown in Fig. S2. It can be found that the impedance signal of the two electrodes doesn't show significant difference, suggesting that the negative stool

sample was not responsible for the increase of R_{et}. The results of the detection of toxins diluted in negative stool solution in Fig. 6.6 indicated the capability of the immunosensor for the determination of both TcdA and TcdB in stool samples for clinical diagnosis.

6.4 Conclusions

A simple sandwich-type electrochemical impedance immunosensor with single domain antibody labeled gold nanoparticles as amplifying probe for detecting *C. difficile* toxin A and B was designed in this work. Initially, cystamine self-assembled monolayers were coated onto the gold electrode surface and utilized for the immobilization of primary antibody through amine coupling chemistry. Toxins were then bonded onto the electrode through antigen-antibody interaction. Finally, secondary antibody coated gold nanoparticles were introduced onto the electrode surface as an amplifying probe to optimize the immunosensing performance. This proposed method achieved a limit of detection for TcdA and TcdB as 0.61 pg/mL and 0.60 pg/mL (S/N=3) respectively. This electrochemical impedance immunosensor exhibited convenience and high sensitivity. The pilot study with spiked clinical stool samples showed promising results, indicating the designed biosensor has a great potential in clinical applications.

Acknowledgement

This work was supported by National Science Foundation (CMMI-1030289) to HSZ and by National Institute of Health grants R01AI088748, R01DK084509, U19AI109776, and R56AI99458 to HF.

References

[1] S. Khanna, D. S. Pardi, Mayo Clinic. 87 (2012) 1106-1117.

[2] G. P. Carter, J. I. Rood, D. Gut Lyras, Microbes 1 (2010) 58-64.

[3] D. Drudy, S. Fanning, L. Kyne, Int. J. Infect. Dis. 11 (2007) 5-10.

[4] M. J. LaMarche, J. A. Leeds, A. Amaral, J. T. Brewer, S. M. Bushell, G. Deng, J. M. Dewhurst, et al., Med. Chem. 55 (2012) 2376-2387.

[5] S. H. Cohen, D. N. Gerding, S. Johnson, C. P. Kelly, V. G. Loo, L. C. McDonald, J. Pepin, et al., Infect. Control Hosp. Epidemiol. 31 (2010) 431-455.

[6] A. Rodriguez-Palacios, S. Borgmann, T. R. Kline, J. T. LeJeune, Anim. Health Res. Rev. 14 (2013) 11-29.

[7] D. O'Connor, P. Hynes, M. Cormican, E. Collins, G. Corbett-Feeney, M. Cassidy, J. Clin. Microbiol. 39 (2001) 2846-2849.

[8] D. N. Gerding, S. Johnson, L. R. Peterson, M. E. Mulligan, J. Silva, Infect. Control Hosp. Epidemiol. 16 (1995) 459-477.

[9] T. W. Chang, S. L. Gorbach, J.B. Bartlett, Infect. Immun. 22 (1978) 418-422.

[10] X. He , J. Wang, J. Steele, X. Sun, W. Nie, S. Tzipori, H. Feng, J. Microbiol. Methods 78 (2009) 97-100.

[11] T. D. Wilkins, D. M. Lyerly, J. Clin. Microbiol. 41 (2003) 531-534.

[12] R. H. Yolken, L. S. Whitcom, G. Marien, J. D. Bartlett, J. Libby, M. Ehrich, T. Wilkins, J. Infect. Dis. 144 (1981) 378-378.

[13] N. Gan, H. Jin, T. Li, L. Zheng, Int. J. Nanomedicine 6 (2011) 3259-3269.

[14] D. Grieshaber, R. MacKenzie, J. Voros, E. Reimhult, Sensors 8 (2008) 1400-1458.

[15] I. I. Suni, Trends Anal. Chem. 27 (2008) 604-611.

[16] Y. Wang, Z. Ye, Y. Ying, Sensors 12 (2012) 3449-3471.

[17] B. Y. Chang, S. M. Park, Annu. Rev. Anal. Chem. 3 (2010) 207-229.

[18] X. Dominguez-Benetton, S. Sevda, K. Vanbroekhoven, D. Pant, Chem. Soc. Rev. 41 (2012) 7228-7246.

[19] E. C. Cho, B. O. Jang, E. J. Kim, K. K. Koo, Korean J. Chem. Eng. 25 (2008) 548-552.

[20] L. Yang, Y. Li, G. F. Erf, Anal. Chem. 76 (2004) 1107-1113.

[21] X. Chen, Y. Wang, J. Zhou, W. Yan, X. Li, J. J. Zhu, Anal. Chem. 80 (2008) 2133- 2140.

[22] R. Pei, Z. Cheng, E. Wang, X. Yang, Biosens. Bioelectron. 16 (2001) 355-361.

[23] C. Ruan, L. Yang, Y. Li, Anal. Chem. 74 (2002) 4814-4820.

[24] A. Hayat, C. Yang, A. Rhouati, J. L. Marty, Sensors 13 (2013) 15187–15208.

[25] J. Wang, Small 1 (2005) 1036-1043.

[26] J. F. Rusling, C. V. Kumar, J. S. Gutkind, V. Patel, Analyst 135 (2010) 2496-2511.

[27] Y. Xu, H. Cai, P. G. He, Y. Z. Fang, Electroanalysis 16 (2004) 150-155.

[28] Y. C. Yeh, B. Creran, V. M. Rotello, Nanoscale 4 (2012) 1871-1880.

[29] B. Wenger, K. Kugelbrey, H. Gao, H. Sigrist, G. Voirin, Biosens. Bioelectron. 34 (2012) 94-99.

[30] J. M. Pingarrón, P. Yáñez-Sedeño, A. González-Cortés, Electrochim. Acta. 53 (2008) 5848-5866.

[31] H. Tang, J. Chen, L. Nie, Y. Kuang, S. Yao, Biosens. Bioelectron. 22 (2007) 1061-1067.

[32] A. Bonanni, M. I. Pividori, S. Campoy, J. Barbe, M. del Valle, Analyst 134 (2009) 602-608.

[33] H. Chen, J. H. Jiang, Y. Huang, T. Deng, J. S. Li, G. L. Shen, R. Q. Yu, Sensor Actuat. B Chem. 117 (2006) 211-218.

[34] Z. Y. Yang, D. Schmidt, W. L. Liu, S. Li, L. F. Shi, J. L. Sheng, K. Chen, et al., J. Infect. Dis. 210 (2014) 964–972.

[35] G. Yang, B. Zhou, J. Wang, X. He, X. Sun, W. Nie, S. Tzipori, et.al., BMC microbiol. 8 (2008) 192.

[36] K. C. Grabar, R. G. Freeman, M. B. Hommer, M. J. Natan, Anal. Chem. 67 (1995) 735-743.

[37] J. W. Slot, H. J. Geuze, Eur. J. Cell Biol. 38 (1985) 87-93.

[38] Z. P. Chen, Z. F. Peng, P. Zhang, X. F. Jin, J. H. Jiang, X. B. Zhang, G. L. Shen, et al., Talanta 72 (2007) 1800-1804.

[39] M. Saleh, H. Soliman, O. Haenen, M. El-Matbouli, J. Fish Dis. 34 (2011) 845-852.

[40] X. Liu, M. Atwater, J. Wang, Q. Huo, Colloids Surf. B Biointerfaces. 58 (2007) 3-7.

[41] B. Rezaei, T. Khayamian, N. Majidi, H. Rahmani, Biosens. Bioelectron. 25 (2009) 395-399.

Supplementary Information

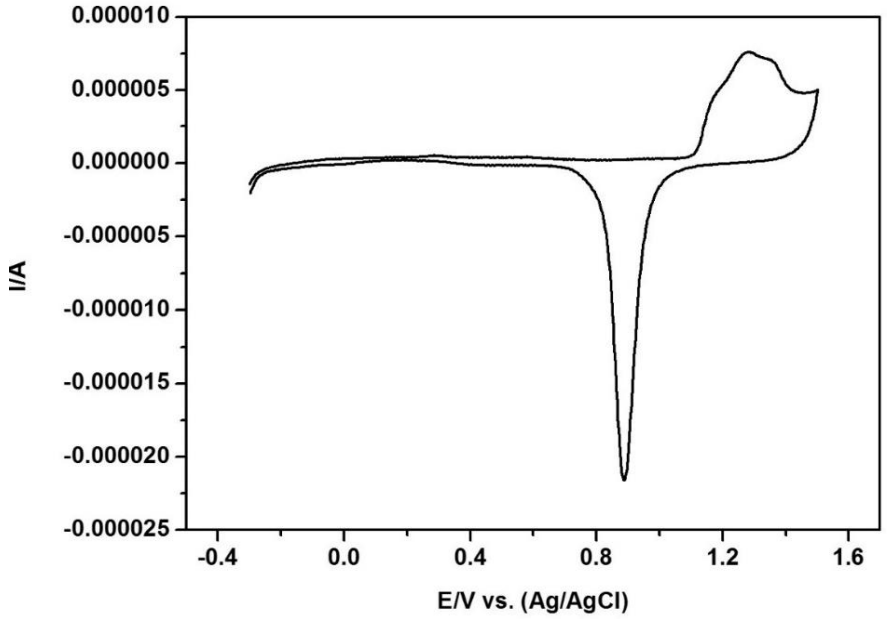

Figure S6.1 CV of bare gold electrode in 0.5 M H_2SO_4, scan rate: 100 mV/s.

Fig. S6.1 shows the typical CV curve of a bare, clean gold electrode in 0.5 M H_2SO_4. The real surface of the gold electrode can be determined by integration of the reduction peak of gold oxide located at +0.89 V [1]. As we know, the charge required for the reduction of the oxygen layer depends on the crystalline structure of gold [2, 3]. Herein, a value of 400 μC cm^{-2} was use as standard reference charge for polycrystalline Au [4]. Therefore, the real surface area of gold electrode used in this work was calculated to be 0.0232 cm^2.

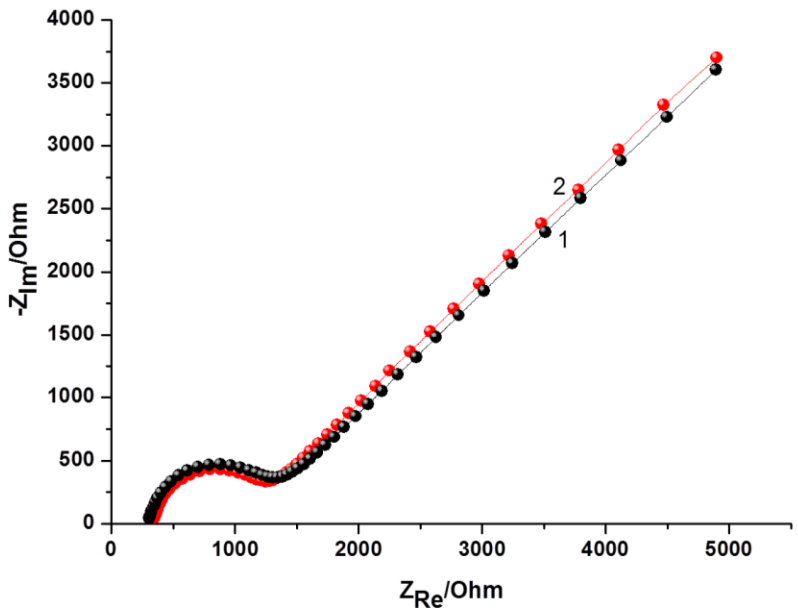

Figure S6.2 The comparison of blank single of the BSA/sdAb$_1$/gold electrode incubated in PBS (1: black dot) and negative stool solution (2: red dot).

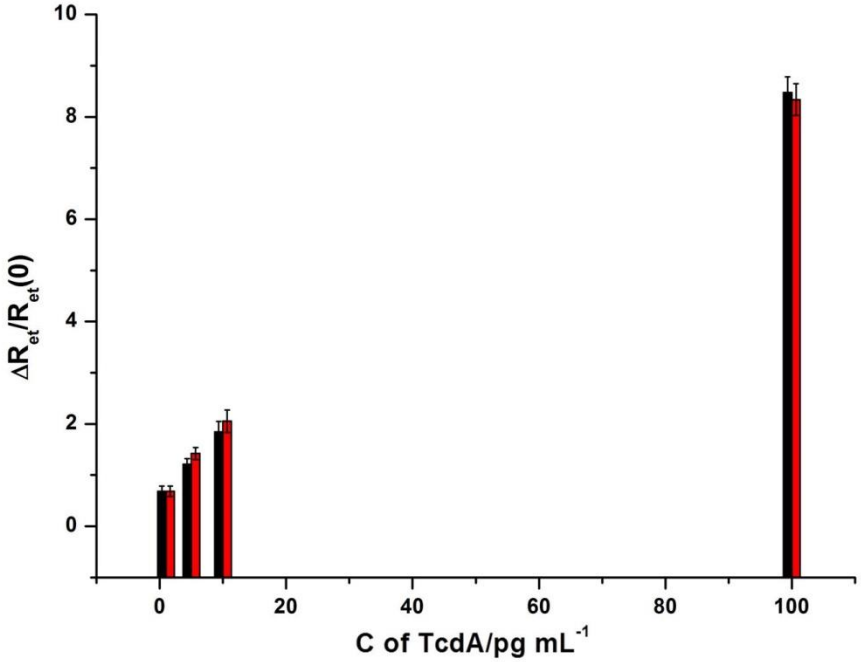

Figure S6.3 The comparison of the relative resistance $\Delta R_{et}/R_{et}$ (0) of BSA/sdAb$_1$/gold electrode with amplification of sdAb$_2$-Au NPs correspond to different concentration of TcdA in PBS (black column) and negative stool sample (red column).

Table S6.1 Comparison of reported *C. difficile* detection methods with the proposed method

Method	**Analyte**	**Limit of Detection**	**Reference**
Cell-based immunocytotoxicity assay	TcdA	less than 1 pg/ml	5
Differential pulse voltammetry	TcdB	0.7 pg/mL	6
HT29 cell cytotoxicity assay	TcdA	100 pg/ml	7
Vero cell cytotoxicity assay	TcdB	25 pg/ml	7
Slow off-rate modified aptamers based Enzyme immunoassays	TcdA/B	Less than 300 pg/mL for TcdA; 300 pg/mL for TcdB	8
Electrochemical impedance immunosensor	TcdA/B	0.61 pg/mL for TcdA; 0.60 pg/mL for TcdB	9/This work

[1] Y. Z. Fu, R. Yuan, D. P. Tang, Y. Q. Chai, L. Xu, Colloids Surf. B Biointerfaces 68 (2009) 130–135.

[2] R. F. Carvalhal, R. S. Freire, L. T. Kubota, Electroanalysis 17 (14) (2005) 1251-1259.

[3] J. C. Hoogvliet, M. Dijksma, B. Kamp, and W. P. van Bennekom, Anal. Chem. 72 (2000) 2016-2021.

[4] S. Trasatti, O. A. Petrii, Pure Appl. Chem. 5 (1991) 711-734.

[5] X.Y. He, J.F. Wang, J. Steele, X.M. Sun, W.J. Nie S. Tzipori, H. P. Feng, J. Microbiol .Methods. 78 (2009) 97–100.

[6] Y.S. Fang, S.Y. Chen, X.J. Huang, L.S. Wang, H.Y. Wang, J.F. Wang, Biosens. Bioelectron. 53 (2014) 238-244.

[7] S.T. Cartman, M.L. Kelly, D. Heeg, J.T. Heap, N. P. Minton, Appl. Environ. Microbiol. 78 (2012) 4683-4690.

[8] U.A. Ochsner, E. Katilius, N. Janjic, Diagn. Micr. Infec. Dis. 76 (2013) 278-285.

[9] Z.Z. Zhu, L.F. Shi, H.P. Feng, H.S. Zhou, Bioelectrochemistry 101 (2015) 153-158.

Chapter 7 Conclusions and outlook

In this thesis, electrochemical approaches based on low dimensional nanomaterials for catalysis and sensing applications have been studied. Two types of nanotubes and three kinds of nanoparticles were successfully synthesized by different nanofabrication methods. The detailed information and the corresponding electrochemistry application of each type of nanomaterials are presented in table 7.1.

Table 7.1 Low dimensional nanomaterials and their applications in electrochemistry in this thesis.

	Zero dimensional nanomaterials			One dimensional nanomaterials	
Nanomaterials used in this thesis	Pt nanoparticles	CuO nanoparticles	Au nanoparticles	Bamboo shaped carbon nanotubes	TiO_2 nanotube arrays
Fabrication method	Chemical deposition	Electrochemcial deposition	Citrate-mediated reduction	Chemical vapor deposition	Electrochemical anodization
Size	Diameter: 2-4 nm; 6-7 nm	Diameter: ~120 nm	Diameter: 13-15 nm	Diameter:~25-30 nm Length: up to several microns	Diameter: ~ 60 nm Length: ~3.5 μm
Application in this thesis	Electrolycatalyst for methanol/ethanol oxidation	Electrolycatalyst for glucose sensing	Signal amplification element for electrochemcial sensing of *C. difficile* toxins	Support material for Pt nanoparticles and enzyme HRP	Nanostructured electrode and support material for CuO nanoparticles
Chapter	2&3	5	6	2&3&4	5

It's known that nanostructured conductive materials are promising candidates not only as electrocatalysts but also as their supports in enhancing the performance of an electrocatalysis process. In this work, nitrogen doped bamboo shaped carbon nanotubes were prepared by chemical vapor deposition method, which is a typical gas phase "bottom up" method. From the TEM results of the samples, we concluded that the growth model of the synthesized bamboo shaped carbon nanotubes is base growth model. The role of the nitrogen doping in the formation of bamboo shaped structure is to influence the carbon diffusion through nitrogen diffusion. Meanwhile,

structural defects caused by nitrogen doping provides more active sites for chemical and electrochemical reactions on BCNT surface than on hollow CNT surface. Herein, BCNTs were used as support for loading Pt nanoparticles on their surface. The resulted Pt/BCNTs electrolycatalyst was found to display better electrocatalytic activity for methanol/ethanol oxidation than Pt NP modified undoped carbon nanotube. The better performance of BCNTs in electrolycatalysis may be due to the defective sites and active sites caused by nitrogen doping on their surface. Furthermore, a BCNTs/polymer film was prepared and employed to immobilize HRP for the electrocatalysis of H_2O_2. Direct electrochemistry and electrocatalysis of HRP incorporated into the film was investigated. The results indicated that the immobilized HRP onto the film retains its good bioelectrocatalytic activity to H_2O_2. The defective sites and active sites on the BCNTs surface induced by nitrogen doping could help to promote the direct electron transfer between enzyme and electrode. Therefore, it provides a vast array of new opportunities to use BCNTs as building units for bioelectrochemical applications.

It's known that TiO_2 nanotubes have much better biocompatibility and show greater potential as implant materials than carbon nanotubes. Besides large surface area, highly ordered one dimensional, one-end open tubular structure and good biocompatibility, TiO_2 nanotubes offers several additional benefits as an electrode in electrochemical biosensors. Thus, an inexpensive and well performing non-enzymatic electrochemical glucose biosensor was developed based on TiO_2 nanotube array electrode. Well-aligned TiO_2 nanotube arrays were successfully synthesized by electrochemical anodization. Highly uniform CuO nanoparticles were electrodeposited onto TiO_2 nanotube arrays through a two-step method and used as electrocatalyst for the glucose sensing. The proposed electrode shows a high sensitivity of 239.9 $\mu A\ mM^{-1}\ cm^{-2}$ and a low detection limit of 0.78 μM with good stability, reproducibility, selectivity and fast response time.

Finally, a sandwich-type electrochemical impedance immunosensor for detecting Clostridium difficile toxin A (TcdA) and toxin B (TcdB) was proposed. Single domain antibody conjugated gold nanoparticles were applied to amplify the detection signal. Initially, cystamine self-assembled monolayers were coated onto a gold electrode surface and utilized for the immobilization of primary single domain antibody through amine coupling chemistry. Toxins were then bonded onto the electrode through antigen-antibody interaction. After that secondary antibody coated gold nanoparticles were introduced onto the electrode surface as an amplifying probe to optimize the immunosensing performance. This proposed method achieved a limit of detection for TcdA and TcdB as 0.61 pg/mL and 0.60 pg/mL (S/N=3) respectively with good stability and selectivity. This method is simple, quick turnaround, and ultrasensitive, thus possesses a great potential for clinical applications.

In future, the improvement of the electrocatalytic performance of an electrolycatalysis process can be achieved from following two aspects: increase the surface area and optimize chemical composition of electrolycatalyst and support material as well as the electrode. In general, the addition of a second/third element M to Pt nanoparticles can improve their performance for small organic molecules due to a bio-functional effect. The oxidation of methanol/ethanol to CO_2 is more complete at the binary and ternary electrocatalysts compared to Pt alone due to the OH group formed on the neighboring M atoms. Herein, M could be Ru [1], Au [2], Pd [3] and so on. On the other hand, nanostructured conductive porous materials with good electrical conductivity and mechanical property can significantly increase the active surface area, thus the controllable synthesis of novel nanostructure porous electrocatalysts and its support as well as electrode are key points in the area of electrolysis.

The advantages of electrochemical biosensors at nanoscale include rapid, sensitive, cost effective and portable. Depending on the types of the target molecular, different strategies can be applied to design the sensor device. Similar to electrolycatalysis, novel nanostructures with high surface area are also need to be developed to optimize the performance of the biosensors. For enzyme based electrochemical biosensors, the maintaining of the bioactivity of enzyme on the electrode for a long time is still a challenge. The utilization of enzyme protection reagent such polymer is one of the most used approach. Recently, 3D polymer nanostructure is found to be able to remain the activity and increase the loading amount of enzyme on electrode [4]. Non-enzymatic biosensors can avoid the use of enzyme and are considered as a promising strategy for future novel electrochemical biosensors. Besides the common electrocatalyst like metal, alloy or metal oxide nanostructure, quantum dots also has excellent performance in non-enzymatic biosensors [5]. Moreover, this type of biosensors provides the possibilities to detect two or three targets at the same time [6]. For electrochemical biosensor based on electrochemical impedance spectra, the key issues are to amply the detection signal, improve the productivity and develop novel electrode structure. Currently, surface coating with nanomaterials like graphene is a popular approach. Overall speaking, a current trend in electrochemical biosensor is to integrate with other technique like microfluidic and optical technique to fabricate easy-to-use analytical tools for point-of-care diagnosis [7].

Reference

[1] C.W. Kuo, I.T. Lu, L.C. Chang, Y.C. Hsieh, Y.C. Tseng, P.W. Wu, J.F. Lee, J. Power Sources 240 (2013) 122-130.

[2] S. Xiao, F. Xiao, Y. Hu, S. Yuan, S. Wang, L. Qian, Y. Liu, Sci. Rep. 4 (2014).

[3] J.Y. Lee, D.H. Kwak, Y.W. Lee, S. Lee, K.W. Park, Phys. Chem. Chem. Phys. 17 (2015) 8642-8648.

[4] A.M. Parra-Alfambra, E. Casero, M.D. Petit-Dominguez, M. Barbadillo, F. Pariente, L. Vazquez, E. Lorenzo, Analyst 136 (2011) 340-347.

[5] N.u.H. Alvi, V.J. Gómez, P.E.D.S. Rodriguez, P. Kumar, S. Zaman, M. Willander, R. Nötzel, Sensors (Basel, Switzerland) 13 (2013) 13917-13927.

[6] J.A. Hansen, J. Wang, A.-N. Kawde, Y. Xiang, K.V. Gothelf, G. Collins, J. Am. Chem. Soc. 128 (2006) 2228-2229.

[7] B. Liu, D. Du, X. Hua, X.Y. Yu, Y. Lin, Electroanalysis 26 (2014) 1214-1223.

List of publications, book chapter and conference presentation

Publications after joining WPI

1. **Zanzan Zhu**, H. Susan Zhou, A novel non-enzymatic glucose biosensor based on CuO nanoparticle-decorated TiO_2 nanotube arrays, In preparation.
2. **Zanzan Zhu**, Lianfa Shi, Hanping Feng, H. Susan Zhou, Single domain coated Au nanoparticles as enhancer for Clostridium difficile toxin detection by electrochemical impedance immunosensors. *Bioelectrochemistry* 101 (2015) 153-158.
3. **Zanzan Zhu**, Brandon Bukowski, N. Aaron Deskins, H. Susan Zhou, Bamboo shaped carbon nanotube supported platinum electrocatalyst synthesized by high power ultrasonic-assisted impregnation method for methanol electrooxidation and related density functional theory calculations. *International Journal of Hydrogen Energy* 40 (2015) 2216-2224.
4. **Zanzan Zhu**, Olijora Rezhdo, Matthew Perrone, Zhengzheng Bao, Ahsan Munir, Jianlong Wang, H. Susan Zhou, Jiahui Shao, Magnetite nanoparticles photoresist derived carbon as a suitable substratum for nerve cell culture, *Colloids and Surfaces B: Biointerfaces* 102 (2013) 428-434.
5. **Zanzan Zhu**, Jianlong Wang, Ahsan Munir, H. Susan Zhou, Direct electrochemistry and electrocatalysis of horseradish peroxidase immobilized on bamboo shaped carbon nanotube/chitosan matrix, *Colloids and Surfaces A: Physicochemical and Engineering Aspects* 385 (2011) 91-94.
6. **Zanzan Zhu**, Jianlong Wang, Ahsan Munir, H. Susan Zhou, Electrocatalytic activity of Pt nanoparticles on bamboo shaped carbon nanotubes for ethanol oxidation, *Electrochimica Acta* 55 (2010) 8517-8520.

7. Ahsan Munira, **Zanzan Zhu**, JianlongWang, H. Susan Zhou, FEM analysis of magnetic agitation for tagging biomolecules with nanoparticles in a microfluidic system, *Sensors and Actuators B* 197 (2014) 1-12.
8. Ahsan Munira, **Zanzan Zhu**, JianlongWang, H. Susan Zhou, Experimental investigation of magnetically actuated separation using tangential microfluidic channels and magnetic nanoparticles, *Nanobiotechnology* 8 (2014) 102-110.
9. Ahsan Munira, **Zanzan Zhu**, JianlongWang, H. Susan Zhou, In situ analysis of capturing dynamics of magnetic nanoparticles in a microfluidic system, *Smart Structures and Systems* 12 (2013) 1-22.
10. Jianlong Wang, **Zanzan Zhu**, Ahsan Munir, H. Susan Zhou, Fe3O4 Nanoparticles Enhanced SPR Sensing for Ultrasensitive Sandwich Assay, *Talanta* 84 (2011) 783–788.
11. Ahsan Munir, Jianlong Wang, **Zanzan Zhu**, H. Susan Zhou, Residence time distribution analysis of magnetic nanoparticle-enhanced mixing using time-dependent magnetic actuation in microfluidic system, *Microfluidics and Nanofluidics* 10 (2012) 735-747.
12. Ahsan Munir, Jianlong Wang, **Zanzan Zhu**, H. Susan Zhou, Mathematical Modeling and Analysis of a magnetic nanoparticle-enhanced mixing in a microfluidic system using time-dependent magnetic field, *IEEE Transaction on Nanotechnology* 10 (2011) 753-761.
13. Jianlong Wang, Ahsan Munir, **Zanzan Zhu**, H. Susan Zhou, Magnetic Nanoparticle Enhanced Surface Plasmon Resonance Sensing and Its Application for the Ultrasensitive Detection of Magnetic Nanoparticle-Enriched Small Molecules, *Analytical Chemistry* 82 (2010) 6782-6789.

Book chapter

- **Zanzan Zhu**, H. Susan Zhou, Nanoparticles for Biosensing Applications: Current aspects and Prospects, "Noble Metal Nanoparticles for Biomedical Applications", World Scientific Publishers, 2015.

Conference Presentation

- **Zanzan Zhu**, Jianlong Wang, Ahsan Munir, H. Susan Zhou, Direct Electrochemistry and Electrocatalysis of Bamboo Shaped Carbon Nanotube Based Nanocaomposite, MRS 2011 Fall Meeting, Boston, 11/2011.
- **Zanzan Zhu**, Hanping Feng, H. Susan Zhou, Gold nanoparticle based electrochemical impedance biosensor with signal amplification for the detection of Clostridium difficile toxins, MRS 2013 Fall Meeting, Boston, 12/2013.